The
PHILOSOPHICAL
MAGAZINE

FIRST PUBLISHED IN 1798

A Journal of
Theoretical Experimental
and Applied Physics

Physicists, chemists and their biological colleagues have a fundamental common interest in the properties of molecules and molecular assemblies and the need has been growing for a journal which would bring together experimental and theoretical contributions to this field.

The physical aspects of molecules will be dealt with, in particular:

1. The structure of molecules as determined by physical methods and interpreted by quantum mechanics;

2. The electromagnetic properties of molecules and the processes of molecular excitation, ionization and dissociation;

3. The interaction between molecules and the equilibrium and transport properties of molecular assemblies.

The following contributions have been received for the first volume:

1. Nuclear Magnetic Resonance and Rotational Isomerism in Substituted Ethanes. By J. A. POPLE

2. Dielectric Properties of Iodine in Aromatic Solvents at 9000 Mc./sec. By G. W. NEDERBRAGT and J. PELLE

3. On the Dipole Moments of Azines. By H. F. HAMEKA and A. M. LIQUORI

4. Electron–Electron Separation in Molecular Hydrogen. By M. P. BARNETT, F. W. BIRSS and C. A. COULSON

5. On Irreversible Processes in Quantum Mechanics. By I. PRIGOGINE and M. TODA

6. The Transport of Energy and Momentum in a Dense Fluid of Rough Spheres. By J. P. VALLEAU

7. Constant Pressure in Statistical Mechanics. By W. BYERS BROWN

8. One-dimensional Multicomponent Mixtures. By H. C. LONGUET-HIGGINS

The Effects of Radiation on the near Infra-Red Absorption Spectrum of α-Quartz†

By E. W. J. Mitchell and J. D. Rigden

The Physics Research Laboratory,
University of Reading

Abstract

The variation of the absorption strength and spectrum in the region of $3\,\mu$ has been determined for different specimens of crystalline quartz and for x-ray, electron and pile irradiated crystals. It is shown that the $3\,\mu$ group of bands is associated with imperfections rather than harmonics or combinations of lattice vibration frequencies, and that the imperfections are not Frenkel or Schottky defects. Two of the bands, 2·88 and 2·95 μ, are anisotropic, having anisotropic absorption ratios $(\mathbf{E}_{\shortparallel}c/\mathbf{E}_{\perp}c)\leqslant 0\cdot130$ and $\leqslant 0\cdot145$ respectively. A band is induced by pile irradiation at 2·79 μ but tends to saturate at a low dose $(<10^{19}\,n^{\circ}\,\mathrm{cm}^{-2})$. The band is not produced by ionizing radiation. It is suggested that the 2·79 μ band may be due to O–H bond formation by association of hydrogen impurity with the products of atomic damage. This band is also anisotropic with a ratio of 0·71. Possible defect axis directions which could give the observed anisotropic ratios are discussed.

§ 1. Introduction

THERE is a group of absorption bands in quartz centred about $3\,\mu$. The spectrum has been measured by, amongst others, Dreisch (1927), Plyler (1929), Drummond (1936) and Arnold (1954), and examination of their results, together with those obtained in this laboratory, indicates that the strength of the absorption is specimen dependent. It has to be assumed therefore that the bands are associated with imperfections, contrary to what has frequently been postulated. By introducing further imperfections by irradiation with high energy particles we can determine whether the existing bands are associated with the simple point defects.

§ 2. Experimental

All the measurements have been made with the cooperation of Dr. J. Goulden of the N.I.R.D., Shinfield, who kindly put the double-beam Grubb–Parson's spectrometer at our disposal. In most cases the rocksalt

† Communicated by Professor R. W. Ditchburn.

prism was used but some measurements were made using a grating (2400 lines per inch). A specially constructed specimen holder and cell enabled spectra to be obtained at temperatures in the range $-190°$c to $100°$c.

Most of the measurements have been made on specimens of the best optical quality Brazilian quartz obtained from Hilger and Watts, Ltd. The specimens were $1·5 \times 1·0 \times 1·0$ cm and had two pairs of polished faces so that anisotropic absorption measurements could be made on the same crystal. The c-axis was along one of the 1 cm edges. Some measurements were made on a synthetic quartz crystal obtained from the G.E.C. Research Laboratories, Wembley.

The absorption of 1 cm of quartz at 2μ is negligible (less than $0·01$ cm^{-1}, Drummond 1936) and from the known refractive index the transmission of a non-absorbing specimen for light at normal incidence is calculated to be $91·5\%$. Between 2 and 4μ the refractive index can be taken as constant without introducing any significant error. The double beam compensation mechanism was correct to $\pm 0·5\%$ for transmissions between 10 and 100% so that the value of transmission (T) at a given wavelength was found by linear interpolation between the zero and $91·5\%$ levels. If x cm is the specimen thickness the absorption coefficient is given by $\mu(\text{cm}^{-1}) = 1/x \ln 91·5/T$. The errors in μ resulting from the measurement of the traces are $\pm 0·1$ cm^{-1} for a 1 cm specimen when $\mu \simeq 2·5$ cm^{-1}, falling rapidly to $\pm 0·01$ cm^{-1} for $\mu \simeq 0·1$ cm^{-1}. The wavelength scale was calibrated using the lines of water vapour and from a polystyrene sample using the wavelengths given by Plyler and Peters (1951).

Details of irradiations are given in the appropriate sections below.

§ 3. Results

3.1. *The Absorption in Unirradiated Crystals*

The absorption spectra of various unirradiated crystals are shown in figs. 1 and 2. All the curves refer to measurements in which the light travels parallel to the c-axis. It will be seen that these spectra are composed of several overlapping bands which we describe as α, β, γ etc. Labelling the bands in this way is convenient because the value of the photon energy at the peak depends on the amount of absorption present in the adjacent bands.

In some specimens (fig. 1) the α-band is prominent, whilst in others (fig. 2 (*a*)) it is barely resolved. The band β is just a point of inflection on all the curves but γ, δ and ϵ are well defined peaks. The γ-band is the principal peak in all but one of the specimens and occurs at a photon energy of $0·420$ ev ($2·95\mu$). The exception is the synthetic crystal (fig. 2 (*b*)) in which both α and γ are weaker, possibly absent, and a peak which may correspond to β, is resolved between the normal α, γ positions.

Fig. 1
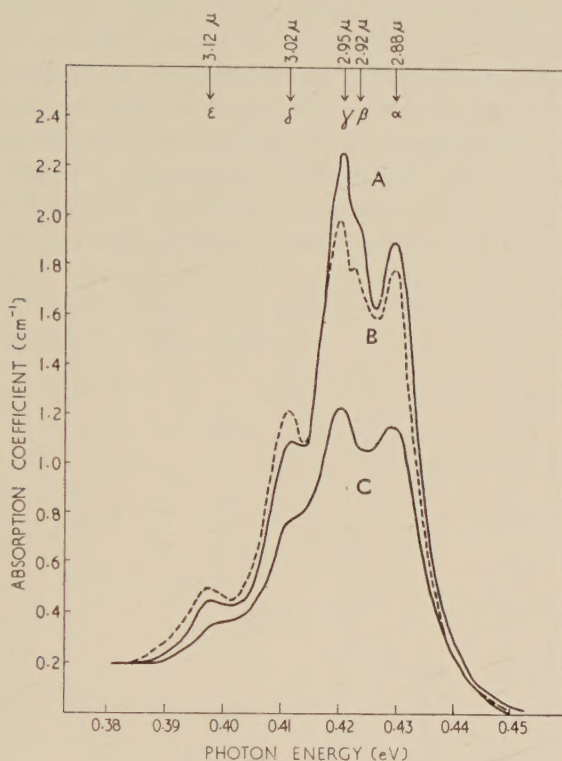
Absorption curves of unirradiated natural crystals (α-band strong).
A, Mitchell and Rigden, B, Drummond, C, Dreisch.

Fig. 2 (a)   Fig. 2 (b)

Absorption curves of unirradiated natural and synthetic crystals :
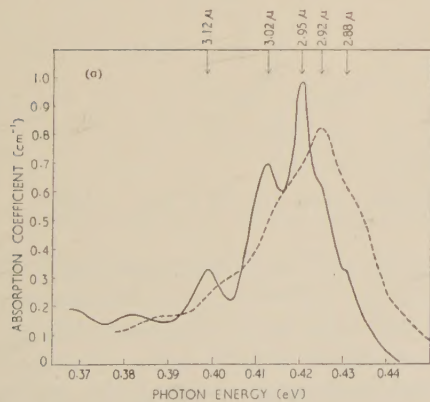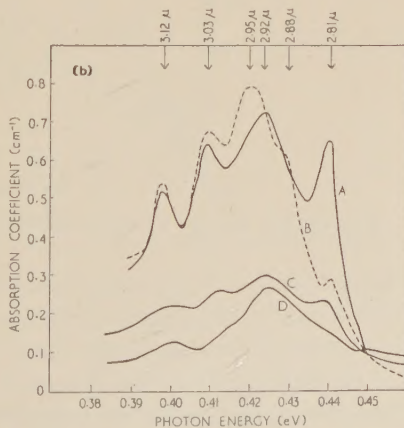   (a) Natural crystals, α-band weak ; —————————Mitchell and Rigden,
                                       — — — —Arnold.
    (b) Synthetic crystals : curves A and B, Mitchell and Rigden A–$E_\perp$
c-axis, B–$E_\parallel$ c-axis ; curves C and D, Arnold. (Assuming Arnold's
ordinate to be in cm^{-1}.)

Synthetic quartz sometimes has a broad absorption band at $3\cdot1\,\mu$ which has been attributed by Brown *et al.* (1952) to the presence of water inclusions. They found that crystals having this band also showed considerable Tyndall scattering of visible light, the scattering presumed to come from the inclusions. The synthetic quartz measured in the present work was cut from one of the high quality, low aluminium concentration (*ca.* $0\cdot01$ atom%) crystals now grown by Brown and Thomas (1956) and does not show the water inclusion band. Neither has this band been found in any of the natural crystals which we have examined.

Fig. 3
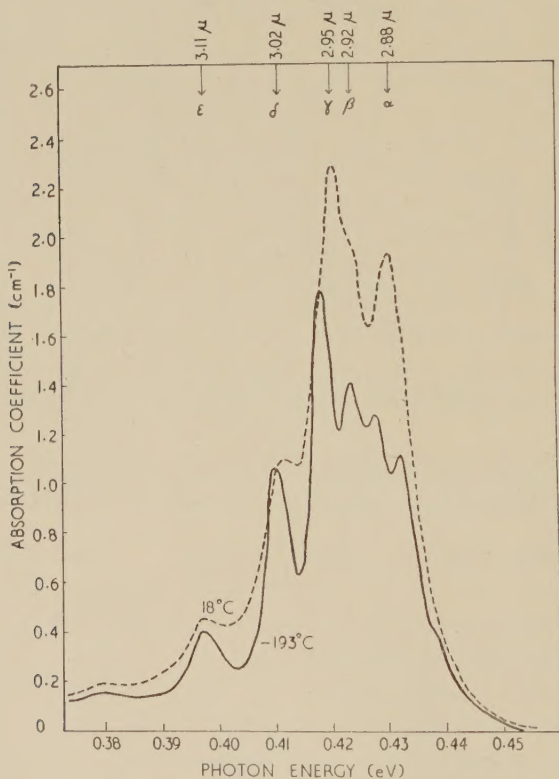
Absorption curves of unirradiated natural quartz at 18°c and −193°c.

Although free from water inclusions the synthetic specimen (fig. 2 (*b*)) did have a peak at $2\cdot81\,\mu$ which was not present in all the natural specimens. It seems likely that this corresponds to vibrational absorption of isolated O–H bonds as will be discussed below.

Increasing the resolving power of the instrument by using the grating improved the resolution of the peaks slightly and revealed some fine structure. Even using the rocksalt prism, however, the bands sharpened considerably when the specimen was cooled to −193°c as shown in fig. 3. At the low temperature β is clearly resolved and α appears as a doublet.

3.2. *Anisotropy of Absorption*

Drummond (1936) reported that the absorption around 3μ was aniso-tropic but his measurements were not made on the same specimen. The anisotropy is clearly shown in fig. 4, in which curve (A) refers to a measure-ment with light travelling parallel to the c-axis, that is with **E** always perpendicular to c, and curve (B) to light travelling perpendicular to the axis so that there are components of **E** parallel to c.

It will be seen from fig. 4 that $\mu_{\mathbf{E}_\perp} > \mu_{\mathbf{E}_{||}}$ where μ is the absorption coefficient. The ratio of these quantities can be determined without using polarizing devices if it can be once established that the absorption is isotropic about the c-axis and that the wavelength at the peak does not depend on the direction of **E**.

Fig. 4
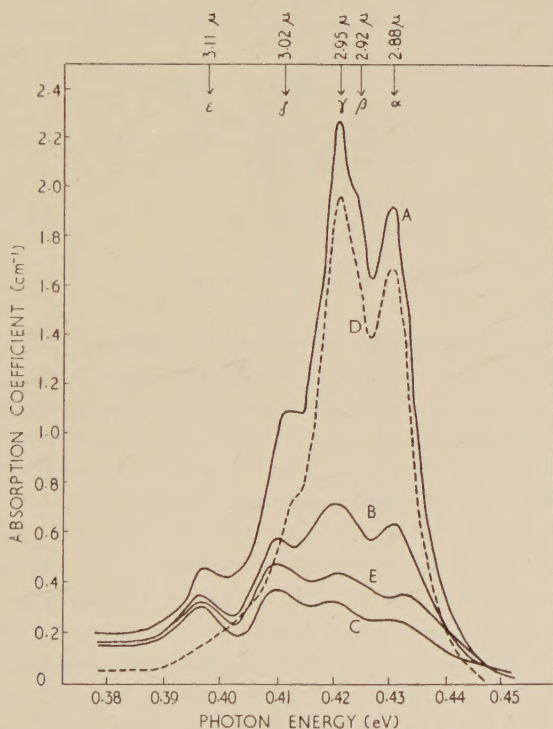
The anisotropy of the absorption bands in unirradiated natural quartz.

The absorption for all directions of **E** perpendicular to c was determined as follows. Light falling on the specimen was plane polarized by a 5 plate selenium polarizer. The crystal was mounted in a cell which could be rotated by a small electric motor, care being taken to ensure that the aperture was constant throughout the rotation. For wave-lengths of $2 \cdot 0$ and $2 \cdot 95 \mu$ the transmission was recorded as the specimen rotated. By rotating the crystal rather than the polarizer it was not necessary to make any correction for the variation of efficiency of the monochromator and detector for different directions of **E**. This

experiment showed that the transmission was constant to better than $\frac{1}{2}\%$ for all **E** perpendicular to c. It can be assumed therefore that the transitions are dipolar. That the position of the peak is independent of $\langle \mathbf{E} \rangle$ can be shown to sufficient accuracy by measuring with unpolarized light passing along and perpendicular to c.

We can now determine the transmission of the crystal for $\mathbf{E}_{\perp}c$ ($T_{\perp}$) and for $\mathbf{E}_{\parallel}c$ ($T_{\parallel}$) without using a polarizer, and independently of any selective polarization effects in the monochromator or the detector. Let $I_c(\mathrm{O})$ be the intensity of unpolarized light incident on the crystal in the direction $\mathbf{E}_{\parallel}c$, I_c the intensity transmitted by the crystal assuming that the reflection correction has been made, $I_p(\mathrm{O})$ and I_{p_1} the corresponding intensities when the light travels in a direction (1) perpendicular to c, $I_p(\mathrm{O})$ and I_{p_2} for a direction (2) perpendicular to c and (1), and k_1 and k_2 be the sensitivities, relative to some arbitrary direction, of the monochromator and detector for **E** parallel to (1) and (2) respectively. Then

$$T_c = \frac{\frac{1}{2}I_c k_1 + \frac{1}{2}I_c k_2}{\frac{1}{2}I_c(\mathrm{O})k_1 + \frac{1}{2}I_c(\mathrm{O})k_2} = \frac{I_c}{I_c(\mathrm{O})} = T_{\perp}$$

$$T_{p_1} = \frac{\frac{1}{2}I_p(\mathrm{O})T_{\perp}k_1 + \frac{1}{2}I_p(\mathrm{O})T_{\parallel}k_2}{\frac{1}{2}I_p(\mathrm{O})(k_1 + k_2)} = \frac{k_1 T_{\perp} + k_2 T_{\parallel}}{k_1 + k_2}$$

$$T_{p_2} = \frac{k_2 T_{\perp} + k_1 T_{\parallel}}{k_1 + k_2}$$

$$T_M = \frac{1}{2}(T_{p_1} + T_{p_2}) = (\tfrac{1}{2}T_{\perp} + T_{\parallel})$$

and $$T_{\parallel} = 2T_M - T_c.$$

For the most accurate measurements it is essential to use a beam of parallel light whereas in our experiments the beam was diverging. The main uncertainty in the measurements to be described, however, does not arise from the divergence but from the presence of overlapping bands.

Using this technique curve (C) in fig. 4 was obtained for the absorption spectrum for $\mathbf{E}_{\parallel}c$, the perpendicular case still being given by curve (A). The difference curve (D) shows that both α- and γ-bands are strongly anisotropic and that δ is probably anisotropic. The α and γ peaks are still present in the $\mathbf{E}_{\parallel}c$ curves but owing to the overlap of the bands and the uncertainty about the β-band we can only put a lower limit to the ratio ($\mathscr{A}$) of the absorption when the **E** is parallel to c, to that when **E** is perpendicular. Taking the peak values we find $\mathscr{A}_{\alpha} = 0.130$ and $\mathscr{A}_{\gamma} = 0.145$. If it is assumed that the absorption for $\mathbf{E}_{\parallel}c$ in the region of the α and γ peaks is composed only of α absorption and γ absorption, then resolving geometrically we find $\mathscr{A}_{\alpha} = 0.110$ and $\mathscr{A}_{\gamma} = 0.123$.

The final curve (E) in fig. 4 was obtained using the selenium polarizer. Using the polarizer alone the deflection from the detector was greater when **E** was horizontal than when vertical. Accordingly the polarizer was mounted to give **E** horizontal and the specimen mounted so that the light passed perpendicular to the axis with $\mathbf{E}_{\parallel}c$. The difference between curves (E) and (C) is due to the polarizer not being 100% efficient, the effect of the unpolarized component being enhanced by the high anisotropic ratio.

3.3. *The Effects of Irradiation*

Although the study of the effects of irradiation is made complicated by the overlapping band structure there are two unequivocal results

(*a*) None of the bands α–ε is continuously enhanced by pile irradiation.

(*b*) A new band (χ), which was briefly reported by Paige (1955), is induced at 0·444 ev (2·79 μ) by pile irradiation, the value of the peak energy at any time depending on the amount of overlapping from the lower energy bands.

Fig. 5
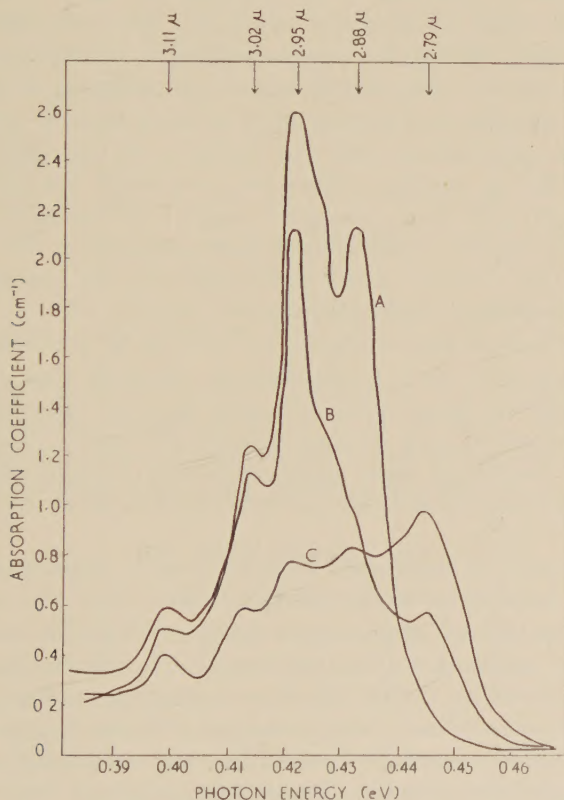
The effect of pile irradiation on the near infra-red absorption of natural quartz : curve A, unirradiated ; B, neutron dose $6·5 \times 10^{17}$ n° cm^{-2} ; and C, neutron dose 44×10^{17} n° cm^{-2}.

These two results are illustrated in fig. 5 in which absorption curves are plotted for two neutron irradiations. The visible colouring of this specimen due to aluminium impurity, Mitchell and Paige (1955), was at all times uniform.

It is also clear from fig. 5 that both α and γ decrease rapidly with pile irradiation. The extent to which these changes are due to ionization

effects has been investigated using ultra-violet illumination, x-ray and 2 Mev electron irradiation. Illuminating an untreated crystal with ultra-violet light from a high pressure mercury lamp had no effect on the absorption spectrum. Two opposite polished faces of another crystal were irradiated with x-rays from a copper target, the dose being *ca.* 10^7 r per face. This treatment had the effect of decreasing the α-band such that it was no longer resolved. The electron irradiation was carried out at the Tube Investments Research Laboratory, nr. Cambridge, using the 2 Mev Van de Graaff accelerator. The macroscopic temperature of the specimen during the irradiation was −80°C, the total electron dose being 950 (μA min cm^{-2}) or $3 \cdot 6 \times 10^{17}$ e^- cm^{-2}. This produced a very intense visible absorption band (A_1, A_2—associated with Al, Mitchell and Paige 1955) in the crystal and led to the decrease of absorption in the α–ε bands. The effects of ionizing radiation on the 3μ bands is exceedingly complex and further work is being carried out.

Approximate calculations, and the evidence of the visible colouring, show that as far as ionizing effects are concerned the above electron irradiation would give more ionization in the crystal than would have occurred during the pile irradiation of these specimens. It is concluded, therefore, that the χ-band, which is induced only by pile irradiation, is associated with atomic displacements.

The neutron dose corresponding to curve (B) in fig. 5 would be expected to induce about 10^{19} cm^{-3} displacements, Mitchell and Paige (1956), whereas for a displacement energy of 40 ev the 2 Mev electron irradiation would be expected to give of the order of 10^{16} cm^{-3}. Thus, although the χ-band is associated with displaced atoms, because its strength is small after pile irradiations we should not expect to see it after the electron irradiation.

Since the χ-band is associated with an atomic displacement the rate curve for the band is of considerable interest. For the neutron doses used during the present experiments (up to 50×10^{17} n° cm^{-2}) the rate of replacement collisions can be neglected. For effects associated with simple point defects we should therefore expect an approximately linear increase with neutron dose. The measured rate curve is shown in fig. 6 and is clearly not linear, the slope continuously decreasing. In addition measurements have been made using a stack of five 0·2 mm. thick specimens which had received an estimated neutron dose of 80×10^{17} n° cm^{-2}. The χ-band could just be detected. These specimens were irradiated for another purpose and were too small for accurate infra-red measurements. However, they show that the χ-band absorption is less than 1 cm^{-1} for this dose.

Because of the decrease of the α- and γ-bands the real rate of increase of the χ-band near the origin cannot be determined exactly. The lowest rate (A) is given by joining up the experimental points for the peak absorption and an estimated real rate, allowing for the decrease of the α- and γ-bands, is also shown (B).

In order to try to decide the axis of the χ centre we have determined the anisotropy of the χ-band. This was not possible with any accuracy until after the dose of $44 \times 10^{17}\ n^{\circ}$ cm^{-2}. Then the α- and γ-bands were sufficiently small and the radiation induced band (χ) sufficiently large

Fig. 6
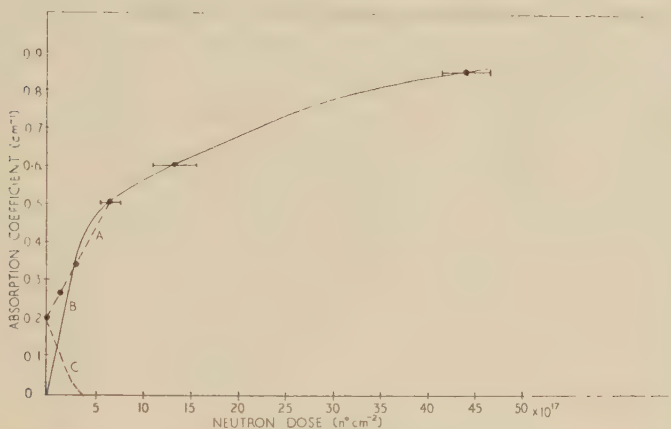
Rate curve for the χ-band induced by neutron irradiation. (Curve B is corrected for the decrease of α, assumed to be of the form C).

for a specific value of $\mathscr{A}_\chi$ to be measured. The curves are shown in fig. 7, from which a value of $\mathscr{A}_\chi = 0.71$ is obtained. The same reasons which made these curves suitable for determining $\mathscr{A}_\chi$ make them unsuitable for determining further values of $\mathscr{A}_\alpha$ and $\mathscr{A}_\gamma$.

§ 4. Discussion of Results

4.1. *The Origin of the 3 μ Group*

Several authors have suggested that these bands are harmonics and combinations of the fundamental lattice vibration frequencies. By choosing suitable combinations Plyler (1929) predicted wavelengths at which such bands would be expected to occur and some of the predictions corresponded to the observed peaks. Saskena (1940) in his detailed analysis of the vibrational spectrum of quartz comments that the 3 μ bands probably result from harmonics and combinations of the lattice vibrations. Arnold (1954) made the specific suggestion that the γ-band, which he found at 2·92 μ, is the third harmonic of the 8·7 μ Si–O vibration.

This type of explanation cannot be maintained, however, because of the wide variations in absorption strength of the bands in different crystals. In order to account for these variations it would be necessary to assume that about one half of the bonds were broken in some specimens during growth of the crystal, and in others, as the result of relatively weak irradiations during which only 10^{18}–10^{19} cm^{-3} defects would have been produced. Neither assumption is valid. In any case Arnold's

suggestion is ruled out by the large anisotropy of the γ-band ($\mu_{E_\perp}$ cm^{-1} > $\mu_{E_{||}}$) compared with $\mu_{E_\perp}$ = 0 for the 8·7 μ band.

It is necessary to assume, therefore, that the bands are associated with imperfections. None of the bands is progressively increased by pile irradiation—cf. the C-band, Mitchell and Paige (1956)—indicating that the original bands are not associated with displaced silicon or oxygen atoms, or the vacancies. Consequently it is likely that the defects responsible for the bands are impurity atoms, or are in some way associated with the presence of dislocations.

Fig. 7
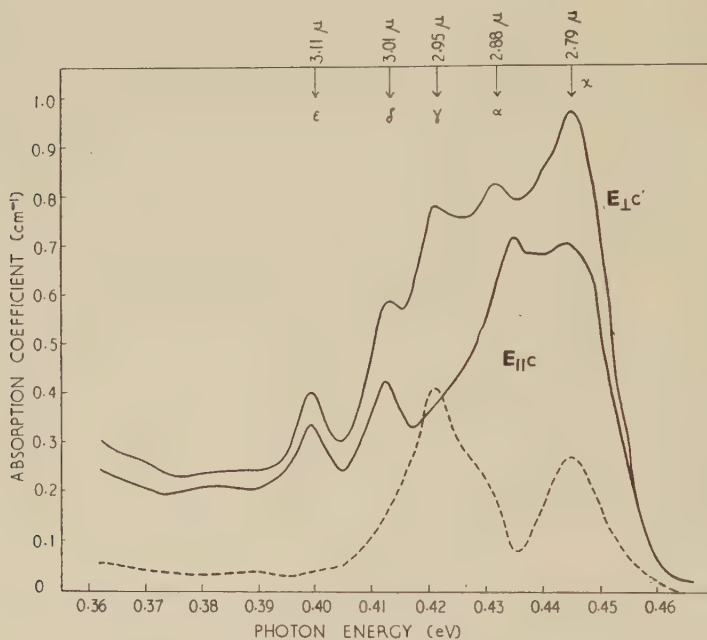
Anisotropy of the χ-band.

The measurements at low temperature showed that both α and γ decreased in total strength as the temperature was lowered. For electronic transitions involving at least one localized level in a solid the total absorption strength is generally independent of temperature. The observed decrease can be qualitatively accounted for in several ways:

(*a*) A normally forbidden electronic transition of an impurity, the atomic selection rule being relaxed in the crystal as a result of lattice vibrations—e.g. Cu in NaCl, Seitz (1951).

(*b*) A centre having three electronic levels, L, M and N such that the L–M transition is allowed but L–N forbidden. If there are in the ground state two electrons in each of L and M no absorption will be possible. When electrons from M have been thermally excited to N the L–M transition will be observed—the higher the population of N (higher temperature) the higher the strength of L–M absorption.

(*c*) A vibrational absorption associated with an impurity.

Regarding (*c*), the energies involved (*ca.* 0·4 ev) are high for impurity induced vibrations, and the absorption strength is too high for the bands to correspond to harmonics of a lower energy impurity induced vibration.

The normally forbidden transition (*a*) becomes allowed because in the real crystal the atomic wave functions (e.g. S_g, S_r) are modified, having to a limited extent the character which would give an allowed transition (e.g. S_g, $(S+\delta p)_r$). It is this which gives the transition probability of the observed band and we should expect the anisotropy to be characteristic of dipole rather than quadrupole transitions. An explanation of type (*a*) cannot be ruled out, therefore, on the grounds that α and γ absorption is isotropic for all directions of **E** perpendicular to the *c*-axis.

The centres giving rise to the 3 μ bands must have the property that, on capturing or losing an electron, the absorption—vibrational or electronic—is drastically reduced. For a centre of type (*b*), for example, a trapped electron would either go into N thereby inhibiting absorption or the levels would be modified giving absorption at some longer wavelength (cf. F–F′ in NaCl), with a consequent decrease at 3 μ.

To account for the differential changes in absorption which have been produced by cooling, by using polarized light and by irradiating with ionizing radiation it is necessary to assume that more than one type of centre must be contributing to the 3 μ absorption bands.

4.2. *The χ-Band*

It has been shown that the radiation induced band is associated with atomic displacements. The departure of the rate curve from linearity indicates that the rate of displacement of atoms cannot be the complete rate determining process. We conclude from this and from the tendency to a saturation value of absorption (fig. 6) that a product of damage is becoming associated with an impurity (or dislocation).

The peak absorption occurs at 2·79 μ (±0·01) which is close to the wavelength at which the O–H bond vibrational absorption occurs in vapours and weak solutions—e.g. 2·696 to 2·770 μ, Fox and Martin (1937), (1940). A strong band has been found in some specimens of fused quartz, and in glasses, at 2·75 μ and this band has been attributed to O–H vibrations—e.g. Ellis and Lyon (1937), Florence *et al.* (1953).

Quartz probably crystallized in nature by a hydrothermal process similar to that now used for producing synthetic quartz. Consequently hydrogen is a likely impurity and O–H bonds could be formed during irradiation by the combination of interstitial hydrogen and interstitial oxygen, or by hydrogen occupying silicon vacancies. The concentration of O–H bonds which would be required to account for the observed absorption strength can be calculated using the probability of absorption determined from the measurements on weak solutions. Kaye (1954) has given a mean value of the peak absorption per O–H bond in various solutions, and assuming an average width at half-absorption of 0·04 ev –based

on the measurements by Fox and Martin (1937), (1940)—we find a mean value of $(2\pm1)\times10^{21}$ O–H bonds (cm^{-3}) per unit integrated absorption expressed as $(\mu_{max}\times\Delta\mathbf{E})$ in cm^{-1} ev. The initial rate of increase of the χ-band, allowing for the effect of the decrease in the α- and γ-bands on both the rate and the bandwidth, is 2×10^{-3} cm^{-1} ev per 10^{17} n° cm^{-2}. This would be equivalent to the formation of 4×10^{18} (cm^{-3}) O–H bonds per 10^{17} incident neutrons per cm^{2}. Mitchell and Paige (1956) estimated that *ca.* 3×10^{18} displaced oxygen atoms and 1×10^{18} displaced silicon atoms are produced per 10^{17} n° cm^{-2}. If the rate of formation of O–H bonds was limited further by diffusion of the hydrogen or the displaced atoms then the observed rate should correspond to a lower limit for the rate of production of point defects. To an order of magnitude, therefore, the above interpretation is consistent with the observations. Further experiments are being carried out to determine whether the hydrogen concentration in quartz can be varied in a controlled manner by heat treatment, thus enabling more quantitative tests of the mechanism to be made.

Whatever the origin of the χ-band, the band which was resolved at $2\cdot81\pm0\cdot01\,\mu$ in unirradiated synthetic quartz (curve 1, fig. 2 (*c*)) is likely to be associated with O–H. This band is also resolved on one of Arnold's curves for synthetic quartz, while in unirradiated natural crystals we have sometimes detected changes of slope in absorption curves which could be associated with a band at about $2\cdot80\,\mu$. However, the anisotropy differs from that of the χ-band. For the χ-band $\mu_{\perp}$cm$^{-1}/\mu_{\parallel}$ cm^{-1} is $1\cdot4$ while for the $2\cdot81\,\mu$ band in unirradiated synthetic quartz $\mu_{\perp}/\mu_{\parallel}$ is at least greater than $2\cdot2$ (see fig. 1 (*c*)). It is possible, owing to the way in which the crystal was grown artificially with the major growth perpendicular to the *c*-axis, that O–H groups tend to be incorporated preferentially in the growth plane.

4.3. *The Anisotropy of the α-, γ- and χ-Bands*

For a set of $3n$ linear oscillators regularly arranged about the *c*-axis with which they make an angle θ, the anisotropic ratio $\mathscr{A}$ is $2\cot^{2}\theta$. If we have more than one set $3n_1, 3n_2\ldots\ldots$ making angles $\theta_1, \theta_2\ldots\ldots$ then

$$\mathscr{A}\equiv\frac{\mu_{\parallel}}{\mu_{\perp}}=\frac{\sum_x 3n_x\cos^2\theta x}{\sum_x n_x.3/2\sin^2\theta x}. \qquad \ldots\ldots (1)$$

Thus for defect oscillators having axes along Si–O directions for which $\theta_1=44^{\circ}$ 18', $\theta_2=66^{\circ}$ 15', $n_1=n_2=2$ the ratio $\mathscr{A}$ is $1\cdot06$. For the other simple directions, parallel to the following, the values are: *c*, $\mathscr{A}=\infty$; *a*, $\mathscr{A}=0$; nearest neighbour Si–Si, $\mathscr{A}=1\cdot06$; perpendicular to Si–Si through the common O, $\mathscr{A}=0\cdot74$; and perpendicular to the plane of the Si–O–Si triangles, $\mathscr{A}=1\cdot3$.

The anisotropic ratios which have been measured in the infra-red are: α, $0\cdot130$; γ, $0\cdot145$ and χ, $0\cdot71$. If each of these is interpreted as

being due to sets of oscillators at one angle θ, we find $\theta = 75°\ 42'$ for the α-band, $74°\ 57'$ for γ and $59°\ 12'$ for the χ-band.

As far as α and γ are concerned there is the possibility that the oscillators lie in planes parallel to (001)—e.g. linear oscillators along the *a*-axis tunnels—and that the measured anisotropy differs from zero because of a combination of beam divergence, misorientation of the crystal and thermal vibration of the axis out of the plane.

The beam of light used in the experiments was diverging with a maximum semi-angle of $\phi = 2°$. Thus for light nominally travelling perpendicular to *c* and having **E** nominally parallel to *c* we have contributions **E** $\sin \phi$ capable of exciting the centres. In the case of **E** nominally perpendicular to *c* the effective **E** becomes **E** $\cos \phi$, so that for a prism shaped light path in the crystal

$$\mathscr{A} = \int_{-\phi}^{\phi} \tfrac{1}{2} \tan^2 \phi \, d\phi,$$

which is negligible for a divergence of $\pm 2°$. Possible errors due to misorientation, including cutting and mounting, were less than $2°$. The effect of temperature on the anisotropy cannot be easily determined. The difficulty is that the uncertainty in the anisotropic ratios, leading to the values of $0\cdot123$ and $0\cdot145$ being considered as upper limits, arises because of the uncertainty in determining the amount of α and γ present in the $\mathbf{E}_\parallel c$ case when both α and γ are small and overlapping. At low temperatures the α and γ bands are reduced and this makes the determination of the anisotropic ratio more difficult.

The 'thermal spread' suggestion cannot be ruled out experimentally at present, although the angular variations required to account for the results (a mean of $\pm 15°$ to give observed upper limit of $\mathscr{A} = 0\cdot13$) would have to correspond to approximately $0\cdot5$ Å displacement out of the plane.

There are two directions between well defined points in the structure which make about the required angle to the *c*-axis. Oxygen atoms (9), (5), (4w) and (7b)—using the numbering of atoms shown on fig. 8—form a tetrahedron, and a similar tetrahedron is formed by the oxygen atoms (7b), (8b), (6b) and (4). If P and P' are respectively the points which are equidistant from the atoms in each of these tetrahedra, then PP' makes an angle of $67°$ with the *c*-axis. For an oscillator in such a direction $\mathscr{A} = 0\cdot36$ compared with the observed upper limits of $0\cdot130$ and $0\cdot145$.

The second direction is one of the O–O directions. The O–O directions are : 6 similar to (5) to (8), $78°\ 50'$ with *c*, oxygens separated by $2\cdot60$ Å; 6 similar to (5) to (6), $47°\ 3'$ with *c*, $2\cdot64$ Å : 3 similar to (6) to (8), $60°\ 44'$, $2\cdot65$ Å ; and 3 similar to (5) to (7), $27°\ 49'$, $2\cdot60$ Å. Taken together and using eqn. (1) the anisotropic ratio is $1\cdot02$. Taking the directions between the closest oxygens—viz. directions making $78°\ 50'$ and $27°\ 49'$ with *c*, the ratio is $0\cdot80$. By itself the $78°\ 50'$ O–O direction gives a value for the anisotropy of $0\cdot078$, which is consistent with the observed limits. It is not clear, however, if the centre is diatomic, how the axis is parallel to

this particular O–O direction, or if the centre is a simple impurity how the directed wave function has its axis in this direction, rather than being distributed about the four O–O directions. The same difficulty was noted by O'Brien (1955) when explaining the anisotropy of some of the paramagnetic resonance effects associated with aluminium impurity in quartz. To account for the quadrupole effects Miss O'Brien had to assume that only two of the possible four oxygen atoms surrounding a given aluminium were suitable for the formation of the colour centre.

Fig. 8
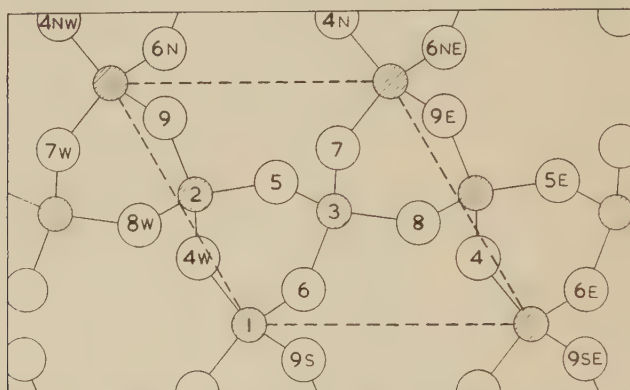
Projection of atom positions in α quartz on to a (001) plane. Atoms in the unit cells below those shown are given a suffix b.

The χ-band appears to be related to the association of a product of damage with an impurity. The simplest possibilities are shown in the table. We have omitted from this table the combinations of an impurity substituted for silicon with interstitial silicon or oxygen atoms, and of an impurity substituted for oxygen with interstitial silicon or oxygen atoms. There are large numbers of such directions and a random distribution of defect-pairs will tend to be isotropic.

The values of anisotropic ratio given in the table were calculated from eqn. (1). In calculating the ratio for interstitial pairs we have assumed that these are distributed between the major tunnels in the structure—those parallel to the c-axis, and those parallel to a-axes. For the rhombohedral unit cell there are 3 a-axis tunnels per cell, and 1 c-axis tunnel. The c-axis tunnels are 1·1 times longer than those along the a-axes so that we take $\mathscr{A} = 1 \cdot 1/(3/2) = 0 \cdot 73$, in good agreement with the measured value of $0 \cdot 71 \pm 0 \cdot 04$. All the other values given in the table differ significantly from the observed ratio.

There is, however, a further possibility to be considered that the observed transition is associated with a wave function directed at right angles to the principal axis of the centre. For example, the tightly bound electrons of the centre may have p-function components parallel

to the principal axis, while the observed transition may be associated with a less tightly bound electron having a p-function perpendicular to the main axis. In particular, a centre comprising a substitutional impurity in a silicon position adjacent to a silicon vacancy, would give an anisotropic ratio of 0·74 for the perpendicular direction passing through the nearest oxygen. This direction can also account for the observed ratio.

Anisotropic ratios for some impurity/damage combination centres. Where the centre can occur equally in several directions values are given for the mean and also for each of the directions assuming that all the centres are in one direction.

Position of impurity	Damage product	Principal axis, θ	Anisotropic ratio	
Substituted for Si	Si vacancy	54°	1·06	
	O vacancy	44° 18′	1·06	(2·10)
		66° 15′		(0·39)
Substituted for O	Si vacancy	44° 18′	1·06	(2·10)
		66° 15′		(0·39)
	O vacancy	27° 49′		(7·18)
		47° 3′	1·02	(1·75)
		60° 44′		(0·63)
		78° 50′		(0·08)
Interstitial	Interstitial Si or O	0°	0·73	(∞)
		90°		(0)

§ 5. Conclusions

The experiments have shown that the 3 μ group of bands is associated with imperfections in the crystal and that the imperfections concerned are not interstitial silicon or oxygen atoms, nor silicon or oxygen vacancies. At least two centres are required to account for the various differential changes in absorption strength. The absorption in the 3 μ bands is modified by the electron and hole trapping which accompanies the passage of ionizing radiation through the crystals.

Two of the bands are very anisotropic and the important axes associated with the observed transitions are 75° 42′ (α) and 74° 57′ (γ) from the c-axis, assuming that all the oscillators of each kind make the same angle with the c-axis. This could correspond to a direction parallel to one of

the nearest neighbour O–O directions but there is no other evidence to show how one such direction should be preferred to the other three O–O directions.

The radiation induced band is associated with atomic displacements and their combination with some imperfection—possibly hydrogen impurity. The anisotropy of this band can be accounted for if the centre is a combination of an interstitial oxygen, or silicon, atom with an interstitial impurity. Thus the anisotropy is consistent with the O–H model. Alternatively, agreement with the observed anisotropic ratio is found for an oscillator having an axis in a direction perpendicular to a line joining two neighbouring silicon positions and passing through the nearest oxygen atom.

Acknowledgments

References

Arnold, G. W., 1954, *J. chem. Phys.*, **22**, 1259.
Brown, C. S., Kell, R. C., Thomas, L. A., Wooster, N., and Wooster, W. A., 1952, *Miner. Mag.*, **29**, 858.
Brown, C. S., and Thomas, L. A., 1956, *Proc. Inst. elect. Engrs.*, **104**, 174.
Dreisch, T., 1927, *Z. Phys.*, **42**, 426.
Drummond, D. G., 1936, *Proc. roy. Soc.* A, **153**, 328.
Ellis, J. W., and Lyon, W. K., 1937, *Nature, Lond.*, **139**, 70.
Florence, J. M., Glaze, F. W., and Black, M. H., 1953, *J. Res. nat. Bur. Stand.*, **50**, 187.
Fox, J. J., and Martin, A. E., 1937, *Proc. roy. Soc.* A, **162**, 419 ; 1940, *Ibid.*, **174**, 234.
Kaye, W., 1954, *Spectro chim. Acta*, **6**, 257.
Mitchell, E. W. J., and Paige, E. G. S., 1955, *Phil. Mag.*, **46**, 1353 ; 1956, *Ibid.*, **1**, 1085.
O'Brien, M. C. M., 1955, *Proc. roy. Soc.* A, **231**, 404.
Paige, E. G. S., 1955, *Thesis*, University of Reading.
Plyler, E. K., 1929, *Phys. Rev.*, **33**, 48.
Plyler, E. K., and Peters, C. W., 1951, *J. Res. nat. Bur. Stand.*, **45**, 462.
Saskena, B. D., 1940, *Proc. Indian Acad. Sci.* A, **12**, 93.
Seitz, F., 1951, *Rev. mod. Phys.*, **23**, 328.

Proportional Counter Measurements of π-Mesonic X-Rays†

By D. West and E. F. Bradley

Atomic Energy Research Establishment, Harwell

Abstract

A xenon filled proportional counter has proved to be a very useful instrument for the study of π-mesonic x-rays from light elements. Measurements of the K_α energies from ^{6}Li, ^{7}Li, ^{9}Be, ^{10}B and ^{11}B are described. Energy shifts due to the short range pion-nucleon forces are observed, confirming the scintillation counter measurements.

The experimental values of the energy shift are fitted equally well by the theories of Deser *et al.* (1954) or Karplus (1956).

Measurements of L_α energies are used to deduce a value for the π-meson mass equal to $272.5 \pm 0.8\,m_e$.

The natural broadening of the beryllium K_α line due to the short lifetime for capture of the π-meson from the 1s state has been measured. A width $\Gamma = 1.2 \pm 0.2$ kev was observed.

Intensity ratios of K_α and K_β and L_α, L_β and L_γ lines are also reported.

§ 1. Introduction

π-mesonic x-rays were first detected by Camac, McGuire, Platt and Schulte (1952). Later work by McGuire *et al.* (1954), and by Stearns, DeBenedetti, Stearns and Leipuner (1954), established that the yield of the K series x-rays decreased rapidly with increasing Z due to capture from the 2p level, and was barely detectable above Z=9.

The first accurate measurements of the energies of the K x-rays were made by means of critical absorbers in conjunction with a measurement of the pulse height distribution from the x-rays with a sodium iodide scintillator. Stearns, Stearns, DeBenedetti and Leipuner (1954), showed that the energies of the K_α x-rays from lithium and beryllium were definitely lower than the values calculated from purely electromagnetic interactions. Later, improvements in the technique enabled direct measurements of energy to be made from pulse height distributions obtained with a NaI scintillator. Stearns, Stearns, DeBenedetti and Leipuner (1955), Camac, McGuire, Platt and Schulte (1955) and Stearns and Stearns (1956 a) measured the energies of π-mesonic K x-rays for elements up to fluorine and obtained energy values which were in all cases lower than those calculated from purely electromagnetic interactions. The energy shifts are due to the short range forces between pions and

---

† Communicated by the Authors.

nucleons and the observed shifts were in qualitative agreement with a theory of Deser *et al.* (1954) discussed below.

In the case of the lighter elements the energy resolution of the scintillation counter is not small enough to resolve the $K_\alpha (2p \to 1s)$ and $K_\beta (3p \to 1s)$ lines. This is well within the capabilities of the proportional counter whose resolution is at least four times narrower than that of the scintillation counter. It was therefore desirable to repeat these measurements with a proportional counter. Moreover the improved resolution enabled the natural broadening of the 1s level in beryllium to be measured for the first time. The level broadening arises from the short lifetime for capture of the π-meson in the 1s state. Measurements of the energies of L_α x-rays were also carried out and the relative intensities of K_α and K_β and also L_α, L_β and L_γ radiations can be estimated.

The first results obtained with proportional counters were described in a letter, West and Bradley (1956 a) and interim accounts of the present work were presented at the 6th Rochester Conference 1956 and the CERN Symposium 1956 .

§ 2. The Proportional Counter

The two main requirements of the proportional counter were a high efficiency for detecting x-rays combined with a low background counting rate. It was therefore made capable of withstanding pressure and was filled to 3 or 5 atmospheres pressure with xenon. To reduce the background counting rate due to general radiation from the cyclotron, the active length of the counter was kept to a minimum, which required the use of field tubes of the type described by Cockroft and Currant (1951). A diagram of the counter is shown in fig. 1. It was made of aluminium

Fig. 1
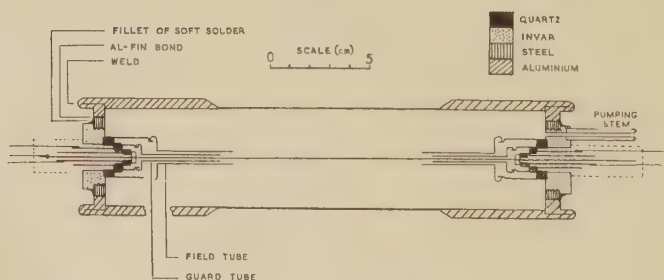
Diagram of the proportional counter.

and opposite the active region of the counter the wall was turned down to 0·030 in. to minimize absorption of x-rays. The field and guard tube assemblies were of the type described by Batchelor *et al.* (1955). They were bonded with ' araldite ' to invar plugs which were screwed and soft soldered into the steel core of a section of ' Al-fin ' the aluminium outer portion of which was argon arc welded to the counter body. The

inside of the counter wall was finely polished and then oxidized in the manner described by Wilkinson (1950) for Geiger counters.

It had previously been noticed that the uniformity of the counter wire was very important in pressurized proportional counters. The wire used here (0·005 in. Cu–Ni alloy) was specially prepared by Johnson and Matthey Ltd. using a freshly prepared diamond die. The uniformity of multiplication factor was tested by measuring the pulse height distribution due to the 59·6 kev γ-rays from ^{241}Am with the source placed at different positions along the counter and round its axis. With a filling consisting of 3 atmospheres pressure of xenon +3 cm of Hg pressure of methane, the counter gave a multiplication factor which was uniform over the active volume to better than half of one per cent when the field tube potential was correctly adjusted.

The counter operated with an H.T. voltage of ∼ 5000 volts on the wire and amplifier integration and differentiation time constants of $3\,\mu$ sec were used. It was necessary to embed the external portion of the field tube assembly in ceresin wax to eliminate electrical breakdown. The energy resolution, measured with 59·6 kev γ-rays was 2·9% (half width at half maximum) and is only slightly worse than the best resolution obtainable (2·5%) with low pressure fillings. The filling gas was occasionally repurified over heated calcium, or over a sodium mirror, during the series of measurements when the energy resolution had deteriorated slightly.

Fig. 2
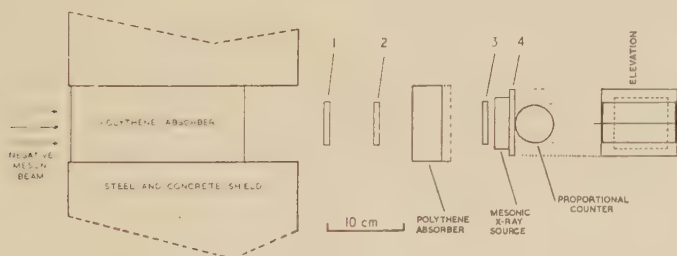
Diagram of the experimental arrangement.

§ 3. Experimental Method

Negative mesons from the Liverpool Synchrocyclotron entered the apparatus shown in fig. 2. Counters 1, 2 and 3 are plastic scintillators 2·5 in. × 2·5 in. × 0·25 in. viewed by 2 in. photomultipliers in contact with a small face of the scintillator. Counter 4 is a plastic scintillator 4 in. × 3·5 in. × 0·15 in. It was used as an anticoincidence counter and to obtain a maximum efficiency it was viewed by two photomultipliers in contact with the small faces at opposite sides of the crystal. The two multipliers had independent H.T. supplies and their outputs were mixed via cathode followers. The anticoincidence scintillation counter completely covered the active region of the proportional counter. π-mesons which stopped in the target material were selected by means of a

coincidence between the output of counters 1, 2 and 3 (resolving time 0·3 μsec) in anticoincidence with the output of counter 4. (123–4 event.)

The fraction of these events which gave a pulse in the proportional counter was further selected by means of a triple coincidence between counters 1, 2 and 3 in coincidence with a proportional counter pulse and in anticoincidence with the output of counter 4. (123 Prop.–4, event.) An event of this type opened a gate 11 μsec in duration which allowed the proportional counter pulse to pass to a 70 channel pulse analyser of the Hutchinson Scarrott type.

Tests with α, γ coincidences from ^{241}Am, detecting the α-particles with a scintillation counter and the γ-rays with a proportional counter, showed that a maximum coincidence rate was obtained with 2 μsec resolving time when the α-particle pulses were delayed by 2 μsec. Accordingly the triple coincidence pulse from the scintillation counter telescope was delayed by this amount before mixing with the proportional counter pulse. (With a 5 atmosphere filling 3 μsec delay and 4 μsec resolving time were used.)

The negative meson beam consisted of π-mesons of energy 96 Mev together with 6% of μ's and 4% electrons having the same momentum and therefore a longer range than the π's. An absorber was placed in the beam and its thickness adjusted to give a maximum number of π-mesons stopped in the target. Polythene was used to minimize scattering and the last few inches were inserted between counters 2 and 3 enabling the 12 coincidence rate to be used as a monitor when determining the stopped meson rates. The mesonic x-ray sources were $2\frac{3}{4}$ in. $\times 2\frac{3}{4}$ in. with a thickness of ~ 2 g/cm^2 which was known to give only a small amount of backscattered Compton radiation. When powders were used they were compressed into thin aluminium boxes weighing a few grammes by means of a hydraulic press. With the optimum absorber thickness, approximately 0·6 of the π-mesons were stopped by the target material.

In addition to 12 feet of concrete and steel shielding between the cyclotron and experimental rooms, a cave of concrete and iron 2 ft thick and open at the rear was constructed round the apparatus. The meson beam was magnetically deflected so that direct radiation from the cyclotron could not pass through the apparatus.

The counting rate which could be accepted was limited by the single rate in the proportional counter. Above about 6000 c.p.m., which corresponds to a mean rate of one proportional counter pulse per cyclotron pulse, some broadening and additional background was observed in the spectra. This was presumably caused by pile up of consecutive pulses and throughout the measurements the proportional counter single rate was never allowed to exceed 6000 c.p.m. The duration of the cyclotron pulse was ~ 100 μsec and as an additional precaution a paralysis time of 100 μsec was put on the gating pulse and in the later measurements a paralysis of 200 μsec was put on the proportional counter channel of the coincidence unit.

Table 1 gives a typical set of counting rates used in a measurement of the beryllium K_α line together with the corresponding values in a scintillation counter experiment (Stearns and Stearns, private communication).

The overall efficiencies of the proportional counter and scintillation counter are comparable, but the counting rates which can be accepted are much smaller in the case of the proportional counter. The background of very large pulses in the detectors is much smaller with the proportional counter presumably due to its smaller stopping power. A major part of the background was associated with the (123–4) rate obtained without the target. This rate was usually about 0·5 to 0·75 times that due to the target. It arose from mesons which stopped in the third scintillator and in the part of its photomultiplier and case which was exposed to the beam.

Table 1.   Comparison of Proportional Counter and Scintillation Counter
Experiments

	Proportional counter	Scintillation counter
Coincidence resolving time in the detector channel	2 μsec	0·05 μsec
Gate length	11 μsec	2·0 μsec
Detector single rate	4100 c.p.m.	$\sim$ 12000 c.p.m.
Stopped meson rate	1070 c.p.m.	16000 c.p.m.
Gating rate	41 c.p.m.	900 c.p.m.
Estimated casual rate	2·6 c.p.m.	< 20 c.p.m.
Gated pulses comprise :		
Mesonic x-rays	16 c.p.m.	$\sim$ 160 c.p.m.
Background on scale	12 c.p.m.	$\sim$ 140 c.p.m.
Background off scale	13 c.p.m.	$\sim$ 600 c.p.m.

Energy calibrations were carried out with radioactive K x-ray sources. The proportional counter pulse was made to produce a gating pulse by feeding it into the channel usually fed by the triple pulse from the counter telescope as well as into its own channel, the anticoincidence counter being disconnected. The source was placed midway along the counter, the uniformity measurements already referred to having indicated that the multiplication factor for a source at this point differed by only a very small amount, <0·1%, from the mean value over the whole effective region of the counter.

§ 4. Energies of π-Mesonic K_α X-Rays

Runs of up to 10 hours duration were needed to obtain an adequate number of counts in the spectra of K_α x-rays. As a check on drifts in gain during these long periods, energy calibrations were carried out every two hours. The standard deviation of the mean value of the

position of the calibration peak, which represents the uncertainty in the measurements due to drifts, usually amounted to less than 0.25%.

Spectra of K x-rays from natural lithium, ^{9}Be, ^{10}B (95%) and ^{11}B (82%) are shown in figs. 3–6 †. K_β peaks are seen clearly resolved in the spectra of lithium and beryllium x-rays.   The boron spectra, taken with a counter filled to 5 atmospheres pressure of xenon to obtain an increased efficiency, also contain peaks due to boron μ K x-rays and aluminium

Fig. 3
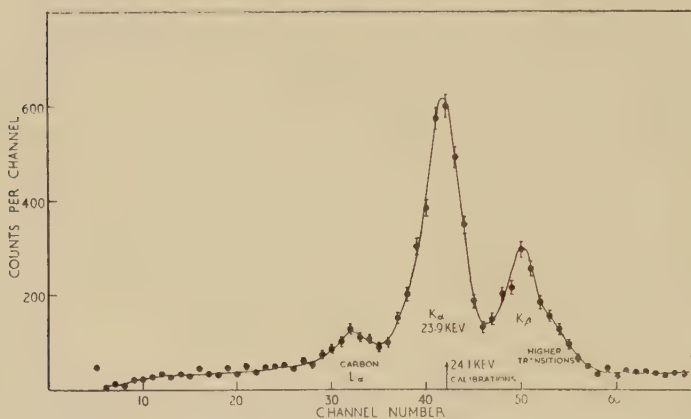
Pulse size distribution of π-mesonic K x-rays from lithium $(93\%\ ^7\text{Li},\ 7\%\ ^6\text{Li})$.

Fig. 4
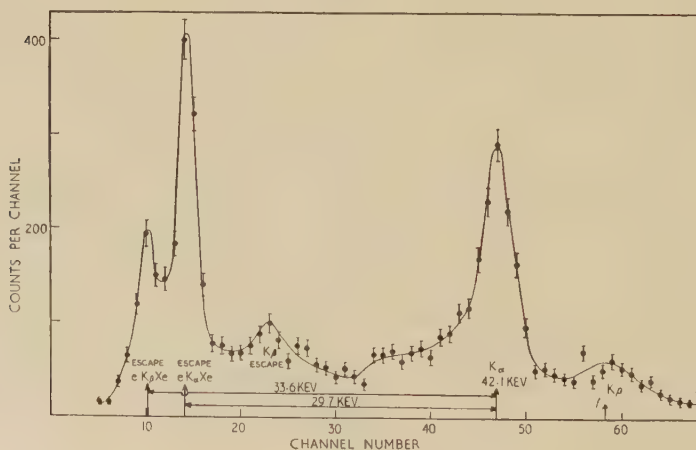
K x-rays from beryllium.

† For incident radiations of energy greater than the K electron binding energy of xenon (34.6 kev) prominent 'escape peaks' occur in the spectra when the K_α (29.7 kev) or K_β (33.6 kev) radiations of xenon escape from the counter.

M x-rays from the material of the source box. For elements of higher atomic number, the yield of x-rays and the efficiency of the counter were too low for worthwhile measurements to be made. Peak positions were determined from free hand drawings through the experimental points by two observers, the mean position being used. Only the K_α

Fig. 5
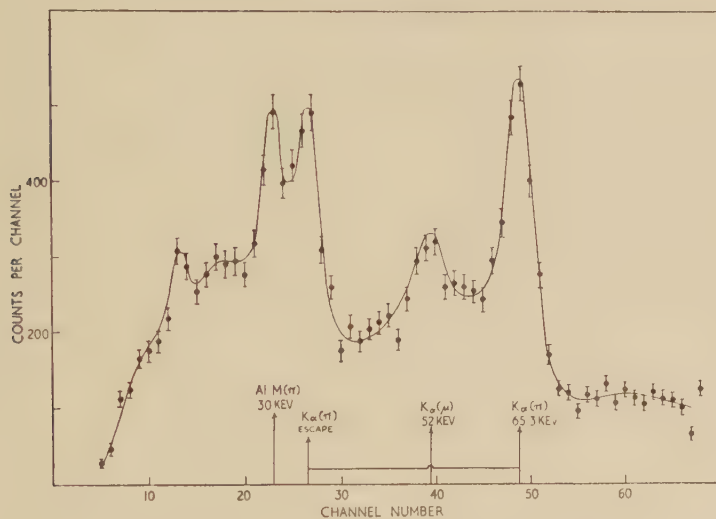
K x-rays from ^{10}B (95% ^{10}B, 5% ^{11}B).

Fig. 6
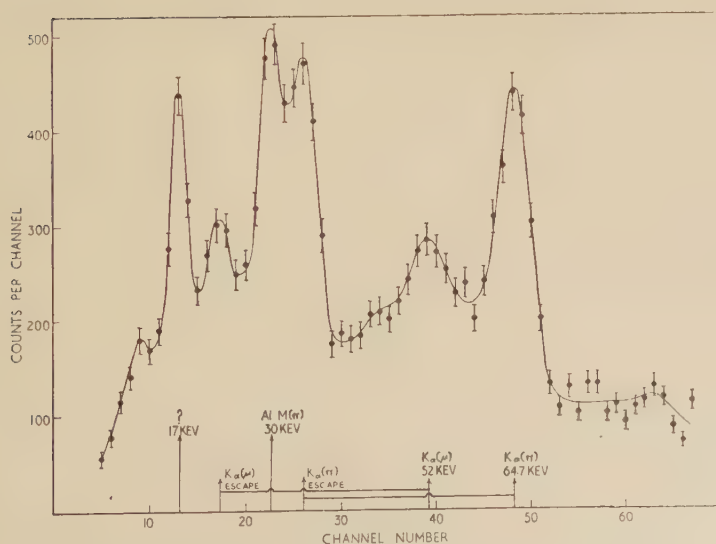
K x-rays from natural boron (82% ^{11}B, 18% ^{10}B).

peaks were measured as there is evidence of unresolved higher transitions in the K_β peaks. Table 2 lists the energy values obtained. The mean value quoted is the mean of the individual values weighted by the number of counts in the peak in each case. The errors given are estimated ones based on the uncertainty in the peak position, and random drifts. They are somewhat larger than the r.m.s. errors derived from the internal consistency of the results. Values of the K_α energies of individual isotopes are derived from the measurements by means of the relation

$$E = a_1 E_1 + a_2 E_2$$

where E is the energy observed with the mixture of isotopes, E_1 is the energy corresponding to the isotope having a percentage abundance a_1, and similarly for E_2 and a_2. In each case the correction due to the admixture of the second isotope is very small.

In table 3 the derived K_α energies for individual isotopes are given together with the values obtained by Stearns and Stearns (1956 a) and, the theoretical values ($m_\pi = 272 \cdot 8 \, m_e$) neglecting the short range pion nucleon interaction but including finite nuclear size and vacuum polarization corrections. The agreement with Stearns' values is excellent except in the case of ^{11}B and confirms the existence of an energy shift due to the short range pion nucleon interaction. As can be seen from fig. 6 there are no signs on the proportional counter spectra of any additional lines above the K_α peak which could affect the measured energy in the case of ^{11}B. The sample used was of $99 \cdot 5 \%$ purity and showed no signs of a peak at 74 kev due to $M_g \, L_\alpha$ rays, which was prominent when less pure samples were employed.

The energy shift, which is due to short range interactions between the pion and the nucleus, has been calculated by Deser *et al.* (1954) in terms of the interaction of the pion with single nucleons summed over all the nucleons in the nucleous.

Brueckner (1955), considered in addition the interaction of the pion with two nucleons, the process leading to star formation, and predicted energy shifts approximately 1·5 times as large. Karplus (1956), pointed out that the additional shift predicted by Brueckner is very sensitive to the momentum distribution of nucleons within the nucleus. He favoured a distribution giving a smaller shift than Brueckner's.

The percentage shift in energy given by Deser *et al.* is

$$\frac{\delta E}{E_{K_\alpha}} = -\frac{4}{3}\frac{\mu}{\bar{\mu}} \cdot \frac{4Z}{r_B} \left\{ \frac{2}{3} Z a_1 + \frac{3N+Z}{3} a_3 \right\}$$

where a_1 and a_3 are the pion nucleon s scattering lengths for isotopic spin states 1/2 and 3/2 respectively, r_B is the mesonic Bohr radius and μ and $\bar{\mu}$ are the reduced masses of the pion nucleus and pion single nucleon systems.

The percentages energy shifts given by this equation, using the values $a_1 = 0 \cdot 167 \pm 0 \cdot 012 \, \lambda_\pi$ and $a_3 = -0 \cdot 105 \pm 0 \cdot 010 \lambda_\pi$ (Orear 1956), where λ_π is the π-meson Compton wave-length, are given in table 4 together with the experimental values. The calculated shift depends very nearly on

Table 2. Measured Energies of π-Mesonic K_α Lines

Element and isotopic constitution	Energy calibration used	Measured values of π-mesonic K_α energy (kev)	Mean observed K_α energy (kev)
Lithium Enriched in lithium 6	24·13 kev† (^{113}Sn)	4 determinations	
Lithium (^{7}Li 92·5%) (^{6}Li 7·5%)	24·13 kev† (^{113}Sn)	23·5$_8$ 23·9$_1$ 23·8$_9$ 23·9$_1$ 24·0$_7$	23·88 ± 0·1
Beryllium ^{9}Be 100%)	41·31 kev (^{153}Gd)	42·0$_4$ 42·0$_7$ 41·9$_9$ 42·1$_2$ 42·2$_7$‡ 42·3$_1$‡	42·15 ± 0·15
Boron (^{10}B 95%) (^{11}B 5%)	72·19 kev (^{203}Hg)	65·7$_7$ 64·6$_3$ 65·4$_5$ 64·9$_2$ 65·2$_1$ 65·3$_7$	65·27 ± 0·4
Boron ^{11}B 81·6%) ^{10}B 18·4%)	72·19 kev (^{203}Hg)	64·4$_8$ 64·5$_6$ 64·8$_3$ 64·8$_5$ 64·4$_1$	64·65 ± 0·3

† A critical absorber (silver) removed the K_β radiation.
‡ Measurement of the escape peak.

Table 3. Measured and Calculated Energies of π-Mesonic K_α Lines

Isotope	Measured K_α energy (kev) present work	Measured K_α energy (kev) (Stearns and Stearns 1956 a)	Calculated K_α energy (kev) (E.M. effects only) $m_\pi = 272\cdot8\ m_e$
^{6}Li	24·31 ± 0·1		24·53
^{7}Li	23·85 ± 0·1	23·77 ± 0·12	24·61
^{9}Be	42·15 ± 0·15	42·09 ± 0·1	43·95
^{10}B	65·3 ± 0·4	65·2 ± 0·2	68·75
^{11}B	64·5 ± 0·3	63·5 ± 0·2	68·82

$a_1 + 2a_3$ and thus involves a small difference between two quantities. The resulting errors in the calculated shifts are considerable†. The Brueckner theory predicts an additional percentage shift $Z^2/985 \cdot 4/3$ and the corresponding values, together with those of Karplus and Halpern (1957), given in table 4 are subject to a similar uncertainty.

Table 4.   Measured and Calculated Energy Shifts

Isotope	Observed energy shift present results	Observed energy shift Stearns and Stearns (1956)	Calculated Deser *et al.*	Calculated Brueckner	Calculated Karplus‡
	%	%	%	%	%
^{6}Li	0.9 ± 0.4		1.1 ± 0.5	2.3 ± 0.5	1.4 ± 0.5
^{7}Li	3.1 ± 0.4	3.4 ± 0.5	2.5 ± 0.7	3.7 ± 0.7	3.1 ± 0.7
^{9}Be	$4.1 \pm 0.3_5$	$4.2 \pm 0.2_5$	3.9 ± 1.1	6.2 ± 1.1	4.9 ± 1.1
^{10}B	5.0 ± 0.6	5.15 ± 0.3	3.2 ± 1.6	6.6 ± 1.6	3.9 ± 1.6
^{11}B	$6.3 \pm 0.4_6$	7.8 ± 0.3	5.5 ± 1.7	8.9 ± 1.7	6.9 ± 1.7

‡ Taken as 1.25 times the values of Deser *et al.*

Table 5.   Comparison of the Theories

Theory	$a_1 + 2.23a_3$ Prop. counter results	$a_1 + 2.13a_3$ Stearns and Stearns scintillation counter results
Deser *et al.*	$-0.079 \pm 0.004\lambda_\pi$	$-0.069 \pm 0.002\lambda_\pi$
Karplus	$-0.063 \pm 0.003\lambda_\pi$	$-0.055 \pm 0.002\lambda_\pi$
Brueckner	$-0.033 \pm 0.005\lambda_\pi$	$-0.023 \pm 0.002\lambda_\pi$
Orear's value	$-0.067 \pm 0.023\lambda_\pi$	$-0.057 \pm 0.022\lambda_\pi$

The uncertainties in the calculated values of the energy shifts makes a clearcut discrimination between the theories impossible.

To illustrate this the experimental shifts from all the isotopes were added and a value for $a_1 + 2.23a_3$ was deduced according to the three theories. These values are given in table 5 together with the value of the same quantity derived from Orear's values of a_1 and a_3. Stearns' data, which includes measurements up to $Z = 9$, gives values of $a_1 + 2.13a_3$ also included in table 5.

Thus both the theories of Deser *et al.* and Karplus are equally in accord with the experimental facts, and Brueckner's theory is not completely excluded although it gives the worst fit to the data.

Stearns used their data to deduce values of a_1 and a_3 assuming that the theory of Deser *et al.* applied. A least squares fit gave values of $a_1 = 0.145\lambda_\pi$ and $a_3 = -0.10\lambda_\pi$ which agree well with Orear's values. It

† Account was taken of the fact that the errors on a_1 and a_3 given by Orear are not independent. We are indebted to Professor H. L. Anderson for pointing out the possible importance of this and to Dr. J. Howlett for instruction in the method of combining such errors.

does not however follow, as is evident from table 5, that the theory of Deser *et al.* gives the best fit to the data. When the errors in the least squares values of a_1 and a_3 ($\pm 0\cdot 02$ and $\pm 0\cdot 014$ respectively according to Orear 1956) are taken into account, the values of the energy shifts deduced are seen to be subject to a very large error. For example the calculated shift for oxygen is $10\cdot 4 \pm \sim 6\%$.

The present experimental data is probably accurate enough to discriminate betwen the various theories when more precise values of a_1 and a_3 become available.

§ 5. Energies of π-Mesonic L X-rays

The effect of short range forces on the energies of L transitions from light elements is very much less than in the case of the K series. Stearns and Stearns (1956 a) have estimated that an upper limit to the energy shift is given by $-\delta E/E_{L\alpha} = 2\cdot 5 \times 10^{-5} \times Z^4 \%$. The important phase shift (i.e. for the 2_p level) is δ_{33} which is positive so that the energies of the L transition would be raised in contrast to the behaviour for the K transitions. Stearns and Stearns (1956 a) found no evidence for a shift of this magnitude for $Ca(Z=20)$, and it is therefore safe to assume that the actual shift is much less than the upper limit. For Z up to about 10 the L ray energies can therefore be calculated directly from electromagnetic effects to better than $0\cdot 1\%$.

Fig. 7
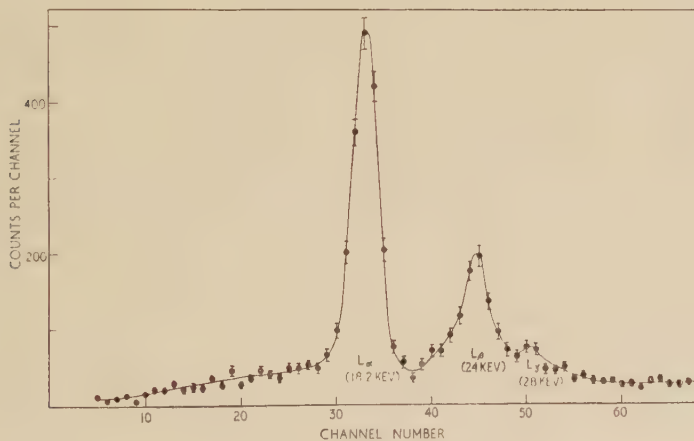
L series x-rays from carbon.

Energy measurements were made of the L_α ($3 \rightarrow 2$) lines of elements from carbon to magnesium, primarily as a check on the experimental technique which was similar to that for the K series measurements. The yield of L rays is however higher than that of the K rays and shorter runs were possible—four hours being about the maximum period.

L ray spectra from C, N, Na and Mg are shown in figs. 7–10. The $L_\beta(4 \rightarrow 2)$ and in some cases the L_γ ($5 \rightarrow 2$) groups are resolved. In the cases of sodium and magnesium the M_α ($4 \rightarrow 3$) line is also clearly seen,

Fig. 8
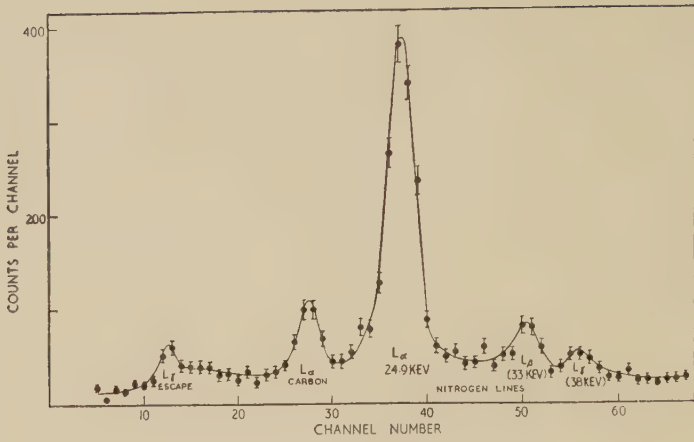
L series x-rays from nitrogen (C₂N₄H₄).

Fig. 9

L and M series x-rays from sodium.

Fig. 10

L and M series x-rays from magnesium.

Table 6 contains the measured L_α energies together with the values calculated for $m_\pi = 272 \cdot 8$ including the small correction due to vacuum polarization (Stearns and Stearns 1956 a). The finite nuclea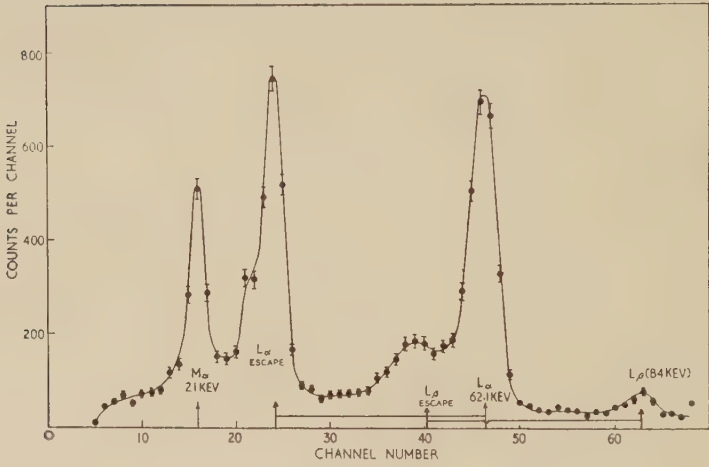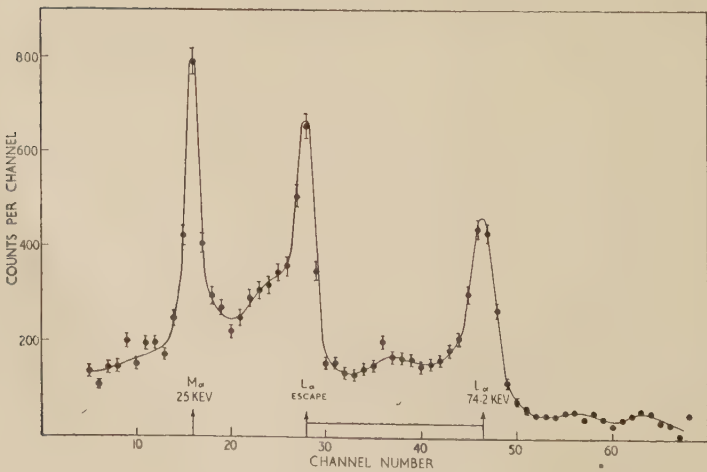r size correction is negligible. From the mean value of the measured energy an effective meson mass is deduced from the measurements for each element. The values are given in the last column of Table 6.

Table 6. Measurements of L_α energies

Element	Compound	Measured energy values of L_α line (kev)	Weighted mean energy (kev)	Calculated energy $m_\pi = 272 \cdot 8$ (kev)	Effective π-meson mass (units of m_e)
C		$18 \cdot 1_1$ $18 \cdot 1_7$ $18 \cdot 1_6$	$18 \cdot 1_5$	$18 \cdot 38$	$269 \cdot 4$
N	BN NH_4F NH_4F BN $C_2N_4H_4$	$24 \cdot 9_6$ $24 \cdot 6_8$ $24 \cdot 8_2$ $24 \cdot 9_7$ $24 \cdot 8_5$	$24 \cdot 8_5$	$25 \cdot 07$	$270 \cdot 4$
F	LiF LiF NaF NH_4F NH_4F LiF LiF LiF	$41 \cdot 6_1$ $41 \cdot 9_4$ $41 \cdot 9_3$ $41 \cdot 6_6$ $41 \cdot 6_8$ $41 \cdot 7_0$ $41 \cdot 7_2$† $41 \cdot 7_2$†	$41 \cdot 7_7$	$41 \cdot 60$	$273 \cdot 9$
Na		$61 \cdot 6_9$ $62 \cdot 1_4$ $62 \cdot 2_5$	$62 \cdot 0_8$	$62 \cdot 29$	$271 \cdot 9$
Mg		$74 \cdot 2_7$ $74 \cdot 0_8$	$74 \cdot 1_5$	$74 \cdot 18$	$272 \cdot 7$

† Measurements of the 'escape' peak.

The mean of all these values weighted by the total number of counts in the peaks divided by the instrumental width squared is $m_\pi = 272 \cdot 5 \pm 0 \cdot 8 \, m_e$ which is to be compared with the accepted value $272 \cdot 8 \pm 0 \cdot 3 \, m_e$ (Barkas, *et al.* 1956) and the limits $272 \cdot 2 \, m_e < m_\pi < 273 \cdot 6 \, m_e$ set by critical absorber measurements on π-mesonic M ray lines by Stearns, Stearns, DeBenedetti and Leipuner (1954).

The value of m_π deduced from the L ray measurements therefore agrees with the accepted value within the experimental error. It

establishes that there is no large systematic error in our technique of measuring energy. In addition there is no indication within the accuracy ($\pm 0.6\%$) of any shift in the energies of the L rays due to short range interactions up to $Z=12$.

§ 6. Measurement of the Natural Broadening of the π-Mesonic K_α Line from Beryllium

The strong interaction between π-mesons and nucleons which leads to capture from the 1s or higher levels is also expected to broaden the energy levels, especially the 1s level. Brueckner (1955), has calculated that the 1s level should have a full width at half maximum $\Gamma = 2 \times 4/3 \times Z^2/2150 . E_{K\alpha}$, which gives $\Gamma = 0.9$ kev for beryllium. The instrumental width in our proportional counter was equivalent to a full width at half maximum of 3·4 kev at this energy. However the effective instrumental width can be reduced by making use of the escape peak. Here the instrumental width is only 1·6 kev at the energy (12·5 kev) corresponding to the escape peak from the beryllium K_α line. Natural broadening of the line will be equally great for the main and escape peaks since there is a constant difference of energy (equal to that of the electronic K_α x-ray of xenon) between the two peaks. The instrumental width is therefore small enough to enable a natural broadening of the predicted amount to be detected.

It was desirable to measure the instrumental width in conditions approximating as closely as possible to those in which the beryllium K_α line was measured. Accordingly a π-mesonic L line (fluorine $L_\alpha = 41.6$ kev) of very nearly the same energy as the beryllium K line (42·15 kev) was chosen for this purpose. The expected natural broadening of this L series line is negligible and the observed width is essentially instrumental.

Beryllium and lithium fluoride sources of very nearly the same mass/cm^2 and area were used, and the proportional counter single rates were made as nearly as possible the same for the two runs. Two hour runs with beryllium alternated with one hour runs with LiF, with calibrations between each run, and the individual spectra were added at the end of a series. Hence drifts should affect the two spectra equally. In fig. 11 two spectra taken in this manner are shown. Figure 12 shows similar spectra in which only the escape peaks were measured.

The widths of these lines were measured by fitting Gaussians to the spectra using an ogive plot, on which the fractional area under a Gaussian up to any abscissa when plotted against the abscissa is a straight line. The fit is sensitive to the background assumed and several choices indicated in figs. 11 and 12 were made.

In table 7 the measured values of the standard deviations σ obtained from the ogive plots are given. In addition the standard deviations of the calibrations (41·3 kev and 11·6 kev for the main and escape peak measurements respectively), taken between the individual runs are

given. They represent the broadening due to random drifts in gain and apply equally to the Be and F measurements. The drift is in all cases negligibly small. The natural broadening of the beryllium line $\sigma_{nat.}$ is then given by $\sigma_{nat} = (\sigma_{Be}^2 - c \cdot \sigma_{F}^2)^{1/2}$ where the factor c is 1·01 for the main peak measurement and $c = 1·04$ for the escape peak measurement and takes account of the slight difference in energy of the two

Fig. 11
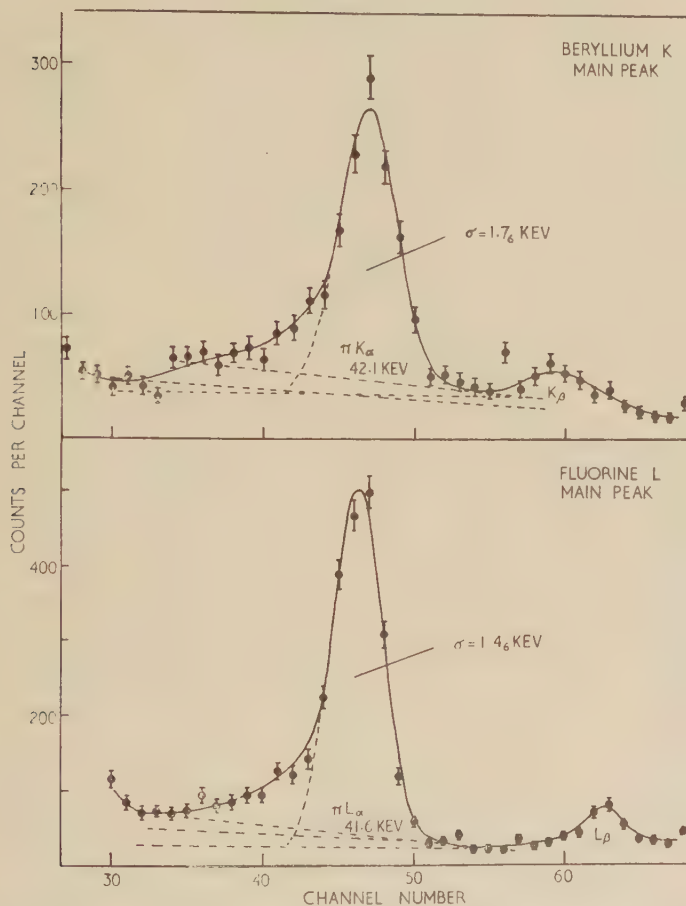
Comparison of the widths of the main peaks from B_e, $K\alpha$ and F, L_α radiations.

lines. The experimental values are given in the last column of table 7 with errors assigned by combining the largest value of the beryllium width with the smallest value of the fluorine width and *vice versa*.

The weighted mean of these values is $\sigma = 0·52 \pm 0·06$ kev or†
$\Gamma = 2·36\sigma = 1·2 \pm 0·2$ kev which is close to Brueckner's value $\Gamma = 0·9$ kev.

† In a previous letter West and Bradley (1956), Γ was wrongly equated to σ.

The experimental width corresponds to a mean life of 6×10^{-19} sec for a π-meson in the 1s state of beryllium.

The Brueckner theory, therefore, which somewhat over-estimates the energy shift, is nevertheless in agreement with experiment as far as the width of the line is concerned. A possible explanation pointed out by Eden (private communication) is that the width as calculated by Brueckner is much less sensitive to the momentum distribution of nucleons than is

Fig. 12
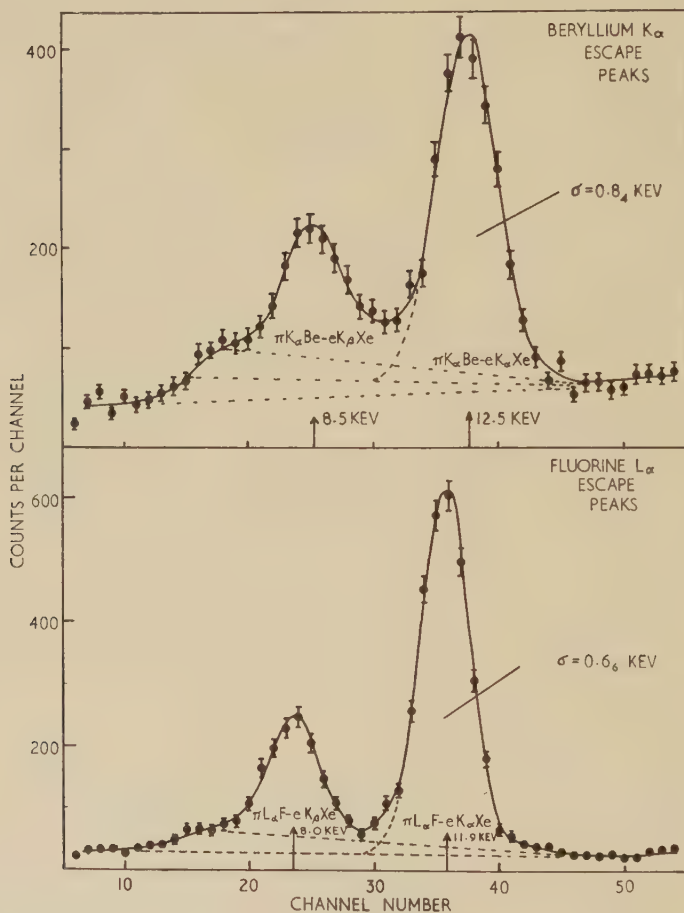
Comparison of the widths of the escape peaks from Be, K_α and F, L_α radiations.

his energy shift. No level broadening is expected from the pion, single nucleon interaction responsible for the level shifts calculated by Deser *et al.* (1954) since the charge exchange process which could give a broadening is energetically impossible in ^{9}Be.

The fact that nuclear absorption of π-mesons does occur and moreover that the resulting broadening calculated by Brueckner is in agreement

Fig. 13
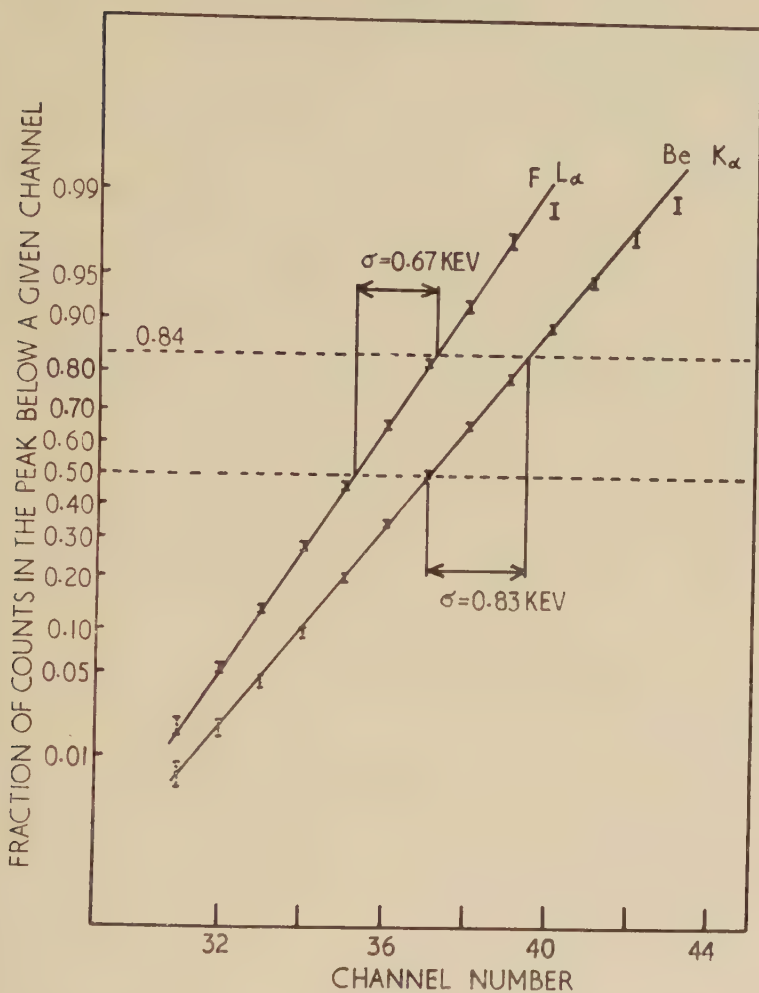
Ogive plots of the escape Peaks from fluorine L_α and beryllium K_α Radiations.

Table 7.   Natural broadening of the Be K_α line

Experimental details	σ Calibrations (kev)	σBe K (kev)	σ F L (kev)	$\sigma_{nat} = (\sigma_{Be}{}^2 - c.\sigma_F{}^2)^{1/2}$ (kev)
Main peak measurement Be, two 2 hr runs F, three 1 hr runs	0·2	$\left.\begin{array}{l}1\cdot8_6\\1\cdot7_8\\1\cdot6_3\end{array}\right\}1\cdot76$	$\left.\begin{array}{l}1\cdot4_4\\1\cdot5_0\\1\cdot4_4\end{array}\right\}1\cdot46$	$\begin{array}{l}1\cdot0+0\cdot2\\-0\cdot4\end{array}$
Escape peak measurement Be, four 2 hr runs F, three 1 hr runs	0·08	$\left.\begin{array}{l}0\cdot8_6\\0\cdot8_8\\0\cdot8_1\end{array}\right\}0\cdot85$	$\left.\begin{array}{l}0\cdot6_8\\0\cdot7_1\end{array}\right\}0\cdot69$	$0\cdot47\pm0\cdot10$
Escape peak measurement Be, four 2 hr runs F, four 1 hr runs	0·08	$\left.\begin{array}{l}0\cdot8_6\\0\cdot8_2\\0\cdot8_3\end{array}\right\}0\cdot84$	$\left.\begin{array}{l}0\cdot6_7\\0\cdot6_5\end{array}\right\}0\cdot66$	$0\cdot49\pm0\cdot07$

with experiment makes it unlikely that the theory of Deser *et al.* can adequately describe the energy shifts of the K lines. As discussed in § 4, the energy shifts themselves cannot decide between the theories at present but the existence of a level broadening is evidence that a theory of the Brueckner or Karplus type which includes the interaction leading to absorption of the π-meson is to be preferred.

§ 7. Relative Intensity Measurements

The proportional counter is not a suitable instrument for the absolute measurement of intensities of the x-rays owing to the rapid variation of efficiency with energy and the very complicated geometry. Relative efficiencies for two lines of slightly different energy can however be calculated with fair precision from the photoelectric absorption co-efficient of xenon as a function of energy. Only an approximate value of the mean track length of x-rays passing through the counter is required. It was derived from a measurement of the efficiency at 60 kev made using an ^{241}Am source of known intensity placed at the same distance from the counter as the mid point of the target. The mean track length determined in these conditions was 0·7 (counter diameter) for x-rays crossing the counter.

Table 8.   Relative Intensities

Element	Intensity ratio $K_\beta : K_\alpha + K_\beta$	Intensity ratio $L_\alpha : L_\beta : L_\gamma$
Lithium	1. 0·35 2. 0·30 mean 0·32 ± 0·03	
Beryllium	1. 0·21 2. 0·20 mean 0·20$_5$ ± 0·02	
Carbon		1. 0·75 : 0·20 : 0·05 2. 0·89 : 0·09 : 0·02 mean 0·82 ± 0·08 : 0·14 ± 0·05 : 0·03 ± 0·02
Nitrogen		1. 0·77 : 0·17 : 0·06 2. 0·83 : 0·13 : 0·04 mean 0·80 ± 0·05 : 0·15 ± 0·02 : 0·05 ± 0·01

Absorption in the target material, the anticoincidence scintillator and the aluminium wall of the counter was approximated by assuming first that the actual thickness of the scintillator and aluminium and half the thickness of the target was effective. A second calculation was made using twice these values to allow for obliquity.

Table 8 contains relative intensities of K_α (2 → 1) and K_β (3 → 1 and 4 → 1 etc.), and of L_α, L_β, L_γ lines deduced in this fashion where 1 and 2 refer to the two assumptions made in correcting for absorption.

The $K_\beta : K_\alpha + K_\beta$ ratio in beryllium is similar to the values observed in nitrogen and oxygen ($0\cdot20\pm0\cdot05$ and $0\cdot21\pm0\cdot06$, Camac *et al.* (1955)), but the ratio for lithium is definitely greater than for the heavier elements. This may be connected with the fact, observed by Stearns and Stearns (1956 b) that the yield of lithium K series x-rays is smaller than that from beryllium, which they ascribe to Auger competition.

The relative yields of the L series lines agree with the scintillation measurements of Camac, Halbert and Platt (1955).

A comparison was also made of the total K series yields of ^{6}Li and ^{7}Li. The triple coincidence rates were monitored for these runs which were interlaced with each other and the number of mesons stopping was assumed to be proportional to the number of electrons in each target, and to the number of mesons passing through counters 1, 2 and 3. A ratio

$$\frac{\text{K x-rays from } {}^6\text{Li per stopped meson}}{\text{K x-rays from } {}^7\text{Li per stopped meson}} = 0\cdot93\pm0\cdot05$$

was obtained.

References

Barkas, W. H., Birnbaum, W., and Smith, F. M., 1956, *Phys. Rev.*, **101**, 778.
Batchelor, R., Aves, R., and Skyrme, T. H. R., 1955, *Rev. sci. Instrum.*, **26**, 1037.
Brueckner, K. A., 1955, *Phys. Rev.*, **98**, 769.
Camac, M., Halbert, M. L., and Platt, J. B., 1955, *Phys. Rev.*, **99**, 905.
Camac, M., McGuire, A. D., Platt, J. B., and Schulte, H. J., 1952, *Phys. Rev.*, **88**, 134 ; 1955, *Ibid.*, **99**, 897.
Cockroft, A. L., and Curran, S. C., 1951, *Rev. sci. Instrum.*, **22**, 37.
Deser, S., Goldberger, M. L., Baumann, K., and Thirring, W., 1954, *Phys. Rev.*, **96**, 774.
Karplus, R., 1956, *Sixth Annual Conference on High Energy Physics* (University of Rochester).
Karplus, R., and Halpern, F., 1957, *New York Meeting* (American Physical Society).
McGuire, A. D., Camac, M., Halbert, M. L., and Platt, J. B., 1954, *Phys. Rev.*, **95**, 625.

OREAR, J., 1956, *Nuovo Cim.*, **4,** 856, 1956.

STEARNS, M. B., DEBENEDETTI, S., STEARNS, M., and LEIPUNER, L., 1954, *Phys. Rev.*, **93,** 1123.

STEARNS, M., and STEARNS, M. B., 1956 a, *Phys. Rev.*, **103, 1534**; 1956 b, *CERN Symposium II*, 422.

STEARNS, M. B., STEARNS, M., DEBENEDETTI, S., and LEIPUNER, L., 1954, *Phys. Rev.*, **96,** 804.

STEARNS, M., STEARNS, M. B., DEBENEDETTI, S., and LEIPUNER, L., 1954, *Phys. Rev.*, **95,** 1353; 1955, *Ibid.*, **97,** 240.

WEST, D., and BRADLEY, E. F., 1956 a, *Phil. Mag.*, **1,** 97; 1956 b, *CERN Symposium II*, 417.

WILKINSON, D. H., 1950, *Ionisation Chambers and Counters* (Cambridge : University Press).

Surface Distributions of Dislocations in Metals : II†

By C. J. Ball

Crystallographic Laboratory, Cavendish Laboratory, Cambridge, England

Abstract

It is shown that the rotation axis of a boundary containing dislocations of three systems can lie anywhere on the surface of a cone ; to each direction of the rotation axis there corresponds a single boundary plane. The theory cannot explain the experimental evidence on misorientations in zinc unless slip occurs in non-basal directions, or on planes not hitherto reported, at high temperatures. The experimental evidence for face-centred cubic metals is insufficiently precise to form a test of the theory.

§ 1. Introduction

In a previous paper (Ball and Hirsch 1955) it has been shown that Frank's equation for the dislocation content of a plane, low angle boundary (Frank 1950) can be used to determine the types of stress free boundary that can be formed with dislocations of one or two systems subject to these dislocations lying in their usual slip planes. The rotation axes of most of the boundaries observed experimentally approximate fairly closely to those of boundaries containing only two sets of dislocations, but often the discrepancy is greater than can be accounted for by experimental error. In this paper the method of analysis is extended to boundaries containing three sets of dislocations, and the theory is applied to the experimental observations. Some new observations are reported.

§ 2. Method of Analysis

Frank has shown that the resultant Burgers vector $\mathbf{d}$ of the dislocations cut by a vector $\mathbf{r}$ lying in a stress free boundary is given by

$$\mathbf{d}=(\mathbf{r} \times \mathbf{l})2 \sin \tfrac{1}{2}\alpha$$

where $\mathbf{l}$ is a unit vector parallel to the axis of rotation and α is the angle of rotation. It follows that $\mathbf{d}$ is normal to $\mathbf{r}$ and $\mathbf{l}$ for all $\mathbf{r}$. This relation can be used to determine the types of boundary that can be formed with

---

† Communicated by the Author.

any combination of dislocation systems. The most important cases involving three sets of dislocations will now be discussed.

Let the normals to the three slip planes be $\mathbf{p}_1$, $\mathbf{p}_2$, $\mathbf{p}_3$, the Burgers vectors $\mathbf{b}_1$, $\mathbf{b}_2$, $\mathbf{b}_3$, the dislocations parallel to vectors $\mathbf{r}_1$, $\mathbf{r}_2$, $\mathbf{r}_3$ and let there be n_1, n_2, n_3 dislocations of each type per unit length taken normal to that type.

2.1. *Two Slip Systems have the same Slip Plane*

Let the identical planes be $\mathbf{p}_1$, $\mathbf{p}_2$. If we take $\mathbf{r}$ parallel to $\mathbf{r}_1$, it will cut dislocations of the third set only, so $\mathbf{r}_1$ must be normal to $\mathbf{b}_3$. By taking $\mathbf{r}$ parallel to $\mathbf{r}_3$, we see that $\mathbf{l}$ must also be normal to the vector $(n_1\mathbf{b}_1+n_2\mathbf{b}_2)$. As this vector can lie anywhere in the plane containing $\mathbf{b}_1$ and $\mathbf{b}_2$, $\mathbf{l}$ can lie anywhere in the plane normal to $\mathbf{b}_3$.

Corresponding to each direction of the rotation axis there is only one possible boundary plane : for $\mathbf{r}_1$ must be normal to $\mathbf{b}_3$ and lie in $\mathbf{p}_1$, and $\mathbf{r}_3$ must be normal to $(n_1\mathbf{b}_1+n_2\mathbf{b}_2)$ and lie in $\mathbf{p}_3$. The boundary plane is the plane containing $\mathbf{r}_1$ and $\mathbf{r}_3$.

If the dislocations are all parallel, they must be parallel to the intersection of the planes $\mathbf{p}_1$, $\mathbf{p}_3$. $\mathbf{l}$ will also be parallel to this direction. The boundary plane must be normal to the vector $(n_1\mathbf{b}_1+n_2\mathbf{b}_2+n_3\mathbf{b}_3)$. If $\mathbf{b}_1$, $\mathbf{b}_2$, $\mathbf{b}_3$ are coplanar, the boundary can only form on one plane. Otherwise, any boundary plane is possible that is parallel to $\mathbf{r}_3$.

2.2. *Two Slip Systems have the same Burgers Vector*

Let the identical Burgers vector be $\mathbf{b}_1$, $\mathbf{b}_2$. Then $\mathbf{l}$ must be normal to the plane containing $\mathbf{b}_1$ and $\mathbf{b}_3$, as $\mathbf{d}$ will always lie in this plane.

$\mathbf{r}_3$ is determined as it must be normal to $\mathbf{b}_1$ and lie in plane $\mathbf{p}_3$. The boundary plane must contain $\mathbf{r}_3$, but otherwise it is arbitrary as n_1 and n_2 are independent.

2.3. *The Three Slip Systems are Unrelated*

It will be convenient to define unit vectors $\mathbf{d}_1$, $\mathbf{d}_2$ and $\mathbf{d}_3$ by the relations

$$\mathbf{d}_1 \cdot \mathbf{b}_2 \times \mathbf{b}_3 = 0$$
$$\mathbf{d}_1 = 0$$

with similar equations for $\mathbf{d}_2$ and $\mathbf{d}_3$ obtained by rotating subscripts.

If now $\mathbf{r}$ is taken parallel to $\mathbf{r}_1$, $\mathbf{d}$ will be parallel to $\mathbf{d}_1$, as it must lie in the plane containing $\mathbf{b}_2$ and $\mathbf{b}_3$ and be normal to $\mathbf{l}$.

Hence $\mathbf{r}_1$ can be determined, as it must be normal to $\mathbf{d}_1$ and lie in the plane $\mathbf{p}_1$. Similarly, we can determine $\mathbf{r}_2$ and $\mathbf{r}_3$. If $\mathbf{r}_1$, $\mathbf{r}_2$ and $\mathbf{r}_3$ so obtained are coplanar, the boundary will be satisfactory.

In practice, $\mathbf{r}_1$, $\mathbf{r}_2$ and $\mathbf{r}_3$ are obtained in terms of the crystallographic indices of the rotation axis (H, K, L). The indices of the plane containing $\mathbf{r}_1$ and $\mathbf{r}_2$ are next found, again in terms of H, K, L, and the condition

that $\mathbf{r}_3$ should lie in this plane gives an equation relating H, K and L. Solving this equation gives the locus of the rotation axis. The method fails for certain directions of the rotation axis, which must be checked.

It is not immediately obvious that the dislocation ratios required by the above construction will be mutually compatible. That they will be can be shown thus. Read (1953) has shown that any boundary can be composed of any three sets of dislocations with non-coplanar Burgers vectors, the direction of the dislocations being arbitrary. A boundary obtained by the above construction will require its dislocations to lie in their usual slip planes, for, taking $\mathbf{r}$ parallel to the intersection of the boundary plane and plane $\mathbf{p}_1$, $\mathbf{d}$ will be parallel to $\mathbf{d}_1$, and so $\mathbf{r}$ must be parallel to $\mathbf{r}_1$ as it cuts no dislocations of set 1, i.e. $\mathbf{r}_1$ lies in the plane $\mathbf{p}_1$. Similarly $\mathbf{r}_2$ and $\mathbf{r}_3$ must lie in the planes $\mathbf{p}_2$, $\mathbf{p}_3$ respectively.

§ 3. Results

3.1. *Hexagonal and Body-Centred Cubic Systems*

The only slip directions for hexagonal metals reported in the literature are of the form $\langle 11\bar{2}0 \rangle$ lying in the basal plane. The most common slip plane is (0001) but slip has also been reported on prismatic and pyramidal planes, particularly at high temperatures. The only boundaries that can be formed with dislocations of these systems are (*a*) twist boundaries with rotation axis [0001] or (*b*) tilt boundaries in which all the dislocations are parallel. The rotation axis for such a boundary is parallel to the intersection of the slip planes, while the boundary plane contains this direction and is normal to the basal plane.

In body-centred cubic metals slip takes place in the direction [111] on a variety of planes. The number of possible combinations of slip systems is very large, and they will not be considered in detail. If the slip planes are suitably chosen, practically any boundary can be formed by slip alone.

3.2. *Face-Centred Cubic System*

In face centred cubic metals slip takes place on {111} planes in $\langle 110 \rangle$ directions. We will now enumerate the distinct combinations of slip systems, using Thompson's notation (Thompson 1953).

There are five distinct combinations of vectors

1. Three vectors equally inclined to one another.

2. Two vectors at right angles and a third.

3. Two vectors identical and one at 60° to them.

4. Two vectors identical and one at 90° to them.

5. Three vectors in a plane.

Combinations of vector and plane are

		a	b	c	d
Case 1	A B	γ	γ		
	A C	δ	β		
	A D	β	β		
Case 2	A B	δ	δ	γ	
	B C	α	α	α	
	A D	β	γ	γ	
Case 3	A B	γ	γ		
	A B	δ	δ		
	A D	β	γ		
Case 4	A B	γ			
	A B	δ			
	C D	α			
Case 5	A B	δ	δ	δ	γ
	B C	δ	δ	α	α
	C A	δ	β	β	β

Most of these combinations are of the special types considered in § 2.2 and § 2.3.

  Possible rotation axes are

  a In (110)   Cases 1b, 2c

  b   [111]   Cases 3a, 3b, 5c–d

  c   [100]   Case 4

  d In (111)   Case 5a

  d   [110]   Cases 1b, 2c, 3b, 5b (pure tilt boundaries).

  Cases 1a, 2a, and 2b are of the type considered in § 2.4. The loci of the rotation axis for these cases are shown in figs. 1, 2 and 3, respectively. The equations to be satisfied by H, K, L, are
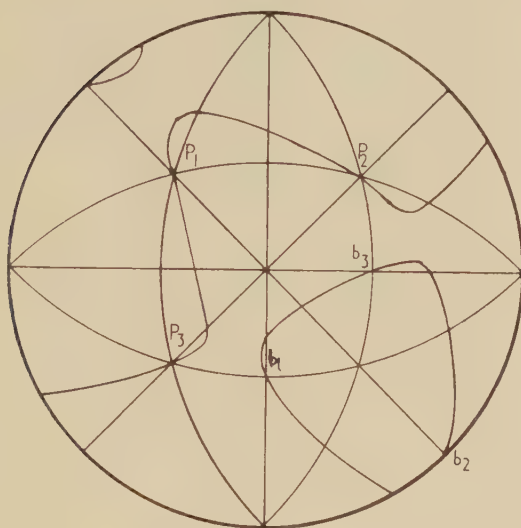
  1a. $H^3+K^3+L^3-2H^2L-2K^2L-2L^2H-HKL=0$

  2a. $3L^3+H^2(K+L)-K^2(L+H)+2L^2(2H+K)+3HKL=0$

  2b. $K^3-2L^3+H^2(K+L)+2K^2(H+2L)+L^2(H+K)+3HKL=0$.
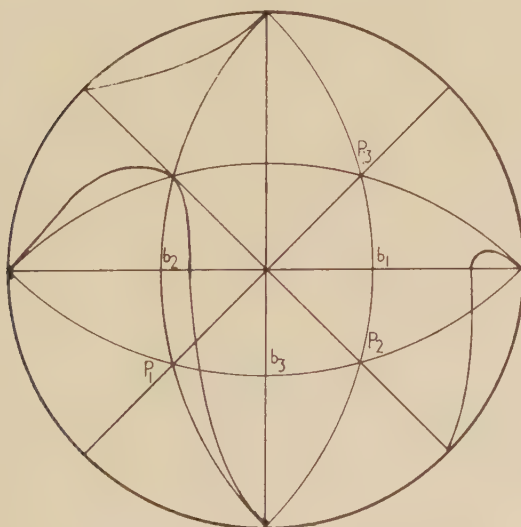
(The orientation of Thompson's tetrahedron adopted was $\alpha=(111)$, $\beta=(\bar{1}1\bar{1})$, $\gamma=(\bar{1}\bar{1}1)$, $\delta=(1\bar{1}\bar{1})$).

Fig. 1

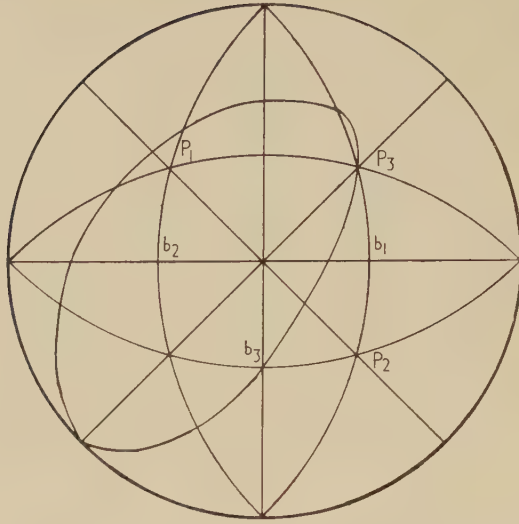Locus of rotation axis for case 1a of the face-centred cubic system.

Fig. 2

Locus of rotation axis for case 2a of the face-centred cubic system.

To each direction of the rotation axis, there corresponds a single boundary plane. This can be determined graphically, as in fig. 4. or by substituting values of H, K, L into the indices of the plane containing $\mathbf{r}_1$ and $\mathbf{r}_2$.

Fig. 3

Locus of rotation axis for case 2b of the face-centred cubic system.

Fig. 4
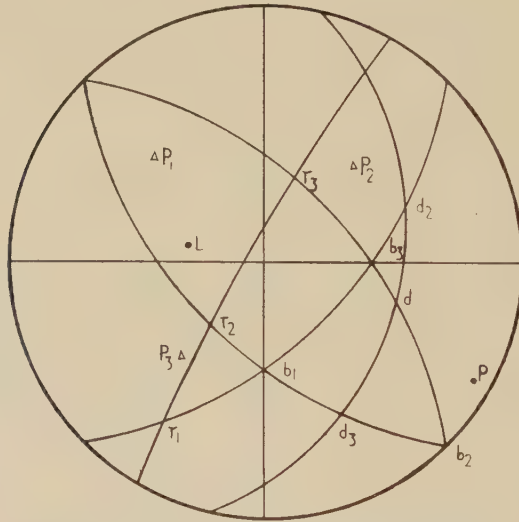
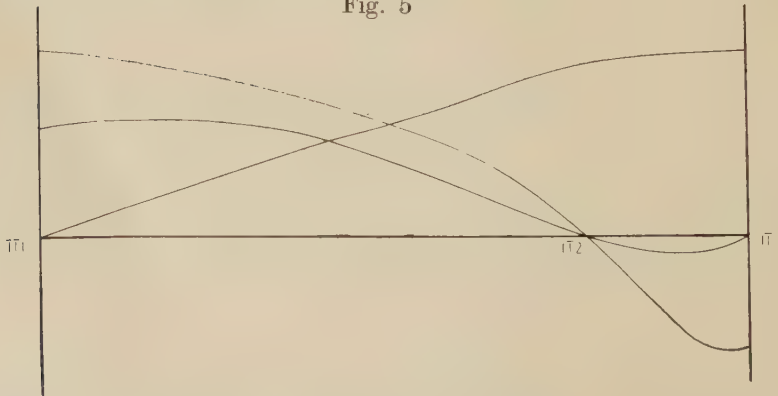Graphical determination of boundary plane.

Fig. 5

Variation of densities of dislocations along the locus of the rotation axes
from [1$\bar{1}$1] to [1$\bar{1}$1] for a boundary of type 1a.

The numbers of dislocations of each type in the boundary can be determined analytically (Read 1953) or graphically. Figure 5 shows the way in which the densities of the three systems of dislocations in a boundary of type 1a vary as the rotation axis travels the locus from [111] to [1$\bar{1}$1]. It will be seen that boundaries containing only one or two sets of dislocations are included as special cases.

Fig. 6
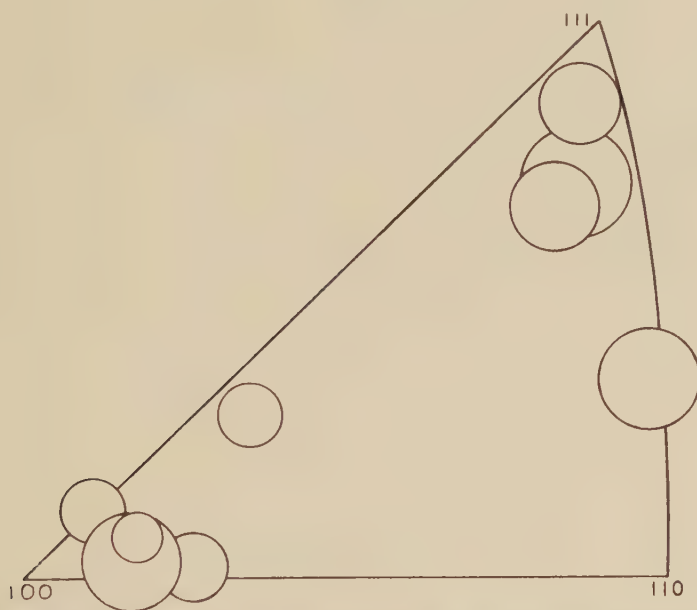
Observed rotation axes in polycrystalline aluminium deformed at temperatures in the range 0–300°c.

§ 4. DISCUSSION

4.1. *Hexagonal and Body-Centred Cubic Systems*

There is very little experimental evidence on the rotation axes of low angle boundaries formed by deformation. The most extensive observations are those of Cahn *et al.* (1954) on zinc. In polycrystalline zinc made to creep at 250°c most of the rotation axes observed were within 10° of the basal plane and it has been suggested (Ball and Hirsch 1955) that this may be because the dislocations are heavily jogged. However, in specimens made to creep at 350°c the rotation axes observed were distributed fairly uniformly throughout the unit triangle. These boundaries could not have been formed by slip alone on any combination of known slip systems. They could have been formed with the help of climb, but the amount of climb required is very large and it seems more reasonable to suppose that at these elevated temperatures slip

is occurring in some direction that does not lie in the basal plane, or on some hitherto unreported planes.

All observed rotation axes in body-centred cubic metals can be explained in terms of boundaries containing only one or two sets of dislocations.

4.2. *Face-Centred Cubic System*

The rotation axes shown in fig. 6 have been observed in polycrystalline aluminium deformed at temperatures in the range 0–300°c. Details of these experiments will be given later.

It will be seen that most of the rotation axes correspond fairly closely with those of boundaries that could be formed with dislocations of only two systems ([100], [111], in (110), in (111)) but that in some cases the discrepancy is greater than can be accounted for by experimental error. It is thought that most of these boundaries contain a small admixture of dislocations of a third system. Boundaries of types 1a, 2a, 2b (§ 3.2) give such complete coverage of the unit triangle that, with the precision of the present experimental results, any rotation axis could be explained in terms of one at least of these types of boundary. However, as to each direction of the rotation axis there corresponds only a single boundary plane, a test of the theory could be made if observations were possible of both rotation axes and boundary planes. This is being attempted.

References

Ball, C. J., and Hirsch, P. B., 1955, *Phil. Mag.*, **46**, 1343.
Cahn, R. W., Bear, I. J., and Bell, R. L., 1954, *J. Inst. Met.*, **82**, 481.
Frank, F. C., 1950, *Carnegie Inst. of Tech. Symposium on the Plastic Deformation of Crystalline Solids* (Pittsburgh Report) p. 150, Office of Naval Research (NAVEXOS–P–834).
Read, W. T., 1953, *Dislocations in Crystals* (New York : McGraw-Hill).
Thompson, N., 1953, *Proc. phys. Soc. Lond.*, B, **66**, 481.

Impurity–Vacancy Interaction in a Metal†

By L. C. R. Alfred and N. H. March
Department of Physics, The University, Sheffield

Abstract

Using a generalization of the model first introduced by Mott for dealing with impurities in monovalent metals, the interaction between an impurity and a vacancy has been studied. Detailed computations have been carried out for the case of copper, with a divalent impurity and a vacancy at a separation of 5 atomic units. The interaction is attractive, the associated energy being calculated as 0·08(4) ev when exchange and correlation energies are neglected. Inclusion of these effects reduces the interaction energy to 0·03(3) ev. A previous calculation by Lazarus leads to a value of 0·045 ev for the case considered here, while a modification of the Lazarus expression proposed by the present writers gives 0·035 ev. Thus the present work tends to substantiate further the Lazarus theory of solute diffusion in metals.

§ 1. Introduction

Much experimental information has accumulated over the past few years concerning the diffusion of impurity atoms in metals. Particularly interesting from the point of view of the present work is the finding that the activation energy for diffusion of cadmium, indium, tin and antimony in silver decreases as the valence difference between solute and solvent atoms increases (Sonder *et al.* 1954, Tomizuka and Slifkin 1954). Later work by Tomizuka and Sonder (1956) on self-diffusion in silver also contains relevant results and should therefore be mentioned here.

An important step towards an understanding of the salient features of these experimental results was taken by Lazarus (1954 ; see also Blatt 1955, Alfred and March 1956) who proposed an explanation based on the screening of a solute atom in a metal. Fundamental to the Lazarus theory is the evaluation of the interaction energy between the screened solute atom and a vacancy, and a simple electrostatic argument was used to compute this. However, as Lazarus pointed out elsewhere (Lazarus 1955), such a procedure appears to neglect any changes in kinetic energy and also to neglect interaction between the screens of the solute ion and the vacancy (see, however, § 3), as well as refinements

† Communicated by the Authors.

such as exchange and correlation effects. In spite of these and other approximations which it was necessary to make, Lazarus' theory has had a good deal of success. In addition to correctly explaining the variation of activation energy for impurity diffusion with valence difference referred to earlier, the theory also predicts a correlation between the frequency factor D_0 and the activation energy H in the diffusion equation

$$D=D_0 \exp\left(-H/RT\right) \qquad . \quad . \quad . \quad . \quad . \quad (1)$$

where D is the measured diffusion coefficient, R is the gas constant and T is the absolute temperature. Such a correlation is indeed evident from the experimental results and for diffusion in silver reasonable quantitative agreement between theory and experiment is found. Even for diffusion in nickel, to which the present theory can hardly be quantitatively applicable, such a correlation is again found and the agreement between theory and experiment is better than order of magnitude (Swalin 1956 ; see also March 1957, where a short review of this work can be found).

In view of these successes, it seemed a matter of some importance to attempt to put the theory on a sounder basis by making a more careful calculation of the interaction between a solute atom and a vacancy in a metal. For convenience later, we note first of all that for the interaction energy ΔE between an impurity having $Z+1$ electrons outside a closed shell and a vacancy in a monovalent metal, with Fermi energy E_m, Lazarus takes

$$\Delta E=-\frac{Z}{r_0}\exp\left(-qr_0\right); \qquad q^2=\frac{2^{5/2}}{\pi}E_m{}^{1/2},\dagger \quad . \quad . \quad . \quad (2)$$

r_0 being the impurity–vacancy separation. This is obtained by calculating the screened field of the impurity from the linearized Thomas–Fermi equation (see, for example, the review by Friedel 1954). Blatt (1955) attempted to improve the treatment by regarding the screening constant q as a parameter to be determined by the requirement that the total screening charge should be correctly given, following an earlier proposal made by Friedel (1954). Unfortunately, much of the agreement between theory and experiment then disappeared, the variation of the activation energy H with Z being much too small. However, the present writers (Alfred and March 1956) subsequently showed that, if the exact solutions of the Thomas–Fermi equation for an impurity are used (Alfred and March 1955 ; see also Fujiwara 1955, who independently made some similar calculations) instead of Blatt's fields, then the interaction energy may be written

$$-\frac{Z}{r_0}\alpha \exp\left(-qr_0\right) \qquad . \quad . \quad . \quad . \quad . \quad . \quad (3)$$

where α varies with Z, but is of the order of unity : for silver with $Z=1$ for example it was found that $\alpha=0.75$. Using these results, the agreement

---

† In (2) and all subsequent equations, atomic units are used,

between theory and experiment was largely restored although, as the present writers pointed out, the formula of Lazarus is probably preferable on the grounds of internal consistency.

From the above discussion, it is clear that ideally we should like to know the interaction energy as a function of impurity-vacancy separation around the nearest-neighbour distance in a metal, but the calculations turn out to be formidable and we have been obliged to restrict ourselves to the more modest programme of obtaining the interaction energy for one separation, which we have taken conveniently as 5 atomic units. This is close to the nearest-neighbour distance in copper (actually 4·8 atomic units) which is the metal we consider in our computations.

In addition to the work referred to above, other attempts have been made previously to calculate the interaction energy between imperfections in metals. For example, we might mention the work of Bartlett and Dienes (1953) in which the association energy of two vacancies in copper was estimated to lie between 0·2 and 0·6 ev. More recently Seeger and Bross (1956) have made a much more detailed investigation of this problem and find a value around 0·3 ev.

§ 2. Model for Present Calculation

We shall now outline briefly the model adopted for the present calculation. We shall deal with the case when the solvent is a monovalent metal, and shall describe the conduction electrons in the unperturbed metal by the free electron model, neglecting exchange and correlation. However, we shall eventually consider the effect of these energy terms by a less accurate, but probably adequate, method. Following Mott (1936) we represent an impurity with $(Z-1)$ electrons outside a closed shell as a point singularity carrying charge Z. As Mott showed, and as is essentially embodied in the statement of eqn. (2), a self-consistent field calculation then leads to the result that the conduction electrons of the metal adjust themselves to screen out the field of the charge Z in a distance of the order of 1 A. For the vacancy we shall adopt a model which appears to have been first suggested by Dexter (1952) : namely we shall treat the vacancy as an impurity of zero valency. Thus for the monovalent metal we are considering here, the vacancy is represented as a point singularity carrying a single negative charge.

To obtain a first approximation to the solution of the present problem, we need the exact numerical solutions for a single impurity and a single vacancy in an infinite metal. As we have already remarked, the case of an isolated impurity has been treated by means of the Thomas-Fermi approximation, first used in this connection by Mott, and a number of exact numerical solutions are available for copper and silver (Alfred and March 1955, Fujiwara 1955). Unfortunately the exact numerical solutions referred to above are all for the case of positive Z. For negative Z, the present writers (Alfred and March 1956) have given a very simple

analytical argument by means of which solutions of fair accuracy can be obtained in this case and this can be made the basis for the calculations of the exact numerical solution (see § 4). Thus the potentials round an isolated impurity and an isolated vacancy, along with the corresponding electronic charge distributions, were known at the outset.

The major problem, therefore, consists in the redetermination of the distribution of conduction electrons and the modified self-consistent field when the impurity (we shall deal specifically with the case of a divalent impurity, say zinc, for the purpose of the numerical calculations, although the method adopted is obviously generally applicable for any valency) and the vacancy are separated by a distance of 5 atomic units. This is a problem which from a mathematical point of view at least is not entirely dissimilar to that of determining the distribution of electrons in a hetero-nuclear diatomic molecule, and we were encouraged to attempt the numerical solution of the present problem as a treatment of the iodine chloride molecule had previously been carried through successfully using the relaxation method (Glazer and Reiss 1953). We have, therefore, made use of this technique in our work, even though an additional complication, that of a variable boundary round the vacancy (see § 5), was present in our problem.

§ 3. Impurity–Vacancy Interaction Energy in First-Order Treatment

In view of the success of the simple formula (2), it is of interest at this stage to consider a more detailed calculation of the interaction energy between an impurity and a vacancy using the model outlined above, but employing the Thomas Fermi method only in the linearization or first-order approximation (Mott 1936 ; see also Friedel 1954). In this case, heavy numerical computations are avoided and some insight into the main features of the problem can be obtained. On the other hand, there appear to be a number of objections to the first-order method, and we feel therefore that the quantitative predictions must be viewed with reserve. Dr. J. Friedel first brought most of the essential results obtained in this section to our notice, although we believe the detailed argument given below to be new.

We take as the basic equation of the first-order treatment

$$\nabla^2 V_p = -4\pi(n-n_0)=q^2 V_p \quad . \quad . \quad . \quad . \quad . \quad (4)$$

where V_p is the perturbing potential energy, $n(\mathbf{r})$ is the electron density in the perturbed metal and n_0 is the unperturbed density. We now seek a variation principle which will yield the relation (4) between density and potential. The form of this is suggested by the following argument. In the full Thomas Fermi approximation the change in kinetic energy of the electrons is given by

$$\frac{3}{10}(3\pi^2)^{2/3}\int(n^{5/3}-n_0^{5/3})\,d\tau. \quad . \quad , \quad . \quad , \quad . \quad . \quad (5)$$

Assuming $\Delta = n - n_0$ is small, (5) may be written

$$E_m \int \Delta \, d\tau + \frac{2\pi}{q^2} \int \Delta^2 \, d\tau \qquad . \quad . \quad . \quad . \quad . \quad . \quad (6)$$

with neglect of higher terms. Adding the potential energy change to (6) and requiring that the resulting expression is stationary with respect to variations in Δ then yields exactly the relation (4) between density and potential. Thus, we adopt (6) as the kinetic energy change consistent with the linearized scheme given by eqn. (4).

It is now a relatively easy matter to calculate the interaction energy between two impurities in a Fermi gas. Suppose, to be general, the impurities are represented by point charges Z and Z' in this model, the separation being r_0. If V_p is the perturbing potential due to Z alone and $V_p{'}$ that due to Z', then from (4) it follows that the potential in the case of two impurities at a finite separation is just the superposition potential $V_p + V_p{'}$.

We must now compute the changes in potential and kinetic energies when we bring the impurities together, and we may write down the following contributions :

(i) The interaction energy between the charge Z of one impurity and the perturbation $V_p{'}$ due to the other.

(ii) The interaction energy between the charge cloud $(-q^2/4\pi)V_p$ round the impurity Z and the perturbation $V_p{'}$ due to the other.

(iii) The change in kinetic energy.

These three terms are evidently given by

$$\left. \begin{array}{l} \text{(i)} \quad \dfrac{ZZ' \exp(-qr_0)}{r_0} \\[3mm] \text{(ii)} \quad -\dfrac{q^2}{4\pi} \displaystyle\int V_p V_p{'} \, d\tau \\[3mm] \text{(iii)} \quad \dfrac{2\pi}{q^2} \left[\dfrac{q^4}{16\pi^2} \left\{ \displaystyle\int (V_p + V_p{'})^2 \, d\tau - \int V_p{}^2 \, d\tau - \int V_p{'}^2 \, d\tau \right\} \right] \\[3mm] \qquad = \dfrac{q^2}{4\pi} \displaystyle\int V_p V_p{'} \, d\tau. \end{array} \right\} \quad . \quad . \quad (7)$$

Thus the contribution (ii) is just cancelled by the change in kinetic energy (iii), and we are left with the formula of Lazarus

$$\Delta E = \frac{ZZ' \exp(-qr_0)}{r_0}. \qquad . \quad . \quad . \quad . \quad . \quad (8)$$

Unfortunately, however, if an attempt is made to include exchange along the lines of the argument given above, it turns out that the formula (8) is drastically changed. Nevertheless, as we shall see later, the simple arguments given here lead to results which have a number of features in common with those we find from our detailed computations.

§ 4. Potential and Distribution of Electrons Round a Vacancy

We shall now attempt to use the full Thomas–Fermi method, avoiding altogether the first-order approximation used above, and as a necessary preliminary to the main problem we shall discuss in this section the results we have obtained for the case of an isolated vacancy. We wish to solve the equation

$$-\nabla^2 V_p = \frac{2^{7/2}}{3\pi} [(E_m - V_p)^{3/2} - E_m^{3/2}] \quad . \quad . \quad . \quad . \quad (9)$$

for the self-consistent potential energy V_p. We note first of all that near the negative point charge, V_p is large and positive and inside a sphere of a certain radius r_c, will exceed the Fermi energy E_m. It then follows that, in the Thomas–Fermi approximation, no electrons are allowed inside this sphere, the region being one of negative kinetic energy. The radius r_c is determined by the condition

$$V_p(r_c) = E_m \quad . \quad . \quad . \quad . \quad . \quad . \quad . \quad (10)$$

and inside the sphere the appropriate equation to be solved is

$$\nabla^2 V_p = \frac{2^{7/2}}{3\pi} E_m^{3/2}. \quad . \quad . \quad . \quad . \quad . \quad (11)$$

The boundary conditions subject to which we must solve eqns. (9) and (11) are evidently

$$\left. \begin{array}{l} V_p \to \dfrac{1}{r} \quad \text{as} \quad r \to 0 \\[2mm] V_p \to 0 \quad \text{as} \quad r \to \infty \\[2mm] V_p \text{ and } \dfrac{dV_p}{dr} \text{ continuous at } r = r_c \end{array} \right\} . \quad . \quad . \quad . \quad (12)$$

Equation (11) can be solved immediately in this case and we have

$$V_p = \frac{1}{r} - \beta + \frac{2^{5/2}}{9\pi} E_m^{3/2} r^2 ; \qquad r < r_c \quad . \quad . \quad . \quad (13)$$

where β is a constant to be determined. On the other hand, eqn. (9) has to be solved numerically. We found a step-by-step numerical method convenient, trial and error being necessary to determine the correct value of r_c but fortunately the approximate solution considered previously (Alfred and March 1956) is a very useful starting point. We show the exact solution thus obtained in curve 1 of fig. 1 together with the approximate solution given earlier by the writers (curve 2) and the result obtained by a naive application of the first-order approximation ($V_p = 1/r \exp(-qr)$: see curve 3). Also shown in curve 4 of fig. 1 is the exact Thomas–Fermi perturbing potential for $Z = 1$, while in fig. 2 the electron densities round an isolated impurity and an isolated vacancy are shown.

§ 5. Self-Consistent Field Round Impurity–Vacancy System

We must this time solve the basic equations for the potential energy V_p assuming symmetry only about the axis joining the impurity and the

vacancy. As in the isolated vacancy case, we shall have a surface S surrounding the vacancy inside which there are no electrons, although we must now expect that it will be somewhat distorted from a sphere. Inside this surface we must solve eqn. (11) whereas outside we must deal with eqn. (9). The boundary conditions which the potential must now satisfy are

$$
\left.
\begin{aligned}
V_p &\to -\frac{1}{r_1} & \text{as} \quad r_1 &\to 0 \\
V_p &\to \frac{1}{r_2} & \text{as} \quad r_2 &\to 0 \\
V_p &\to 0 & \text{as} \quad r_1 \to r_2 &\to \infty
\end{aligned}
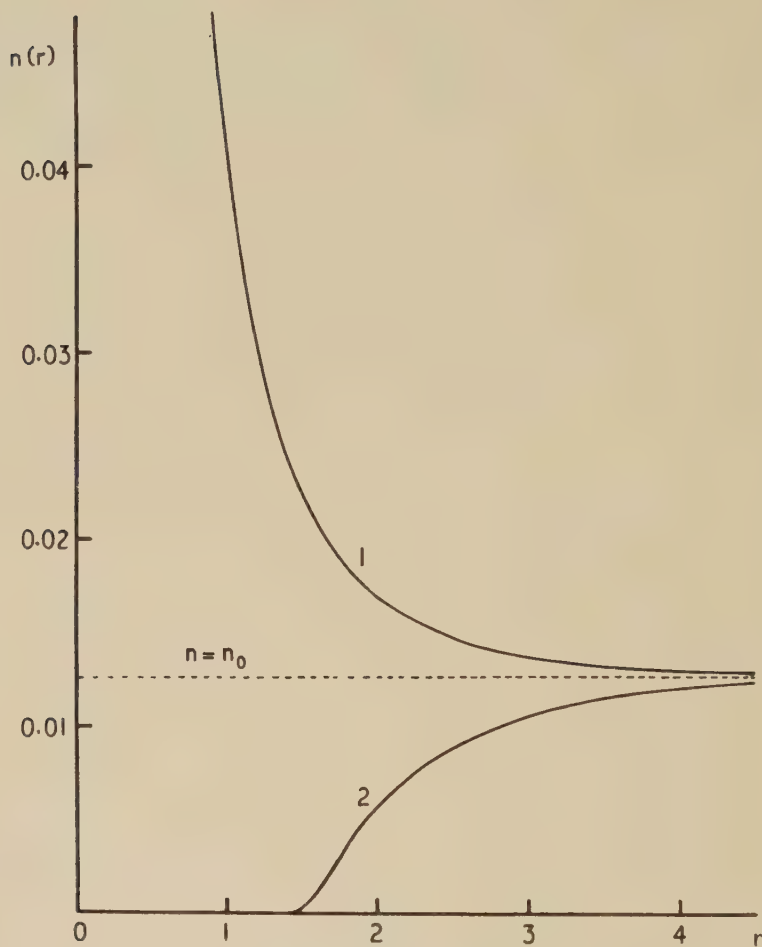\right\} \qquad \cdots \cdots \quad (14)
$$

Fig. 1
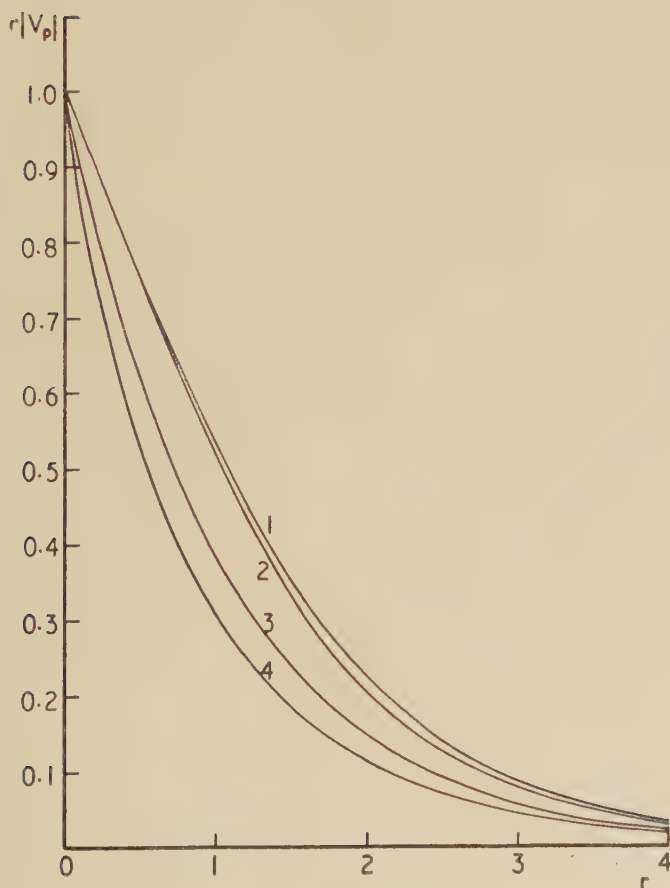
Perturbing potentials

1. rV_p for vacancy—exact numerical solution.
2. rV_p for vacancy—approximate solution.
3. $rV_p = \exp(-qr)$.
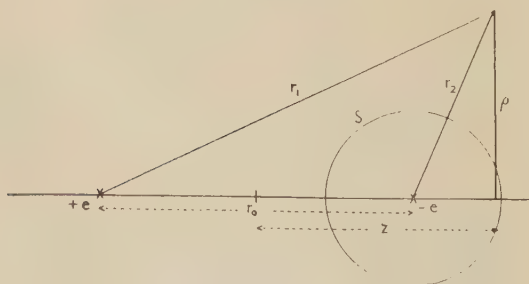4. $r\,|V_p|$ for impurity $(Z=1)$—exact numerical solution.

Fig. 2

Electron densities round isolated imperfections.
1. Impurity ($Z=1$).
2. Vacancy.

Fig. 3

Notation for impurity–vacancy case.

together with the conditions that V_p and its first derivatives are continuous across S. The notation used is shown in fig. 3.

As we have remarked earlier, we now assume for the purposes of the computations that the solvent metal is copper, that the impurity is divalent, and that the separation is 5 atomic units, or the approximate distance between nearest-neighbours in the lattice.

We begin the solution for the perturbing potential V_p corresponding to the impurity–vacancy case by removing the singularities at the impurity and the vacancy. This can be done by substituting

$$V_p = V_{pi} + V_{pv} - \delta \quad \ldots \ldots \ldots \quad (15)$$

where V_{pi} is the perturbing potential energy due to an isolated impurity, V_{pv} that due to an isolated vacancy, and δ is the change from the super-position potential energy. We may then write in the region outside the surface S

$$-[\nabla^2 V_{pi} + \nabla^2 V_{pv} - \nabla^2 \delta] = \frac{2^{7/2}}{3\pi} [(E_m - V_{pi} - V_{pv} + \delta)^{3/2} - E_m^{3/2}] \quad (16)$$

where $\nabla^2 V_{pi}$ and $\nabla^2 V_{pv}$ are known numerically from the previous work. In the region inside S we have

$$[\nabla^2 V_{pi} + \nabla^2 V_{pv} - \nabla^2 \delta] = \frac{2^{7/2}}{3\pi} E_m^{3/2} \quad \ldots \ldots \quad (17)$$

and we must solve these equations subject to the boundary conditions that δ is finite at the impurity and the vacancy, tends to zero at infinity, and is continuous together with first derivatives on the surface S.

As the potential has axial symmetry, the problem reduces to a two-dimensional relaxation solution. (For detailed discussion of two-dimensional relaxation methods, reference can be made to Southwell (1946) and Allen (1954).) Taking cylindrical polar coordinates with the impurity and vacancy on the z-axis and the origin halfway between (see fig. 3), the finite difference equations can be easily set up. The fact that the boundary is at infinity presents no real difficulty as δ falls off quickly and may be put equal to zero to sufficient accuracy on a finite surface. Because of symmetry, we are only concerned in the relaxation solution with the half of the (ρ, z) plane on either side of the z-axis, the intersection of the finite surface with the (ρ, z) plane is then only part of the boundary; the z-axis, which is the axis of symmetry, making up the other part. The complicating feature in the relaxation process is that we have a variable boundary S separating regions in which two different differential equations must be solved. The unknown boundary must again be found by trial and error, the boundary being adjusted at each stage of the calculation, so that eventually the function δ is contin-uous with its first derivatives across S and the perturbing potential energy V_p on the boundary is equal to the Fermi energy E_m. In practice, the condition $(V_p)_S = E_m$ is used first to obtain a solution, then this solution is checked by the condition of continuity which is applied by considering derivatives along the mesh lines at the points where they cut the bound-ary S. Fortunately, however, the change in the boundary when the

impurity and vacancy are brought together is rather small in the present case.

§ 6. Interaction Energy Between Impurity and Vacancy

The interaction energy between the impurity and the vacancy in the metal is obtained by computing the difference between the energy of the impurity–vacancy pair separated by the assumed distance of 5 atomic units and the energy when they are an infinite distance apart. We shall consider separately the following contributions to the energy : (i) kinetic energy ; (ii) potential energy ; (iii) exchange energy ; (iv) correlation energy.

It is certainly true that the method we have used to compute the potential neglects exchange and correlation effects. Thus the calculation neglecting exchange and correlation energies is more internally consistent. However, due to the variation principle of the Thomas–Fermi approximation we should be able to calculate the energy including exchange to good accuracy by using the unmodified density to calculate the exchange energy. This is the procedure we shall adopt here, and we shall compute the correlation energy by a similar method. This latter term, in fact, turns out to be relatively unimportant, but the exchange term is by no means so.

The following expressions result for the changes in the various energy terms :

(i) Kinetic energy change :

$$\Delta T = \frac{3}{10}(3\pi^2)^{2/3}\int [n^{5/3}+n_0{}^{5/3}-n_i{}^{5/3}-n_v{}^{5/3}]\,d\tau \quad . \quad . \quad (18)$$

where n, n_i and n_v are the electron densities corresponding to the impurity–vacancy, isolated impurity and isolated vacancy cases respectively.

(ii) Potential energy change :

$$\Delta V = -\frac{1}{2}\int \frac{1}{r_1}[n-n_i]\,d\tau + \frac{1}{2}\int \frac{1}{r_2}[n-n_v]\,d\tau$$
$$+ \frac{1}{2}\int [V_p(n-n_0)-V_{pi}(n_i-n_0)-V_{pv}(n_v-n_0)]\,d\tau - \frac{1}{r_0}. \quad . \quad . \quad (19)$$

(iii) Exchange energy change :

$$\Delta A = -\frac{3}{4}\left(\frac{3}{\pi}\right)^{1/3}\int [n^{4/3}+n_0{}^{4/3}-n_i{}^{4/3}-n_v{}^{4/3}]\,d\tau. \quad . \quad . \quad (20)$$

(iv) Correlation energy change ΔW : (see especially Gombás 1949, Pines 1955).

This can be obtained in a quite straightforward way using the approximate formula

$$-\frac{0\cdot0564n^{4/3}}{n^{1/3}+0\cdot0795} \quad . \quad . \quad . \quad . \quad . \quad . \quad (21)$$

for the correlation energy density as a function of the electron density n.

The change in energy in each case was evaluated by numerical integration from our relaxation solutions for the densities and the values obtained were as follows:

$$\left. \begin{array}{l} \Delta T = -0\cdot0042 \\ \Delta V = +0\cdot0011 \\ \Delta A = +0\cdot0018 \\ \Delta W = +0\cdot0001 \end{array} \right\} \quad . \quad . \quad . \quad . \quad . \quad . \quad (22)$$

The total change is thus $-0\cdot0012$, and so the energy is lowered by $0\cdot03(3)$ ev with respect to the separated imperfections. If we neglect exchange and correlation, however, the binding energy is increased very significantly, the value being $0\cdot08(4)$ ev. It should, of course, be remembered that we have only included exchange in an approximate way even within the present framework; it would be preferable to use the Thomas–Fermi Dirac method from the beginning and calculate the total energy in this approximation. With the experience gained in the present investigation this should be possible, although it will undoubtedly be a very laborious task. We do not expect the interaction energy to change greatly from our result, although of course it should be remembered that the separate energy terms may well change appreciably. Correlation, as we have seen, is very much less important than exchange, and can probably be safely ignored in future work.

§ 7. CONNECTION WITH FIRST-ORDER RESULTS

As we have already discussed, Lazarus uses the simple form for the interaction energy given by eqn. (2) in his theory, with considerable success, and it is therefore of interest to compare the results of our computations with the first-order arguments of § 3 which were shown to lead to eqn. (2) in the impurity–vacancy case. Putting $Z=1$, $Z'=-1$ and $r_0=5$ in eqns. (7) and (8) and evaluating the kinetic energy change

$$\frac{q^2}{4\pi} \int V_p V_p{}' \, d\tau$$

in confocal elliptic coordinates as

$$\frac{q}{2} \exp\left(-qr_0\right) \quad . \quad . \quad . \quad . \quad . \quad . \quad (23)$$

the following results are obtained

$$\left. \begin{array}{l} \Delta T = -0\cdot0040 \\ \Delta V = +0\cdot0023 \end{array} \right\}, \quad . \quad . \quad . \quad . \quad . \quad (24)$$

to be compared with the results given in eqn. (22).

It will be seen that both methods agree that there is a lowering of the kinetic energy which is sufficiently large to outweigh the increased potential energy, although the binding energy obtained from our computations without exchange and correlation ($0\cdot08(4)$ ev), is considerably larger than that given by the first-order method ($0\cdot045$ ev). Further,

it is clear from our numerical results that the introduction of exchange markedly reduces the binding energy ; a conclusion which can again be qualitatively supported by a first-order argument. It is also of some interest to remark that the final numerical value we obtain for the binding energy (0·03(3) ev) is very close to that given by eqn. (3) : (0·035 ev).

§ 8. Discussion

(i) *Field round Impurity–Vacancy System*

It seems of interest to note briefly here the main conclusions concerning the field and the distribution of electrons which can be drawn from our numerical calculations. We find that a simple superposition of the exact Thomas–Fermi potentials obtained for the isolated imperfections is a fairly good approximation to the potential for the two-centre problem. Also, as we have discussed earlier, using this model together with the Thomas–Fermi approximation there is a slightly distorted sphere round the vacancy (a little smaller than that for an isolated vacancy) in which the electron density is zero, and the negative charge is thus being shielded to the maximum degree by the unneutralized positive charge.

(ii) *Possible Errors Introduced by the Thomas–Fermi Approximation*

It should, of course, be borne in mind that the Thomas–Fermi approximation is not good in regions where the potential is varying rapidly, and corrections ought really to be applied. Attempts to do so have been made previously in simple cases (Scott 1952, March and Plaskett 1956) but so far no successful method having any degree of generality has been proposed. However, we feel that in the present problem, it might eventually be worth while to examine the Weizsäcker correction to the Thomas–Fermi method†.

It is, of course, difficult at the present time to assess the extent to which the errors in the procedure adopted here will affect the interaction energy. In this connection, however, we might perhaps remark that it is difficult to see how the present method applied in an unmodified form to two vacancies, could lead to results such as those of Seeger and Bross (1956) to which we referred earlier. It seems to us that the failure of the present method to allow electrons into regions of negative kinetic energy may be very serious in this latter case, and the possibility that this is a serious source of error in the present work cannot therefore be entirely excluded.

§ 9. Conclusion

We think, however, that in spite of the over-simplified model used and the limitations of the Thomas–Fermi approximation, the present result should be taken as giving some support to the approximate expression (2), perhaps with the modification of (3) introduced, as a

---

† Since this was written Dr. J. Friedel has informed us that he has carried out some computations of the Weizsäcker correction (to be published).

useful representation of the interaction energy between an impurity and a vacancy in a monovalent metal. Thus, while further work is clearly necessary before a definite conclusion can be reached, we suggest that the present investigation tends to substantiate further the Lazarus theory of solute diffusion in metals.

ACKNOWLEDGMENTS

REFERENCES

ALFRED, L. C. R., and MARCH, N. H., 1955, *Phil. Mag.*, **46,** 759 ; 1956, *Phys. Rev.*, **103,** 877.
ALLEN, D. N. DE G., 1954, *Relaxation Methods* (New York : McGraw-Hill).
BARTLETT, J. H., and DIENES, G. J., 1953, *Phys. Rev.*, **89,** 848.
BLATT, F. J., 1955, *Phys. Rev.*, **99,** 600.
DEXTER, D. L., 1952, *Phys. Rev.*, **87,** 768.
FRIEDEL, J., 1954, *Advances in Phys.*, **3,** 446.
FUJIWARA, H., 1955, *J. Phys. Soc. Japan*, **10,** 339.
GLAZER, H., and REISS, H., 1953, *J. chem. Phys.*, **21,** 903.
GOMBÁS, P., 1949, *Die Statistiche Theorie des Atoms und Ihre Anwendungen* (Vienna : Springer).
LAZARUS, D., 1954, *Phys. Rev.*, **93,** 973 : 1955, *Impurities and Imperfections* (New York : American Society for Metals).
MARCH, N. H., 1957, *Advances in Phys.*, **6, 1.**
MARCH, N. H., and PLASKETT, J. S., 1956, *Proc. roy. Soc.* A, **235, 419.**
MOTT, N. F., 1936, *Proc. Camb. phil. Soc.*, **32,** 281.
PINES, D., 1955, *Solid State Physics* (New York : Academic Press). Vol. 1, p. 367.
SCOTT, J. M. C., 1952, *Phil. Mag.*, **43,** 859.
SEEGER, A., and BROSS, H., 1956, *Z. Phys.*, **145,** 161.
SONDER, E., SLIFKIN, L., and TOMIZUKA, C. T., 1954, *Phys. Rev.*, **93,** 970.
SOUTHWELL, R. V., 1946, *Relaxation Methods in Theoretical Physics* (Oxford : University Press).
SWALIN, R. A., 1956, *J. appl. Phys.*, **27,** 554.
TOMIZUKA, C. T., and SLIFKIN, L., 1954, *Phys. Rev.*, **96,** 610.
TOMIZUKA, C. T., and SONDER, E., 1956, *Phys. Rev.*, **103,** 1182.

A Graphical Method for the Determination of Half-Lives†

By I. Kuščer, M. V. Mihailović
Institute of Physics, Ljubljana, Yugoslavia

and E. C. Park‡
Department of Physics, University of Birmingham

Abstract

The graphical determination of half-lives of radioactive isotopes can be made more accurate if the remaining number of counts, instead of the counting rate, is plotted as a function of time. This method has been used to measure the half-life of ^{27}Si, for which the value 4.14 ± 0.03 seconds has been obtained.

§ 1. Introduction

THE decay of a radioactive isotope is usually followed by counting the number of disintegrations (or a constant fraction thereof, according to the geometry and sensitivity of the counter) during successive time intervals. From the data so obtained the half-life is estimated either numerically or, less accurately, graphically from a semilogarithmic plot of the counting rate. It will be shown that the accuracy of the graphical method can be improved if a modified way of plotting is used. For comparison some numerical methods will be reviewed first.

§ 2. Numerical Methods

Peierls (1935) has given the following formula for the mean life time $(\tau = t_{1/2}/\ln 2)$ of a simple activity, if no background is present :

$$\tau \simeq \bar{t} + t_k [\exp{(t_k/\tau)} - 1]^{-1}, \quad \ldots \ldots \ldots \quad (1)$$

where t_k is the total counting time and $\bar{t}$ the time coordinate of the centroid of the observed counts. If $0 = t_0 < t_1 < \ldots < t_k$ and if n_ν is the number of counts during the time interval $\Delta t_\nu = t_\nu - t_{\nu-1}$, then $\bar{t} \simeq \sum_1^k n_\nu \bar{t}_\nu / n$, where $n = \sum_1^k n_\nu$, and $\bar{t}_\nu$ is the average time coordinate of the centroid of the counts in the interval Δt_ν, i.e.

$$\bar{t}_\nu = \tfrac{1}{2}(t_{\nu-1} + t_\nu) - \tau[(\tfrac{1}{2}\Delta t_\nu/\tau) \coth{(\tfrac{1}{2}\Delta t_\nu/\tau)} - 1]$$

$$= \tfrac{1}{2}(t_{\nu-1} + t_\nu) - \Delta t_\nu \left[\frac{1}{12}(\Delta t_\nu/\tau) - \frac{1}{720}(\Delta t_\nu/\tau)^3 + \ldots \right].$$

† Communicated by the Authors.
‡ Present address : Arthur D. Little, Inc., Cambridge, Mass., U.S.A.

Another formula, less simple than (1), is obtained if the method of least squares is applied to the semilogarithmic plot of the counting rate (fig. 1). The result is (Behrens 1951)

$$\tau \simeq \frac{\sum_1 n_\nu (t^* - t_\nu^*)^2}{\sum_1^k n_\nu (t^* - t_\nu^*) \ln (n_\nu/\varDelta t_\nu)}, \qquad \cdots \cdots \quad (2)$$

where $t^* = \sum_1^k n_\nu t_\nu^*/n$, and t_ν^* is the time at which, in the average, the counting rate is equal to $n_\nu/\varDelta t_\nu$, i.e.

$$t_\nu^* = \tfrac{1}{2}(t_{\nu-1} + t_\nu) - \tau \ln \left[\sinh \left(\tfrac{1}{2}\varDelta t_\nu/\tau\right)/\left(\tfrac{1}{2}\varDelta t_\nu/\tau\right)\right]$$

$$= \tfrac{1}{2}(t_{\nu-1} + t_\nu) - \varDelta t_\nu \left[\frac{1}{24}(\varDelta t_\nu/\tau) - \frac{1}{2880}(\varDelta t_\nu/\tau)^3 + \ldots\right].$$

The calculation of the corrected mid-point t_ν^* can be simplified if the time $t_{\nu\ 1/2}$ which halves the number of counts, n_ν, in the interval $\varDelta t_\nu$ is also recorded. The point t_ν^* lies, on the average, very nearly two-thirds of the way from the mid-count point to the mid-time point so that

$$t_\nu^* \simeq t_{\nu-1/2} + \tfrac{2}{3}\left[\tfrac{1}{2}(t_{\nu-1} + t_\nu) - t_{\nu-1/2}\right] = \tfrac{1}{3}(t_{\nu-1} + t_{\nu-1/2} + t_\nu). \quad \cdots \quad (3)$$

(The next term of this approximation is $-\varDelta t_\nu^4/720\tau^3$.) This method has been found useful for plotting counting rates.

Fig. 1
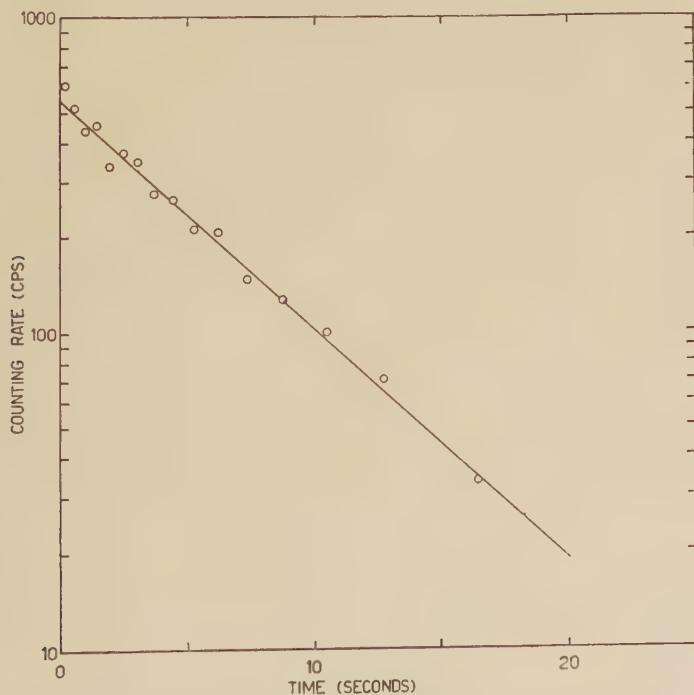
The mean square error σ_τ^2, due to statistical fluctuations, is the same for both expressions, (1) and (2), if $\varDelta t_\nu \ll \tau$. If moreover $t_k \gg \tau$, then

$$\sigma_\tau^2 = \tau^2/n. \qquad \cdots \cdots \cdots \quad (4)$$

This is the minimum value of the mean square error which can be attained with the same total number of observed counts (n) (Peierls 1935).

Instead of plotting the counting rate we may plot its integral, i.e. the number of remaining counts which at $t=t_\nu$ is $N_\nu = \sum_{\nu+1}^{k+1} n_\mu$ (fig. 2). For this purpose the counting must be continued until the activity dies out or until the remainder $(N_k=n_{k+1}=N_0-n)$ can be estimated. The method of least squares now leads to

$$\tau \simeq \frac{\sum_1^k a_\nu t_\nu}{\sum_1^k a_\nu \ln (N_0/N_\nu)} . \qquad \qquad . \quad . \quad . \quad . \quad . \quad (5)$$

The weights a_ν must be so chosen that the mean square error becomes least. If $\Delta t_\nu \ll \tau$, the proper choice is $a_\nu=\frac{1}{2}(n_\nu+n_{\nu+1})$ for $\nu<k$, and $a_k=\frac{1}{2}n_k+n_{k+1}$, which minimizes the mean square error to $\sigma_\tau^2=\tau^2/n$ if $t_k \gg \tau$. With such weights the formula (5) differs only insignificantly from (1).

Fig. 2
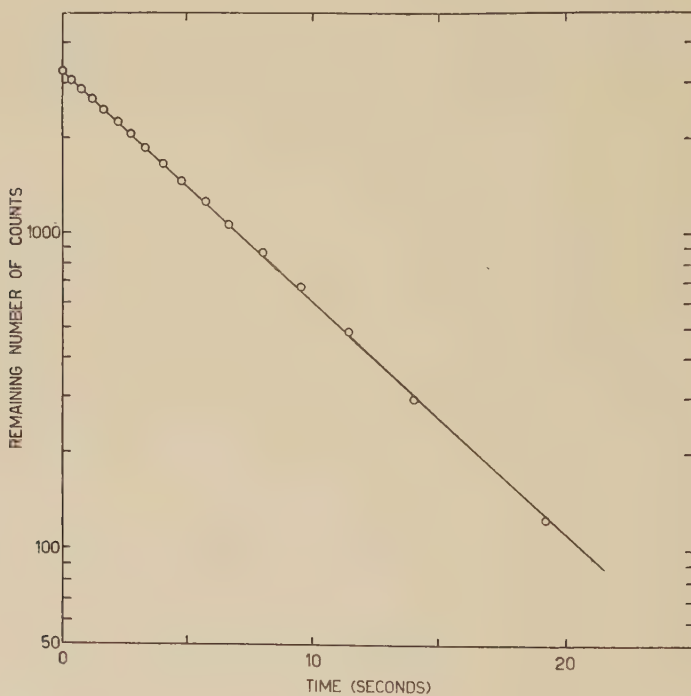
§ 3. A Graphical Method

As indicated above, the method of least squares, applied either to the numbers n_ν or N_ν, leads to results of the same accuracy in both cases. The graphical method, however, distinctly favours the plot of the remaining number of counts (fig. 2), where it is easier to guess a correct straight line than in the counting-rate plot (fig. 1). Even a straight line through only two points, a few half-lives apart, will give good accuracy. According to Peierls (1935) the points must be taken at $t=0$ and $t=1\cdot6\tau$,

in order to minimize the mean square error to $\sigma_\tau^2 = 1{\cdot}54\tau^2/N_0$. This can be improved with three points (A, B, C) and a straight line which goes through the first point (A) and bisects the angle BAC. The minimum $\sigma_\tau^2 = 1{\cdot}22\tau^2/N_0$ is reached if the points are taken at $t=0$, $t=1{\cdot}0\tau$ and $t=2{\cdot}5\tau$. Hence any straight line, reasonably well fitting the points in the plot, will give the life time to an accuracy of the same order as the numerical methods, provided that the accuracy of the drawing itself is sufficient.

Some details of this method will be included in the subsequent report about a measurement of the half-life of ^{27}Si.

§ 4. THE HALF-LIFE OF ^{27}Si

This isotope was produced by the ^{27}Al (p, n) reaction in the external proton beam (10 MeV) of the Birmingham cyclotron, and later also by the ^{28}Si (γ, n) reaction, using x-rays (maximum 26 MeV) from the Ljubljana betatron. In both cases a pneumatic tube system was used to transfer the target to a scintillation counter, in order to observe the decay. A chronograph, connected to the output of a scaler, recorded every hundredth or thousandth pulse of the counter upon teledeltos paper tape (Kuščer and Mihailović 1955). The scaling ratio was so chosen that more than a sufficient number of marks were obtained. When reading the marks a wider ratio (e.g. 1 : 200 or 1 : 2000) was chosen, so that in the central part of the diagram about two points per half-life were obtained.

1	2	3	4	5
ν	t_ν (sec)	Δt_ν (sec)	b_ν	N_ν
0	0			3252
		0·33	−2	
1	0·33			3050
		0·39	−2	
2	0·72			2848
		0·46	−1	
3	1·18			2647
.	.	.	.	.
.	.	.	.	.
.	.	.	.	.
15	14·08			295
		5·15	28	
16	19·23			123
		16·24	86	
$k=17$	35·47			$N_k - 9$ (estimated)

The further working scheme is shown by the accompanying table, which contains the data of a single experiment with a rather poor number of counts. The time coordinates t_ν of every second mark, i.e. of every 200th

pulse, are read from the paper tape (column 2). The differences Δt_ν (column 3) are taken, and the background and dead time corrections estimated (the sum of both being b_ν, column 4). At the lower end of the table, where the background starts to exceed the true activity, the remaining number of 'true' pulses (N_k) has to be estimated. For this purpose an approximate value of the half-life can be used. Then the remaining counts N_ν (column 5) are built up, working backwards, by summing the $n_\nu = 200 - b_\nu$. The equation $N_0 = k.200 + N_k - \sum_1^k b_\nu$ provides a check. Then the plot is made (fig.2) and the half-life read from it.

Only a single decay of the ^{27}Al (p, n) activity, comprising over 90 000 counts, has been used for the half-life determination (Park 1955). Some uncertainty was caused by an unknown dead time of the electronic equipment. The counting rate plot led to the value $t_{1/2} = 4.1 \pm 0.1$ sec, and also permitted the dead time to be estimated. Using this estimate the data were replotted on a graph of the remaining number of counts (which is less sensitive to dead time variations), whereby the value $t_{1/2} = 4.14 \pm 0.03$ sec resulted.

Eight measurements with x-ray activated silicon were made, with the number of counts (N_0) ranging from 3000 to 7000, the total number of counts being 45 000. The average happened to be identical with the previous result :

$$t_{1/2} = 4.14 \pm 0.03 \text{ sec.}$$

The differences between the individual values of the half-life and the average were consistent with the expected statistical deviations. Therefore the standard error of the average was estimated according to eqn. (4). increased by the appropriate factor on account of the back-ground (Peierls 1935). The quoted result is in satisfactory agreement with the value 4.05 ± 0.10 of Hunt *et al.* (1954).

REFERENCES

BEHRENS, D. J., 1951, *A.E.R.E. Report* T/R 629, Harwell.
HUNT, W. A., KLINE, R. M., and ZAFFARANO, D. J., 1954, *Phys. Rev.*, **95**, 611.
KUŠČER, I., and MIHAILOVIĆ, M. V., 1955, *Rep. Inst. J. Stefan* (Ljubljana), **2**, 51.
PARK, E. C., 1955, *Ph.D. Thesis*, University of Birmingham.
PEIERLS, R., 1935, *Proc. roy. Soc.* A, **149**, 467.

Rectilinear Etch Pits on Diamond†

By S. Tolansky and A. R. Patel
Royal Holloway College, University of London, Egham, Surrey

Abstract

It is established that the rectilinearity of the pits formed by etching octahedral faces of diamond depends in a sensitive manner on the temperature and rate of etch. Etching in potassium nitrate at 475°c, although slow, produces rectilinear pits. At 525°c etching is much faster and the pits round off in the familiar manner already long known.

§ 1. Introduction

Several investigators have described the etching effects on diamond produced by strong oxidation. (For literature see Pandya and Tolansky, *Proc. roy. Soc.* A, **225**, 33–48, 1954.) Thus etching can be produced by hot flames rich in oxygen, or by heating diamonds in a melt of potassium nitrate. In this laboratory extensive studies have been made with nitrate fluxes but at temperatures varying from 525°c to 750°c which are much lower than those used by earlier workers.

On octahedral faces the etch pits are invariably equilateral, triangular shaped pits which are always oppositely oriented to the well known equilateral growth trigons. The pits so found are most frequently rounded off at the corners, whilst, on the contrary, the familiar growth trigons are almost invariably strictly rectilinear in outline.

Now recently, in a personal communication, M. Omar of Cairo informed us that he and Kenawi have produced *rectilinear* etch pits by a novel method of etching‡. Their diamond was supported on a tungsten filament at some 1000°c, in a vacuum chamber which contained a very small amount of air. After some hours, small, but rectilinear, etch pits formed, being, as always, oppositely oriented to the growth trigons.

In this present paper we prove that the shape of diamond etch pits is determined by the rate of etching : the pits can be arbitrarily produced either of rectilinear or curvilinear outline.

---

† Communicated by the Authors.
‡ Their results have since been published in the July issue of this volume, page 859.

§ 2. Experimental

We have carried out several experiments but select one set only. A diamond was cleaved on (111) in order to secure (111) surfaces free from the complication of natural trigons. We have already established (and are describing elsewhere) that when oppositely matched cleavage faces are etched, there is a remarkable correlation of the triangular etch patterns on the two separated faces.

In etching with hot nitrate in this laboratory, we have usually formerly found that etching only really effectively sets in after 525°c, and have generally found that a one or two hour etch at this temperature produces a satisfactory early stage etch pattern, despite the fact that earlier authors advocated temperatures of at least 900°c and more. Etching below 525°c is normally so very slow that we have generally ignored lower temperatures in most of our etching experiments. However we began to etch here at 475°c.

Etching was very slow indeed but we found that at this temperature the pits formed are in fact rectilinear (although small). Thus Plate 37 (*a*) (×712) shows a region etched for no less than 24 hours at 475°c. Plate 37 (*b*) (×712) shows the same region after being subject to attack for 42 hours at 475°c. Plate 37 (*c*) is a selected region of this, at magnification 1120. We see quite clearly that rectilinear pits have formed, increasing in size with time of etch. There is merely the barest suspicion of rounding at the corners in some of the pits, but not in all.

Now a mere increase in etching temperature of only 50°c (to 525°) makes a striking change. We have traced this effect by two independent methods. In the first method we have etched the one face for a long time at 475°c. Simultaneously we have etched the other (untouched) matched cleavage face at 525°c for successive (much shorter) times. In the second method we have selected some of the rectilinear pits already formed at 475°c and then exposed them to the etchant at 525°c.

The slowly etched face of method (1) is that already shown in Plate 37 (*a, b, c*). The corresponding matched face is shown in Plate 37 (*d, e, f*). Plate 37 (*d*) (×712) shows that $3\frac{1}{2}$ hours at 525° leads to the long familiar pits which are distinctly rounding off into hexagon shapes. Plate 37 (*e*) (×712) after 6 hours at 525°c shows the increase in size and in Plate 37 (*f*) at ×1120 a shape which may now well be compared with the rectilinear pattern of Plate 37 (*c*) which is shown by the matched cleavage etched at the lower temperature of 475°c. (It is of course quite clear that because we are dealing with a cleavage pair, the etch pits must of necessity be oppositely oriented on the two oppositely cleaved faces.)

Equally striking are the effects shown by method (2). Thus Plate 38 (*a*) (×712) shows a rectilinear pattern produced by a 42 hours etch at 475°c. Plate 38 (*b*) (×712) then shows this identical region after a further exposure to etchant for $1\frac{1}{2}$ hours but now at 525°c. The marked set-in of rounding is clear. Further etching for another $1\frac{1}{2}$ hours at

525°C leads to Plate 38 (*c*) (×712) and here the long familiar rounded etch pits with flat bottoms have finally appeared. The growing pits are now beginning to eat into each other. This change in character has been produced by a mere 50°C increase in temperature.

Another example of the successive conversion of a rectilinear system into a curvilinear system is shown in Plate 38 (*d*, *e*, *f*). Both examples in Plate 38 are typical of many cases we have studied.

It should be recognized that even at 525°C the etching is still quite mild, for it still takes no less than 6 hours to produce the quite small pits of Plate 37 (*e*). Indeed it was this very slowness even at 525°C which led us initially to adopt this temperature as a reasonable starting place for our earlier extensive work on etching numerous diamond crystals.

§ 3. Conclusions

We have thus established two features (*a*) the rectilinearity or curvilinearity of the etch pits depends only upon the temperature of etch, i.e. primarily on the rate of etch (*b*) rectilinearity is highly sensitive to temperature, a mere 50°C change altering the whole character.

It is now clear that the appearance of rectilinear patterns merely implies a slow rate of etch. The rectilinearity of slowly formed etch pits has of course no connection at all with the familiar growth trigons which are oppositely oriented.

In previous communications Tolansky only obtained the familiar somewhat rounded etch pits. We see now that this was because his etching, even at 525°C, was not sufficiently mild. It requires a really slow etching to retain rectilinearity. How slow an etching is needed is shown by the fact that the long 42 hour etch at 475°C produces pits whose sides are a mere 1/2000 cm in length.

Acknowledgment

On the 8·06 and 8·70 MeV States in ^{14}N†

By C. Broude, L. L. Green, J. J. Singh and J. C. Willmott
Nuclear Physics Research Laboratory, University of Liverpool

§ 1. Introduction

We have recently reported measurements on the γ-rays emitted by the 1', $T=1$ state at 8·06 MeV in ^{14}N (Broude *et al.* 1957). This level has a rather large isotopic spin impurity ($\sim 7\%$) and a possible explanation of this has been given by Wilkinson and Clegg (1956) in terms of mutual contamination by the four states formed from a single 2s particle with the ground state of ^{13}C as a unique parent. In a previous paper we suggested a possible identification of these four states on the basis of the weak decay modes of the 8·06 MeV state. The 8·70 MeV state in ^{14}N is, like the 8·06 MeV state, a very broad level formed by s-wave capture of protons by ^{13}C. It is a 0', $T=1$ state and possibly a member of this quartet of states. The present investigation had two purposes. Firstly to investigate the γ-ray decay scheme of the 8·70 MeV level and secondly to investigate the isotropy of the ground state transition from the 8·06 MeV state to see if the ingoing particle is purely s-wave. If there is a substantial d-wave component present the number of similar states likely to mix in is increased and the whole situation is much more complex.

§ 2. Experimental

The 8·70 MeV state in ^{14}N is formed by bombarding ^{13}C with protons of 1·25 MeV. This energy is above the range of the 1 MeV H.T. set in this laboratory, but due to the large width of this resonance the yield at 1 MeV is one half the yield at the peak. Owing to this large width it is impossible to eliminate contamination γ-rays by bombarding the target on and off resonance. Consequently we observed the γ-rays at two different bombarding energies, 1 MeV and 900 keV, and compared the relative intensities. In addition the target backing was bombarded after each run as a further aid to the removal of background. A target of 70% ^{13}C was used, of about 50 keV thickness at 550 keV and 30 keV thickness at 1 MeV. About 0·8% of the target area was found to be thick, giving rise to a small yield from the 550 keV resonance at 1 MeV bombarding energy. This contribution could be readily subtracted.

The γ-ray intensity measurements were carried out in the manner described in the previous paper. The relative intensities of the γ-rays observed at the two bombarding energies after correction for the yield

from the thick target area are shown in table 1. The suggested decay scheme is shown in the figure. It will be seen that there is good agreement between the intensities at the two bombarding energies except for the γ-ray leading to the 3·95 MeV level and its subsequent decay to the 2·31 MeV level. As the 2·31 MeV level is fed in other ways the discrepancy does not show up so strongly in the intensity of this γ-ray.

Angular distribution measurements were made at three bombarding energies, 500 keV, 572 keV and 672 keV corresponding to mean energies in the target of 480 keV, 550 keV and 650 keV. The results are shown in table 2.

Table 1

$E_P = 1$ MeV		$E_P = 900$ keV	
$E\gamma$(MeV)	Relative intensity	$E\gamma$(MeV)	Relative intensity
8·46	100 ± 5	8·39	100 ± 5
5·69	3·2 ± 0·4	5·69	2·9 ± 0·4
5·10	2·1 ± 0·4	5·10	2·8 ± 0·4
4·92	3·2 ± 0·4	4·91	4·0 ± 0·4
4·51	2·1 ± 0·4	4·43	6·1 ± 0·4
3·55	4·1 ± 0·4	3·48	4·5 ± 0·4
3·38	6·5 ± 1·0	3·39	8·9 ± 1·0
2·79	12·3 ± 1·0	2·72	14·0 ± 1·0
2·31	7·9 ± 1·0	2·31	10·5 ± 1·0
1·64	1·9 ± 0·3	1·64	4·6 ± 0·5

Table 2

Proton energy	Observed distribution
480 keV	$1 + (0·00 \pm 0·01)P_2$
550 keV	$1 + (0·008 \pm 0·008)P_2$
650 keV	$1 + (0·023 \pm 0·006)P_2$

§ 3. Discussion

In addition to the main ground state transition, direct transitions from the resonance level occur to the levels at 3·95 MeV, 4·91 MeV, 5·10 MeV and 5·69 MeV. These are the same levels as are fed from the 8·06 MeV level, with the exception of the 5·10 MeV level which was not fed from the lower resonance.

The strongest of these transitions is to the 5·69 MeV state. In the previous paper we suggested that this state might be the 1$^-$, $T = 0$ member of the quartet of s-particle states, as its decay to the ground and first excited states is in the expected ratio if it is the sole contaminator

of the 8·06 mev state. Since that work was completed Wilkinson and Bloom (1957) have shown that the 6·23 mev level in ^{14}N also decays to the ground and first excited state in the correct ratio for it to be the sole contaminator for the 8·06 mev level. This contaminating state should be 1$^-$ and the observed strength of the transition to the 5·69 mev state

^{14}N
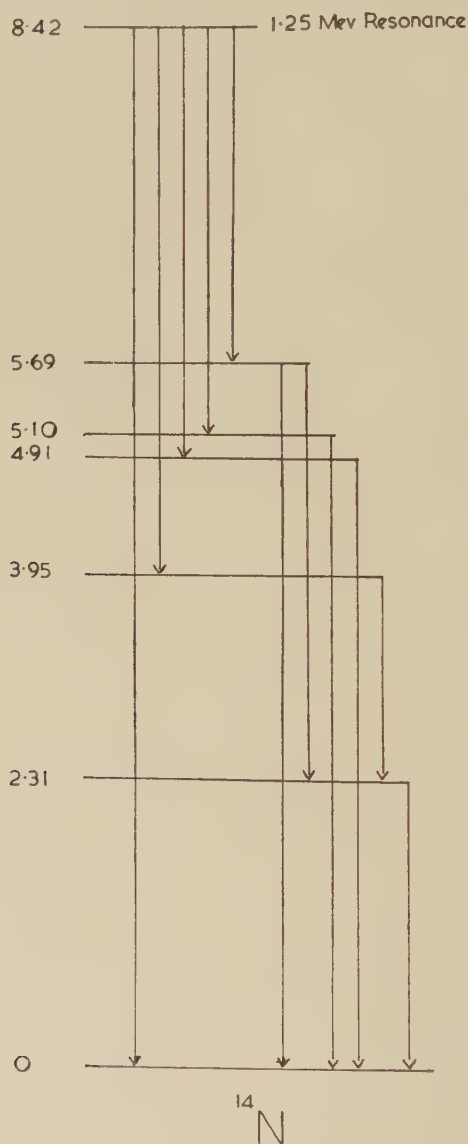
from the 1·25 mev resonance level helps to decide whether this is a possible spin and parity for the 5·69 mev state. Taking the radiation width of the 8·70 mev level for decay to the ground state as 46 ev (Woodbury *et al.* 1953) the radiation width for decay to the 5·69 mev level is 6·0 ev.

This corresponds to 13 Weisskopf M1 units, which is four times higher than the strongest authenticated M1 transition (Wilkinson 1956). If this transition is an E1 transition then the radiation width is 0·45 Weisskopf units, which is above average E1 strength. Thus it seems fairly certain that the transition to the 5·69 Mev level is an E1 transition and this state cannot be 1$^-$, but is 1$^+$.

3.1. *The* 4·91 *MeV Level*

The existence of the transition to the 4·91 Mev state from the 0$^-$ 8·70 Mev state shows that the former level cannot have zero spin, as is generally assumed. The evidence for this assignment comes from the ^{13}C (d, n)^{14}N stripping results of Benenson (1953) which appear to show that the 4·91 Mev level is 0 or 1$^-$. The absence of a transition to the 0$^+$ state at 2·31 Mev and the fact that the 4·91 Mev level is not fed from the 0$^+$ resonance at 1·16 Mev have previously favoured the 0$^-$ assignment. The existence of the transition to the 4·91 Mev state at this resonance means that the level is presumably 1. However, the decay of this state is difficult to reconcile with the 1 assignment, for the isotopically allowed E1 transition to the 0$^+$, 2·31 Mev state is not observed whereas the isotopically forbidden transition to the ground state is. The conditions for observing these transitions are better at the 550 kev resonance but here also the isotopic spin favoured transition was not observed. Further the radiation width for the transition to the 4·91 Mev state is 1·8 ev which corresponds to the rather high value 1·9 Weisskopf M1 units. It thus seems that the 4·91 Mev state requires further investigation before its spin and parity can be stated with confidence.

3.2. *The* 5·1 *MeV Level*

The radiation width for the transition to the 5·10 Mev state corresponds to 1·4 M1 units or 0·047 E1 units. These transition strengths are consistent with an assignment of 1 or 1$^+$ but the absence of a strong transition to the 2·31 Mev level from the 5·10 Mev level rather favours 1$^+$.

§ 4. Angular Distribution

The angular distribution measurements show some evidence for anisotropy at 550 kev bombarding energy and a quite definite anisotropy at 650 kev. At 650 kev the ground state yield is partially due to a contribution from the very wide 1·25 Mev resonance which is essentially isotropic and adds incoherently as the 1·25 Mev and 550 kev resonances are formed through different spin channels. In addition there is also the small thick target yield. After correcting for these effects we are left with a distribution of the form $1 + (0·04 \pm 0·01)P_2$. Using the radius which Milne (1954) has used for the analysis of the elastic scattering results, namely $r = (1 + 1·41 \times 13^{1/3}) \times 10^{-13}$ cm we have computed the amount of d-wave contribution required to produce such a distribution.

The relative phase of the ingoing s- and d-waves at these bombarding energies is determined almost exclusively by the coulomb field and is very nearly independent of the assumed value of the nuclear radius. At 650 kev this angle is 81° and is increasing slowly as the bombarding energy is lowered. As a result, the interference term, though still the dominant term, is small and the d-wave intensity required is 6·05% of the s-wave intensity. The relative intensities of the s- and d-waves calculated from barrier penetrability alone is 1·69%.

On the assumption that the ratio of the s- and d-wave intensities varies across the resonance in the ratio of their penetrabilities, the expected distribution at 550 kev is $P_0 + 0·014P_2$ in reasonable agreement with the observed $1 + (0·008 \pm 0·008)P_2$. The reduced width of this resonance is 13% of the Wigner s-wave limit. The d-wave contribution is thus approximately 45% of the Wigner d-wave limit. Any reduction in the radius used makes the d-wave contribution an even larger proportion of the d-wave sum. It thus seems that the description of this level in terms of the ¹³C core and a single 2s particle is not well founded and that mixed configurations must be employed involving a large amount of d-wave.

REFERENCES

BENENSON, R. E., 1953, *Phys. Rev.*, **90**, 420.
BROUDE, C., GREEN, L. L., SINGH, J. J., and WILLMOTT, J. C., 1957, *Phil. Mag.*, **2**, 499.
MILNE, E. A., 1954, *Phys. Rev.*, **93**, 762.
WILKINSON, D. H., 1956, *Phil. Mag.*, **1**, 127.
WILKINSON, D. H., and BLOOM, S. D., 1957, *Phil. Mag.*, **1**, 63.
WILKINSON, D. H., and CLEGG, A. B., 1956, *Phil. Mag.*, **1**, 291.
WOODBURY, H. H., DAY, R. B., and TOLLESTRUP, A. V., 1953, *Phys. Rev.*, **92**, 1199.

The Flow Stress of Polycrystalline Aluminium†

By C. J. Ball

Crystallographic Laboratory, Cavendish Laboratory,
Cambridge, England

Abstract

It is shown that there is a strong correlation between flow stress and subgrain size in polycrystalline aluminium deformed in tension ; the strength of the boundaries does not appear to depend on boundary angle. The variation of flow stress with temperature suggests that the strength controlling factor is elastic interaction.

§ 1. Introduction

Kelly (1954) extending a theory of Gay et al. (1954), has suggested that the flow stress, σ, at any point on a stress strain curve of a polycrystalline metal specimen is determined by the instantaneous value of the subgrain size, t, according to the relation $\sigma \propto t^{-1\cdot2}$. Using the experimentally observed variation of subgrain size with strain he finds good agreement with the stress/strain curves of aluminium and iron.

However, determinations of subgrain size at low strains, where most change occurs, show considerable scatter, and the effect of other variables which might be expected to affect the flow stress, such as boundary angle, was not investigated. For these reasons the subject has been re-investigated. Measurements have been made, using the x-ray microbeam technique, of the subgrain size and range of misorientations in one original grain in a series of specimens, and these have been correlated with the flow stress. For details of the x-ray measurements see Hirsch and Kellar (1952). In addition, the variation of flow stress with temperature has been determined, in the hope that it would throw some light on the processes occurring at yield.

§ 2. Experimental Method

Tensile test specimens were made from superpure aluminium (99·994%) and recrystallized at 550°c to give strain free grains of size ∼200 μ. These specimens were then strained by amounts ranging up to 35% extension at temperatures in the range −183°c to 375°c. By this means a set of specimens was prepared in which subgrain size and

---

† Communicated by the Author.

misorientations were not closely related, as would have been the case for
deformation at a single temperature.   The influence of temperature of
deformation on substructure will be described in a later paper.

Fig. 1
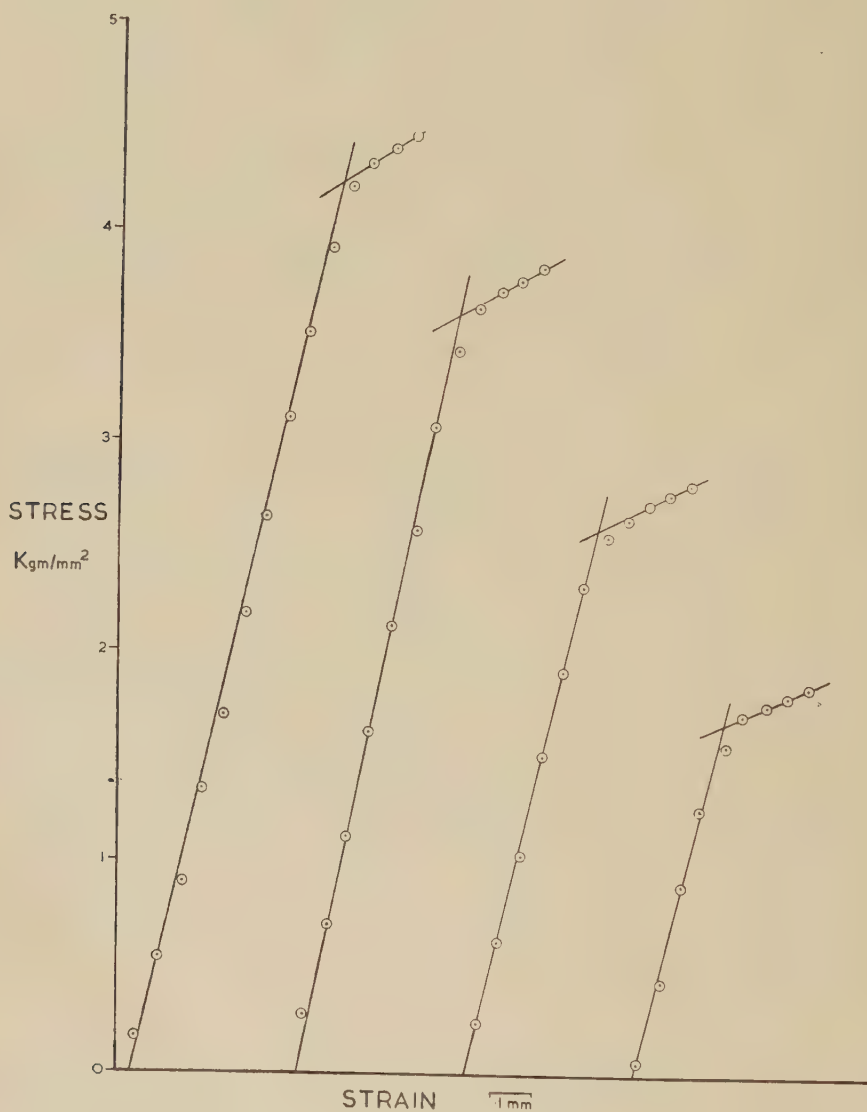
Typical restrain curve.

Before x-ray examination all specimens were etched to a depth of
$\sim 30\,\mu$, as the surface layers are not characteristic of the interior of
the metal.   Microbeam photographs showed that internal strains in

specimens deformed at low temperatures were large. Accordingly, these specimens were annealed for 12 hours at 140°c. As Kelly (1953) has observed, the effect of such a treatment is to sharpen the spots on a microbeam photograph and to eliminate the background between them, without greatly affecting either the subgrain size or the angular extent of an arc. After this treatment internal strains, as estimated from microbeam photographs, were comparable in all specimens.

The specimens were finally restrained at 0°c in a hard beam machine of Polyani type at a rate $2 \cdot 5 \times 10^{-5}$ sec^{-1}. Typical restrain curves are shown in fig. 1. The intersection of the two straight portions of each curve is taken as a measure of the flow stess, σ. Some plastic flow does occur at lower stresses, particularly in specimens that have been annealed. In table 1 are listed values of subgrain size, t, range of misorientations, β, and flow stress, σ, for all specimens.

Table 1

$t\mu$	$\beta°$	σ Kg/mm^2	$t\mu$	$\beta°$	σ Kg/mm^2
40	1·0	1·04	3·6	7·9	3·19
25	1·0	1·04	4·3	4·5	3·53
18	2·3	1·44	3·3	7·0	4·21
14	4·5	1·40	9·0	1·0	2·17
20·5	0·8	1·41	6·6	2·0	3·40
16·5	2·6	1·71	4·45	3·6	4·02
12	4·0	2·56	2·5	7·8	4·34
16	1·0	1·91	3·2	4·5	3·61
11·5	3·0	2·25	1·8	9·0	5·20
5·2	5·0	2·74	1·0	7·3	7·36

The variation of flow stress with temperature cannot be deduced from these results as many of the specimens were annealed before restraining. Instead, following Cottrell and Stokes (1955), specimens were deformed 5% at a high temperature, cooled to the reference temperature and restrained to just beyond the flow point, strained a further 5% at the high temperature and so on, giving several values for the ratio of the flow stresses at each pair of temperatures. The temperatures were obtained with the following baths:

> —77°c solid CO_2 in acetone
>   0°c ice in water
> 100°c oil bath controlled to $\pm 1°$c.
> 200°c to 500°c salt bath controlled to $\pm 2°$c.

The time taken to change a bath was standardized at 15 minutes. Results are summarized in table 2, together with the ratio of the flow

stresses after correction for the change of elastic constants with temper-
ature (taken from Koster 1948). A high reference temperature was
chosen for specimens strained at the highest temperatures as the initial
rate of work hardening on restraining at 0°c was too great to allow an
accurate determination of the flow stress to be made. These readings
are scaled to a reference temperature of 0°c using the relation

$$(\sigma_2/\sigma_3)(\sigma_3/\sigma_1)=(\sigma_2/\sigma_1).$$

This relation has been tested by Cottrell and Stokes (1955). In fig. 2
(σ_T/σ_0), after correction for the change in shear modulus, is plotted
against temperature.

Table 2

$T°$c	$T_{\mathrm{Ref}}°$ c	$\sigma_T/\sigma_{\mathrm{Ref}}$			σ_T/σ_0
0	−77	0·94	0·95	0·95	1·02
100	0	0·96	0·89	0·90	0·97
200	0	0·89	0·90	0·85	0·97
250	0	0·79	0·80	0·77	0·89
300	0	0·68	0·65	0·65	0·78
350	0	0·54	0·56	0·55	0·68
400	300	0·73	—	—	0·62
450	300	0·66	—	—	0·60
500	400	0·92	—	—	0·64
550	450	0·90	—	—	0·61

Fig. 2
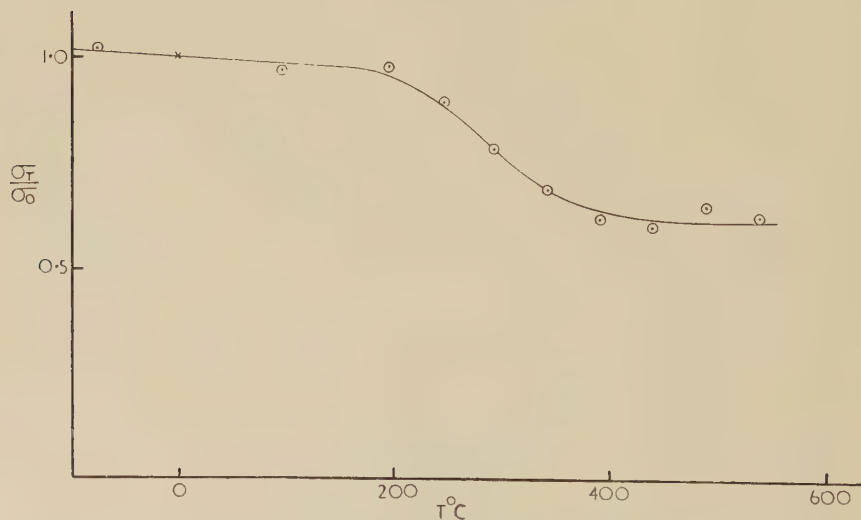
Ratio of flow stress σ_T at temperature T to flow stress σ_0 at 0°c.

§ 3. DISCUSSION

Consider dislocations piled up against a subgrain boundary. The shear stress at the head of a pile up of n dislocations under an applied shear stress τ is $n\tau$. If the criterion for flow is that this stress shall exceed some boundary strength τ_B, we have

$$n\tau = \tau_B.$$

Now

$$n = \frac{\pi l k}{Gb} \cdot \tau$$

where l is the length of the pile up, k is a factor of order unity, G the shear modulus, and b the Burgers vector of the dislocations (Cottrell 1953). Hence

$$\tau = \left(\frac{Gb}{\pi k}\right)^{1/2} l^{-1/2} \tau_B^{1/2}.$$

The tensile flow stress σ will be proportional to τ. If the polycrystalline specimen is homogeneously stressed, for the most favourably oriented slip system we have $\tau = \frac{1}{2}\sigma$. The boundary angle α may be expected to affect τ_B. The relation between α and the experimentally observed quantity β is not known with certainty. For a random distribution of orientations (Gay *et al.* 1953),

$$\alpha \simeq \beta/3,$$

and this will be assumed. If we equate the length of a pile up to the subgrain size t we get a relation between σ, t and β of the form

$$\sigma = At^{-1/2}f(\beta)$$

where A is a constant. To test for this a regression equation of the form

$$\log \sigma = a_1 + b_2 \log \beta + b_3 \log t$$

has been fitted to the data, by standard methods, with the coefficients $a_1 = 0\cdot898$, $b_2 = -0\cdot024$, $b_3 = -0\cdot558$. The coefficients of correlation are $r_{12\cdot3} = -0\cdot08$, $r_{13\cdot2} = -0\cdot92$. It appears, then, that there is a strong correlation between σ and t which is not significantly different from that proposed by Gay *et al.* namely $\sigma \propto t^{-1/2}$ but that σ and β are virtually uncorrelated. In fig. 3 σ is plotted against $t^{-1/2}$.

The slope of the line, with the assumptions mentioned, yields

$$\tau_B \sim G/50.$$

It is not at present possible to explain the strength of the boundaries.

Gay *et al.* considered the stress a distance x ahead of a pile up, and took as their criterion of flow the formation of a dislocation loop by thermal fluctuations. According to Frank (1950) this can occur at room temperature if the stress is of the order of $G/25$. In view of the value for the boundary strength deduced here, it may seem surprising that they found such large stresses to occur. Part of the explanation is that they took $\tau = \sigma$. Also, as their specimens were not annealed, their flow stresses were higher than for comparable specimens in the present work. The anneal also reduces the subgrain size slightly.

The stress distribution inside the polycrystalline specimen is not known, and it may be that stresses at the head of a pile up are as high as $G/25$. Most of the energy to form the new dislocation loop is provided by the applied stress. so dependence of the critical strength on temperature is slight, and would probably not be detected.

In the neighbourhood of $0°c$ the change in flow stress with temperature is only slightly greater than the change in the elastic constants (fig. 2). This suggests that if the criterion for flow is breakdown of a boundary. the strength controlling factor is elastic interaction. In this case, a strong dependence of boundary strength on angle would be expected, and no such dependence has been observed. This, however, may be because the relation assumed between α and β is incorrect. The range of β is not large, and the range of α may very well be much less.

Fig. 3
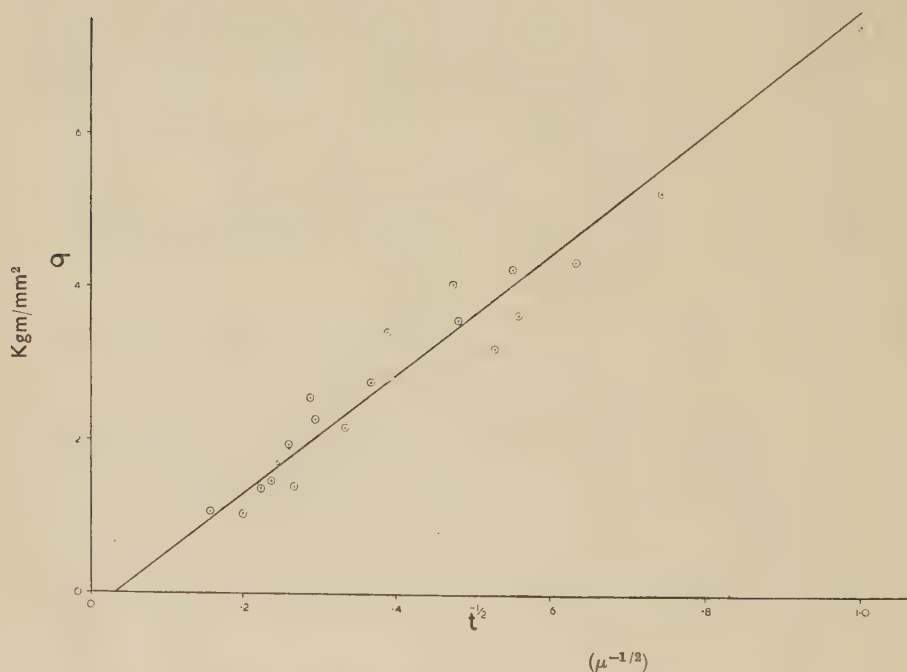
Tensile flow stress σ as a function of (subgrain size t)$^{-1/2}$.

An alternative explanation is that the leading dislocation of a pile up combines with the dislocations of the boundary. The greater the density of dislocations in the boundary, the smaller the length of combination of each with the leading dislocation of the pile up, giving a very much smaller dependence of strength on boundary angle than would be expected in the absence of combination. If the boundary contains dislocations of the correct slip system, the combinations may take the form of

Cottrell-Lomer locks. The mechanism of failure, however, would not be that considered by Stroh (1956), as the strength is not temperature dependent.

In any case, a dependence of strength on boundary angle would be expected for very low angle boundaries. This is being investigated.

The drop in the curve of fig. 2 for temperatures above 200°c requires some comment. 200°c is the temperature at which grain boundary slip begins to operate in aluminium (Ke 1947), and it seems probable that this is the explanation. Relaxation of shearing stresses across grain boundaries would lead to a stress redistribution, and it may be that the effective internal shearing stresses at the places where slip is occurring are just as high as at low temperatures, when allowance has been made for the change in shear modulus.

References

COTTRELL. A. H.. 1953, *Dislocations and Plastic Flow in Crystals* (Oxford).
COTTRELL, A. H., and STOKES, R. J., 1955, *Proc. roy. Soc.* A, **233,** 17.
FRANK, F. C., 1950, *Carnegie Inst. of Tech. Symposium on the Plastic Deformation of Crystalline Solids* (Pittsburg Report), p. 89, Office of Naval Research (NAVEXOS-P-834).
GAY, P., HIRSCH, P. B., and KELLY, A., 1953, *Acta Met.,* **1,** 315 ; 1954, *Acta cryst., Camb.,* **7,** 41.
HIRSCH, P. B., and KELLAR, J. N., 1952, *Acta cryst., Camb.,* **5,** 162.
KE, T. S., 1947, *Phys. Rev.,* **71,** 533.
KELLY, A., 1953, *Ph.D. Thesis,* Cambridge University ; 1954, *Acta cryst.,* **7,** 554.
KOSTER, W., 1948, *Z. Metallk.,* **39,** 1.
STROH, A. N., 1956, *Phil. Mag.,* **1,** 489.

An X-Ray Study of Neutron Irradiated Lithium Fluoride†

By R. E. Smallman and B. T. M. Willis

Metallurgy Division, A.E.R.E., Harwell, Nr. Didcot, England

Abstract

The nature of the damage in neutron irradiated lithium fluoride has been examined by x-rays up to neutron doses at which the majority of the ions have been displaced from their lattice sites. The observations have been made by Debye–Scherrer powder photography, Laue photography and small-angle scattering. The results indicate that isolated defects predominate at low doses, but that these cluster to form large defects at doses higher than about 10^{17} neutrons/cm².

With the exception of some small-angle scattering all the x-ray effects anneal out in the range 400°–500° c. This residual scattering is interpreted as that associated with gas bubbles.

§ 1. Introduction

The nature of the damage induced in lithium fluoride by reactor irradiation has been the subject of several recent x-ray investigations. The problem has doubtless owed its popularity to the simplicity of the un-irradiated structure and, more important, to the ease with which the structure can be damaged.

Binder and Sturm (1954) showed that for a dose of 6×10^{16} neutrons/cm² the lattice expansion as measured from the change of lattice parameter was equivalent to that determined from density measurements. This indicated that the expansion was due to the production of isolated Frenkel defects, an interpretation which was later supported by annealing experiments (Binder and Sturm 1955). Keating (1955) measured the integral breadths of the 001 reflections of crystals irradiated at rather higher doses, 2·1 and $7\cdot5 \times 10^{17}$ n/cm². He observed considerable line broadening, which he interpreted in terms of a model of flat clusters of defects in the (001) plane separated by uniformly stressed material. Finally Mayer (1955) has reported measurements by Perio of the variation of lattice parameter with dose, and Brooks (1956) has reported some x-ray results of Guinier. Both these sets of results will be referred to below.

In the present work new x-ray results are reported on lithium fluoride irradiated in the range 3×10^{16} to 7×10^{18} n/cm².

† Communicated by A. H. Cottrell, F.R.S.

§ 2. Irradiation Procedure

The standard samples were plates, $\frac{1}{2}$ mm thick, cleaved from larger single crystals obtained from Harshaw Chemical Co., U.S.A. These crystals were irradiated in the centre of BEPO, the graphite moderated reactor at Harwell, in a slow neutron flux of about 10^{12} n/cm²/sec and at a temperature of $55 \pm 15°$ c.

The doses were measured by determining the γ-activity of cobalt wire monitors placed with the samples. Owing to self-screening the mean dose received by a sample was less than the unscreened dose recorded by the monitor. Calculations based on the assumption of an infinite slab of $\frac{1}{2}$ mm thickness showed that the standard sample received a mean dose 80% of that recorded by the monitor. This correction has been applied to the dose figures quoted below. Self-screening also produced a variation of $\pm 3\%$ in the dose throughout a given sample; this variation is about half the error involved in estimating the relative doses.

§ 3. X-Ray Results

3.1. *Measurements of Lattice Parameter and Line Breadth*

Debye–Scherrer photographs were taken of powders, which were prepared from fragments cleaved from irradiated single crystals. The lattice parameter a was obtained from the line positions on the photographs. Figure 1 shows the variation of a with dose. For small doses the change of a, $\Delta a/a$, is proportional to dose ; at higher doses a increases to a maximum at 4×10^{17} n/cm² and then falls again. These results are in good agreement with those obtained by Perio (see Mayer 1955).

Fig. 1
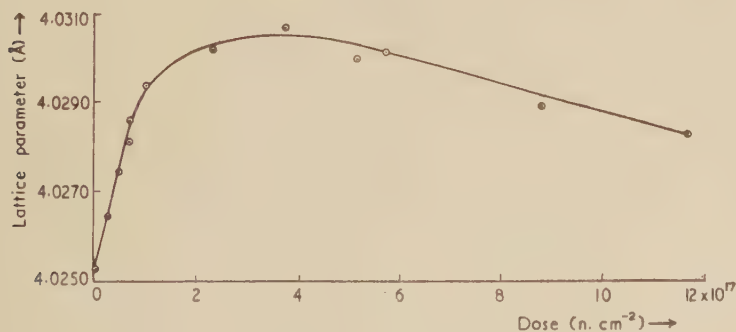
. Lattice parameter of LiF as a function of slow neutron dose.

The integral breadths β_{hkl} of the powder lines were measured from line profiles obtained by microdensitometry. The instrumental broadening was corrected by the Jones (1938) method, and it was assumed that the breadth of the unirradiated crystal was entirely instrumental. A plot of $\beta \cos \theta/\lambda$ *versus* $2 \sin \theta/\lambda$ for the most heavily irradiated sample

$(7\cdot2\times10^{18}$ n/cm^2) was a straight line of slope $0\cdot0042$ through the origin. This showed that the line broadening was predominantly due to strain rather than crystallite size, and that the mean strain was $0\cdot0042$.

The integral breadth of the $422\alpha_1$ line as a function of dose is shown in fig. 2. β_{422} is the same as the unirradiated value up to 1×10^{17} n/cm^2; above this β_{422} increases rapidly with dose and shows no sign of saturation.

Fig. 2
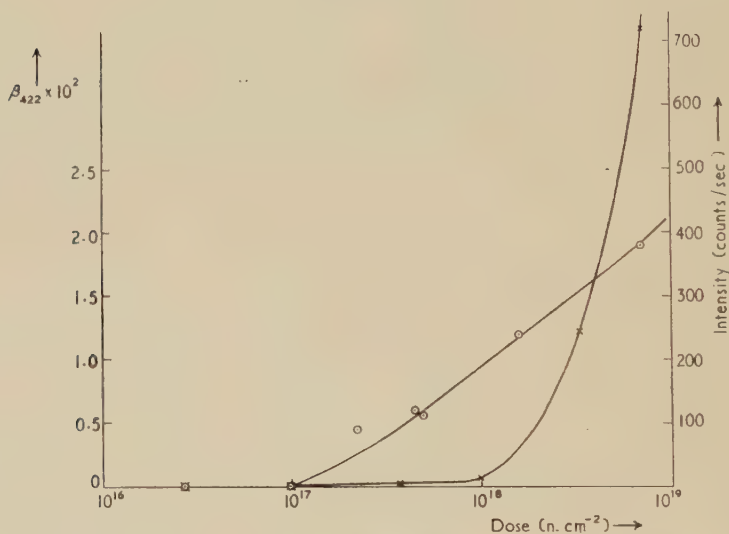
Integral breadth of $422\alpha_1$ line ○, and intensity of x-ray scattering at 1° ×, as a function of slow neutron dose.

3.2. *Laue Photographs*

Transmission 'Laue' photographs, using both white and mono-chromatic MoKα radiation, have been taken of a number of irradiated single crystals. In the heavily irradiated (i.e. greater than 10^{18} n/cm^2) samples narrow, well-defined streaks appear along the $\langle100\rangle$ directions. The streaks extend from the origin to the 200 reciprocal lattice points, and are produced by reflection of the characteristic MoKα radiation.

'Defect diffuse scattering' (Huang 1947), which arises from the dis-tortion of the lattice around the individual point defects, has been carefully looked for. This scattering is difficult to observe experimentally, as it is concentrated near the strong Bragg reflections and is in a region where the thermal diffuse scattering is a maximum. However, extra diffuse scattering has been observed along the radial direction joining the reciprocal lattice point to the origin. Such a radial distribution of intensity is predicted by the theory of defect diffuse scattering (Huang 1947, Cochran 1956).

3.3. *Small-angle X-Ray scattering*

The apparatus used for these tests was that described by Smallman and Westmacott (1957) for the study of cold work and irradiation effects in metals. It consisted essentially of an asymmetric quartz mono-chromator limited with slits to give $\frac{1}{2}°$ beam divergence. The sample to focus distance was 80 mm and the intensity of scattering recorded either on a film or directly using a Geiger counter.

A film taken with a crystal irradiated to 3×10^{18} n/cm² and oriented with the (100) and (001) planes respectively perpendicular and parallel to the x-ray beam, showed that the small angle scattering was approxi-mately isotropic. It was therefore possible to use a Geiger counter (Mullard type MX118 with slit 0·3 mm × 5 mm) to measure accurately the intensity distribution along the (100)–(001) zone. Figure 3 shows a plot of log (intensity) *versus* θ^2 (radians²) for six crystals irradiated with successively increasing doses of 5×10^{16}, $1·0 \times 10^{17}$, $1·0 \times 10^{18}$, $3·3 \times 10^{18}$ and 7×10^{18} n/cm². The results (corrected for parasitic scattering but not for beam height) have been plotted in this way since it is known (Guinier and Fournet 1955) that for a collection of identical scattering groups the intensity scattered over an angle θ is given by

$$I = Mn^2 I_e \exp(-4\pi^2 K^2 \theta^2 / 3\lambda^2). \quad \ldots \ldots \quad (1)$$

Here I_e is the intensity scattered by an electron at small angles, M is the number of groups, n represents the difference between the number of electrons in one group and in an equal volume of surrounding matrix, and K is the radius of gyration of the groups.

The amount of small angle scattering for irradiations less than 3×10^{17} n/cm² is extremely small but above this dose the scattering becomes appreciable. The intensity of scattering at 1° as a function of dose is shown in fig. 2 together with the line broadening results.

Accurate analysis of such a complex scattering system is difficult but an estimate of the maximum size of scattering region is of interest. The table shows the radius of gyration K for the various irradiated crystals calculated from the extreme low angle linear portion of the log I *versus* θ^2 curve.

Irradiation dose (n/cm²)	Size $K(\text{Å})$	Irradiation dose (n/cm²)	Size $K(\text{Å})$
5×10^{16}	10	1×10^{18}	23
1×10^{17}	15·5	$3·3 \times 10^{18}$	22
$3·7 \times 10^{17}$	18·5	7×10^{18}	22

It can be seen that the size of the scattering group increases with neutron dose up to about 10^{18} n/cm² and then remains approximately constant at 22 Å. The number of such regions also increases extremely rapidly with dose, as the intercept on the log I axis indicates.

Fig. 3
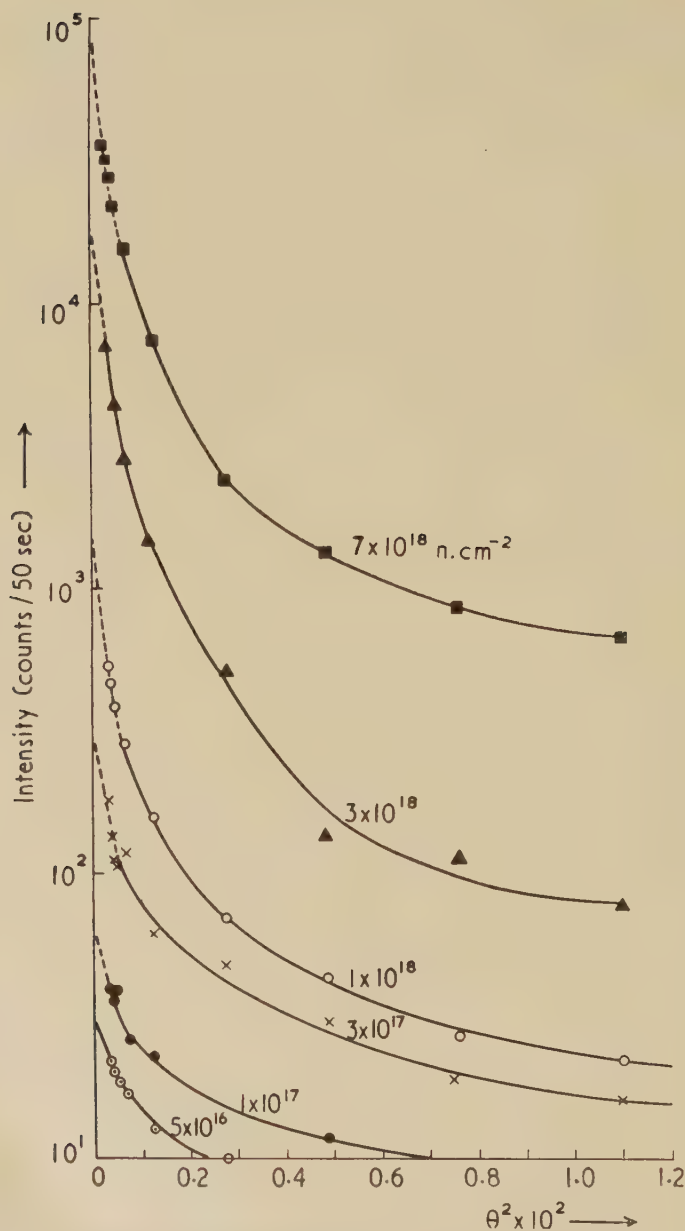
Log (intensity) *versus* θ^2 for six crystals irradiated at successively increasing doses.

3.4. *Annealing Experiments*

Irradiated single crystals have been vacuum annealed for 1 hr periods at 50° and 100° c intervals in the range from room temperature to 700° c. After each anneal the crystals were examined by the three x-ray techniques mentioned above. The bulk of the damage annealed out between 400°

and 500° c., i.e. the lattice parameter reverted to its original value, the powder lines became sharp and the Laue streaks disappeared. The small angle scattering results showed that the annealing behaviour of the scattering group was extremely complex. Below 400° c there is a small increase in small angle scattering but a large decrease does occur

Fig. 4
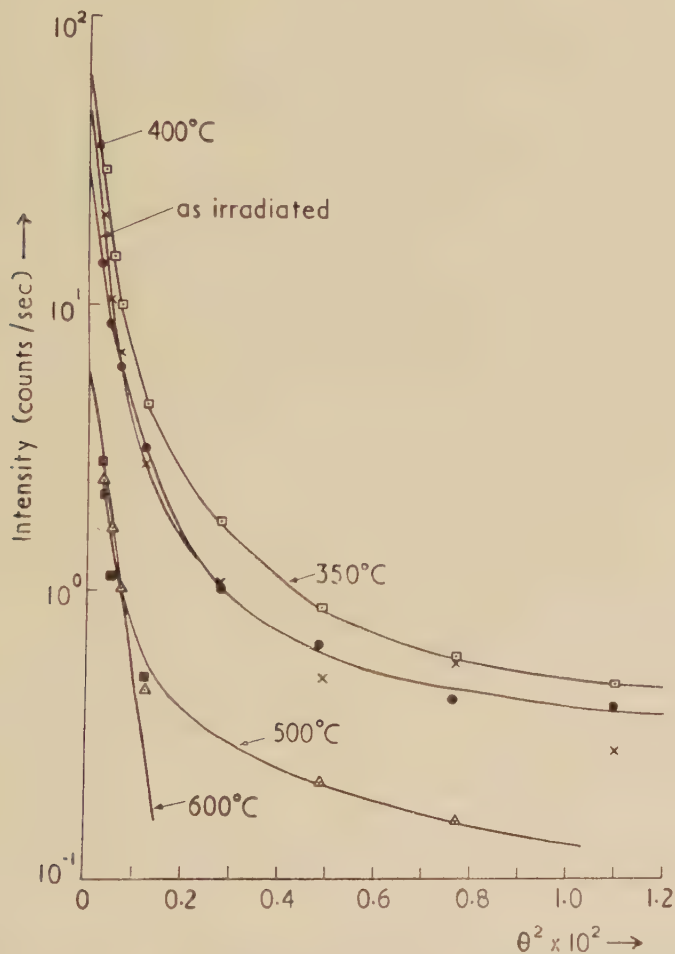
Log (intensity) *versus* θ^2 for crystal irradiated to 10^{18} n/cm^2 and annealed for one hour at successively increasing temperatures. ● As irradiated, ⊡ annealed at 350° c, × 400° c, △ 500° c, ■ 600° c.

in the range 400–500° c. Further annealing at temperatures above 500° c causes the log I *versus* θ^2 plot to become approximately linear but does not remove the scattering completely. The scattering curves for a crystal irradiated to 1×10^{18} n/cm^2 after various anneals are given in fig. 4. Substantial small angle scattering remains after high temperature annealing.

Irradiated lithium fluoride is dark red or black depending on the severity of the dose.   On annealing the colour of all the samples changed.   Crystals irradiated less than 10^{18} n/cm^2 become yellow-brown at low temperatures but finally colourless in the range 400–500° C.   The crystals more heavily irradiated remained dark up to 400–500° C, then became white.

§ 4. DISCUSSION

In the irradiation range below 10^{17} n/cm^2 the amount of small angle scattering and line broadening is extremely small whereas the lattice parameter increases linearly with dose.   This initial linear portion of the lattice parameter *versus* dose curve (fig. 1) can be interpreted as being mainly due to isolated Frenkel defects distributed at random throughout the lattice.   From the slope of this portion we can obtain, by assuming that the lattice expands by the molecular volume for each pair of Frenkel defects produced, an estimate of the number of defects per fission.   This number is fairly close to the theoretical estimate of 1900 obtained by assuming that all the defects remain in the lattice during and after the irradiation (Seitz and Koehler 1956).   We conclude therefore that the major part of the damage does not anneal out at room temperature.

We can interpret the saturation of the lattice parameter *versus* dose curve by using the rough criterion for saturation suggested by Pease (see Varley 1955).   An upper limit to the concentration of Frenkel defects is that for which any additional interstitial introduced in the lattice is adjacent to a vacant lattice site.   If the defects are immobile this will occur when the vacancy concentration is of the order of $1/N$, where N is the number of lattice sites surrounding an interstitial site. Now the cross section for thermal neutron absorption in LiF is 70 barns so that for the saturation dose of 3×10^{17} n/cm^2 a mole fraction $(70 \times 10^{-24})\,(3 \times 10^{17}) = 2 \cdot 1 \times 10^{-5}$ of fissions occurs.   The corresponding concentration of vacancies is $(2 \cdot 1 \times 10^{-5})\,(\frac{1}{2})\,(1900) = 1/50$.   This is rather less than $1/N$, but the difference can be accounted for by assuming interstitial-vacancy interactions over a few ionic distances.

We attribute the fall of the lattice parameter *versus* neutron dose curve to the coagulation of point defects.   Evidence for coagulation is provided by the appearance of $\langle 100 \rangle$ streaks in Laue photographs and by small angle scattering.   The streaks indicate a break-up of the periodicity in the $\langle 100 \rangle$ directions, as produced, for example, by the condensation of interstitial atoms in (100) planes.   The small angle scatter curves show that the scattering system is more complex, being more sensitive to vacancy groups than interstitial aggregates.   However it is expected that aggregates of lithium and fluorine atoms, together with groups of vacancies are present.   Any variation in size of each of these scattering groups will give rise to a concave type of log (intensity) *versus* θ^2 curve, as observed.   Coagulation of defects also produces long range strain, as revealed by the line broadening measurements.   The interpretation

of line broadening in terms of crystallite size is invalid (see § 3), although Varley (1956) reports that Pease has deduced thereby an estimate of the size of the region disordered by a single fission process.

On annealing, the Laue streaks, line broadening and changes in lattice parameter all completely disappear in the temperature range 400–$500°$ C. However, some small angle scattering still remains even at $700°$ C. This residual scattering is believed to be due to the new atoms, ^3H and ^4He, formed by transmutation. The number of such atoms per group can be calculated from the x-ray measurements, since from eqn. (1) the number of scattering particles M is given by

$$M = NI(O)/n^2, \qquad \ldots \ldots \ldots \quad (2)$$

where $I(O)$ is the intercept intensity in electrons per atom and N is the number of atoms/cm³. The conversion of the intensity from counts/sec. to electrons/atom can be made. knowing the geometry of the apparatus and the main beam intensity (Smallman and Westmacott 1957). For our arrangement one count/sec. is equivalent to 20 electrons/atom. Thus in the 1×10^{18} n/cm² and high temperature annealed sample the number of groups is about 4×10^{15}/cm³. However, the number of transmuted atoms formed during irradiation is 8×10^{18}/cm³ so that the number of atoms per group is about 2000. If these small atoms fit interstitially in the lattice sites $(\frac{1}{2}, \frac{1}{2}, \frac{1}{2})$ or $(\frac{1}{2}, 0, 0)$ then the volume occupied is about 500 unit cells. This is not in agreement with the observed size of the scattering group of 30 Å radius. The difference can be accounted for if it is assumed that gas atoms by capturing vacancies in their neighbourhood expand into gas bubbles forming a stable cavity. Such behaviour has been observed metallographically when irradiated uranium (Cottrell 1956) and beryllium (Barnes and Redding, private communication) is heated. An estimate of the size of cavity which this group of atoms would acquire at temperature $T°$K may be obtained since the pressure of a gas bubble of radius R is given by

$$P = 2\gamma/R \quad \ldots \ldots \ldots \ldots \quad (3)$$

where γ is the surface energy of the lithium fluoride. Since the volume of gas atoms at n.t.p. is

$$A_G/\rho_G N \quad \ldots \ldots \ldots \ldots \quad (4)$$

where ρ_G is the density of the gas at n.t.p. and A_G the atomic weight of the gas and N Avrogadro's number. the number of gas atoms per bubble at pressure P and temperature $T°$K is given by

$$4\pi R^3 \rho_G N P . 273/3 A_G T. \qquad \ldots \ldots \ldots \quad (5)$$

Taking the number of atoms per bubble as that given above (2×10^3) and with $\gamma = 200$ ergs/cm² and $\rho_G A_G = 4.5 \times 10^{-3}$ g/cm³ the size of the bubble is about 30 Å radius, in agreement with that observed at $600°$ C.

§ 5. Conclusions

Three principal x-ray techniques, Debye–Scherrer powder photography, Laue photography, small angle scattering, have been used to determine the effect of neutron irradiation on crystals of lithium fluoride. The results indicate that for low doses ($< 10^{17}$ n/cm^2) the defects are predominantly isolated. However at doses higher than about 10^{17} n/cm^2 clusters of defects such as interstial platelets in (100) planes and groups of vacancies are formed. These defects anneal out in the temperature range 400°–500° c but above this temperature it is believed that the transmuted atoms ^{3}H and ^{4}He which remain form small gas bubbles.

Note added in proof.—The presence of gas pockets has been confirmed by microscopic examination of samples annealed for long periods just below the melting point. For example, bubbles six microns in size and of *square* cross section were observed after heating for 24 hours at 700° c.

References

Binder, D., and Sturm, W. J., 1954, *Phys. Rev.*, **96**, 1519; 1955, *Ibid.*, **99**, 603.
Brookes, H., 1956, *Annual Review of Nuclear Science*, 215.
Cochran, W., 1956, *Acta cryst., Camb.*, **9**, 994.
Cottrell, A. H., 1956, *Metallurg. Rev.*, **1**, 479.
Guinier, A., and Fournet, G., 1955, *Small-angle scattering of X-rays* (London: Chapman and Hall).
Huang, K., 1947, *Proc. roy. Soc.*, **190**, 102.
Jones, F. W., 1938, *Proc. roy. Soc.*, **166**, 16.
Keating, D. J., 1955, *Phys. Rev.*, **97**, 832.
Mayer, G., 1955, *International Conference on Peaceful Uses of Atomic Energy*, **7**, 686.
Seitz, F., and Koehler, J. S., 1956, *Solid State Physics*, **2**, 443.
Smallman, R. E., and Westmacott, K. H., 1957 (to be published).
Varley, J. H. O., 1955, *International Conference on Peaceful Uses of Atomic Energy*, **7**, 644; 1956, *Progr. nucl. Energy*, **1**, 672.

Theory of Rochelle Salt†

By A. F. Devonshire

H. H. Wills Physical Laboratory, Royal Fort, Bristol

Summary

Mason's theory of Rochelle salt is critically examined in relation to Bancroft's high-pressure measurements of the dielectric constant. It is shown that, though the theory as it stands cannot explain the results, it can be made to do so fairly well by a slight modification. The theory, however, requires the effective dipole moment to vary with volume in an unexpected way, and no satisfactory explanation has been found for this.

---

§ 1. Introduction

ROCHELLE SALT was the substance that was first shown to be ferroelectric. In recent years many other ferroelectrics have been discovered, but Rochelle salt has properties not possessed by any of the others. The most striking of these properties is the existence of two Curie temperatures. It is true that many other ferroelectrics have two or more transition temperatures, but each transition is always to a new crystal symmetry ; it is only in Rochelle salt that the symmetry‡ below the lower transition temperature is the same as above the upper transition temperature. This property alone would make it of special interest to develop a theory for Rochelle salt, but in addition we are able to check a theory more closely for Rochelle salt than for any other ferroelectric. This is for the following reason. Measurements of the dielectric constant have been made by Bancroft (1938) for various pressures up to 10 000 atmospheres. These measurements not only give us the dielectric constant as a function of pressure and temperature, and hence of specific volume and temperature, but also give the transition temperatures as functions of pressure or specific volume. They show, incidentally, that there are two transition temperatures under conditions of constant volume as well as constant pressure, and also that if the substance is kept at constant temperature and the pressure varied there may be two transition pressures.

The dielectric properties of Rochelle salt have been very fully discussed in a phenomenological way by Mueller (1940), but he did not attempt to relate them to the atomic structure except in so far as it determined the crystal symmetry. The most successful atomic model is that suggested

---

† Communicated by the Author.
‡ This does not necessarily imply that the structure of the unit cell is exactly the same.

by Mason (1947, 1950). He was able to account for the existence of two Curie temperatures at normal pressure, but did not investigate whether the model gave two Curie temperatures at constant volume as Bancroft's results show that it should. We have therefore examined the model in some detail ; we find that, in the exact form that Mason gave it, it does not give two Curie temperatures at constant volume, but that by a slight modification can be made to do so. With this modification we find that we can explain Bancroft's results fairly well, but that some difficulties still remain.

§ 2. Experimental Observations

If the dielectric constant of Rochelle salt is measured at normal pressure as a function of temperature it shows two sharp maxima at about $-16°c$ and $24°c$. In between these temperatures the substance shows hysteresis and other properties characteristic of a spontaneously polarized body. The spontaneous polarization has been measured ; its maximum value is about $2·5 \times 10^{-7}$ coul/cm², and it tends to zero at the two transition temperatures. The transitions are accompanied by changes in crystal

Fig. 1
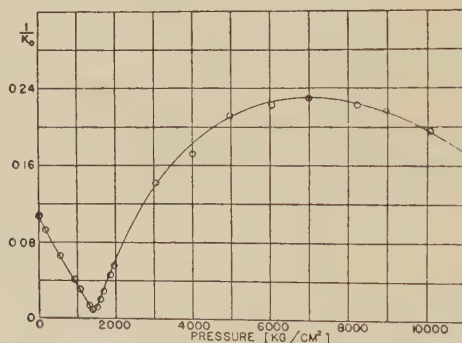
The reciprocal susceptibility of Rochelle salt as a function of pressure at $40°c$
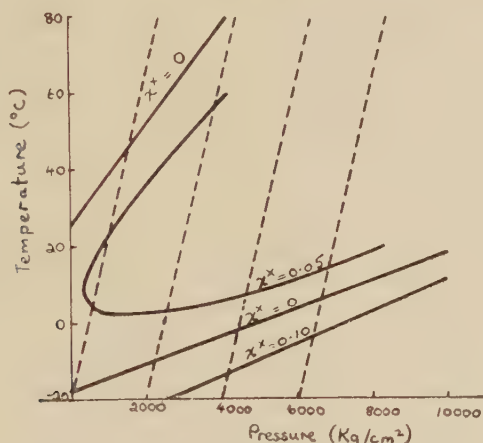(Bancroft 1938).

form ; when spontaneously polarized the crystal has monoclinic symmetry (class C_2), and otherwise is orthorhombic (class D_2). The transitions appear to be second order ones. Anomalies also occur in some of the piezoelectric constants at the transitions, but it has been shown by Mueller that these are the natural consequences of the anomalies in the dielectric constants.

Bancroft (1938) has made measurements of the dielectric constant at various pressures up to 10 000 atmospheres and for temperatures from $-20°c$ to $60°c$. In fig. 1 we show his values of the reciprocal susceptibility plotted as a function of pressure at $40°c$. The reciprocal susceptibility at constant stress along the x-axis (the axis of spontaneous polarization in Rochelle salt) is defined by the equation

$$\chi_{11}{}^X = \left(\frac{\partial E_1}{\partial P_1}\right)_X , \qquad \cdots \cdots \quad (2.1)$$

where X denotes the stress. At a second-order transition χ_{11}^{X} will vanish and the corresponding dielectric constant will become infinite. The figure shows that there is a transition at about 1400 atmospheres and the trend of the curve suggests that there will be a further transition at sufficiently high pressures. Bancroft made similar sets of measurements at other temperatures, but his results are best shown by drawing contours of constant χ_{11}^{X} on a pressure–temperature diagram. This is done in fig. 2, and on the same diagram are drawn lines of constant volume. This diagram shows clearly that two transitions take place under conditions of constant volume as well as constant pressure, and that the temperature range of the spontaneously polarized state increases as the pressure increases. The values of reciprocal susceptibility plotted in fig. 2 all refer to a state of zero polarization. In the spontaneously

Fig. 2

Contours of constant reciprocal susceptibility on a pressure–temperature diagram (Bancroft 1938).

polarized state, however, Bancroft's measurements refer, of course, to crystals with the stable spontaneous polarization. The values for zero polarization can be deduced as follows. At a given temperature and pressure the free energy can be expanded in even powers of P according to the equation

$$G = G_0 + \tfrac{1}{2}\chi_{11}^{X}P_1^{2} + BP_1^{4}, \qquad \cdots \cdots \quad (2.2)$$

where higher powers of P_1 can be neglected if P_1 is small. The electric field E is given by

$$E_1 = \frac{\partial G}{\partial P_1} = \chi_{11}^{X}P_1 + 4BP_1^{3}, \qquad \cdots \cdots \quad (2.3)$$

and the reciprocal susceptibility by

$$\frac{\partial E_1}{\partial P_1} = \chi_{11}^{X} + 12B\dot{P}_1^{2}. \qquad \cdots \cdots \quad (2.4)$$

A spontaneously polarized state occurs when $\chi_{11}{}^X$ is negative. Then if the field is zero we have

$$0 = \chi_{11}{}^X P_1 + 4B P_1{}^3,$$

and hence P_1 is zero or

$$P_1{}^2 = -\chi_{11}{}^X/4B.$$

It can easily be shown that the last solution is the stable one and if we substitute in (2.4), we have

$$\frac{\partial E_1}{\partial P_1} = -2\chi_{11}{}^X,$$

that is

$$\chi_{11}{}^X = -\tfrac{1}{2}\frac{\partial E_1}{\partial P_1}. \qquad \cdot \quad \cdot \quad \cdot \quad \cdot \quad \cdot \quad \cdot \quad \cdot \quad (2.5)$$

Thus we have the value of $\chi_{11}{}^X$ in terms of the reciprocal susceptibility for the spontaneously polarized state. This equation was used in plotting the contours in fig. 2.

When we consider the properties of an atomic model it is convenient to take the polarization and linear dimensions of the model as variables, so that the most directly derived quantity is the reciprocal susceptibility at constant strain $\chi_{11}{}^x$. This is related to $\chi_{11}{}^X$ by the formula (Devonshire 1954, eqns. (2.4))

$$\chi_{11}{}^x = \chi_{11}{}^X + b_{14}{}^2 c_{44}{}^P. \qquad \cdot \quad \cdot \quad \cdot \quad \cdot \quad \cdot \quad (2.6)$$

In this equation b_{14} is the piezoelectric constant that gives the ratio of shear strain in the yz plane to polarization in the x-direction, and $c_{44}{}^P$ is the ordinary shear elastic constant measured at constant polarization. The quantities b_{14} and $c_{44}{}^P$ have no anomalies at the transitions and do not vary much over the temperature range we are interested in; they can be determined by piezoelectric measurements (Mueller 1940). Alternatively they can be determined directly by making measurements at such high frequencies that the piezoelectric response does not take place and then compared with $\chi_{11}{}^X$ (Mason 1947). In either case we find that

$$\chi_{11}{}^x - \chi_{11}{}^X \simeq 0.04, \qquad \cdot \quad \cdot \quad \cdot \quad \cdot \quad \cdot \quad (2.7)$$

and only varies slightly with temperature (Devonshire 1954, p. 97). It is not known how this quantity varies with pressure, but probably this variation is not large. Since the vanishing of $\chi_{11}{}^x$ is the condition for a second-order transition under conditions of constant strain instead of the normal conditions of constant stress, and $\chi_{11}{}^x$ is always larger than $\chi_{11}{}^X$, it follows that if the crystal could be clamped so as to prevent spontaneous strain then the range of the spontaneously polarized state would be reduced. In fact the range of the spontaneously polarized state of the 'clamped' crystal on the pressure–temperature diagram will be that within the contour $\chi_{11}{}^X = -0.04$. This means that at zero pressure the temperature range of the spontaneously polarized state will be just about reduced to zero, though at higher pressures there will be

still a finite range. This was first pointed out by Mueller (1940). It does not seem possible to test this prediction directly ; for although the crystal can be clamped in such a way as to prevent the strain that accompanies induced polarization this will not affect the spontaneous polarization ; the reason is that the spontaneous polarization normally takes place in domains arranged in such a way that the net strain over the whole crystal is small.

§ 3. MASON'S THEORY

Mason's theory of Rochelle salt was based on the crystal structure as determined by Beevers and Hughes (1941). The x-rays did not show the positions of the hydrogen atoms, but the positions of the oxygen atoms appeared to indicate that some of the hydrogen atoms could migrate between two positions of equilibrium as shown in fig. 3 ; the figure is

Fig. 3

asymmetrical because the atoms have different binding energy in the two positions. A movement of a hydrogen atom from one position to another will change the electric moment of the cell, and the system may be considered as a dipole that can reverse its sign, and has a different energy for the positive and negative orientations. The movable hydrogen atoms occur in pairs in the unit cell with opposite orientations, so that when both are in their positions of lowest energy there is no net dipole moment. So far we have only considered the isolated unit cell. When the substance is polarized, however, there will be an electrical interaction between the dipoles in different cells, which will lower the energy. At very low temperatures the atoms will arrange themselves so as to make the total energy a minimum. This arrangement may be either the ' antipolar ' state in which each hydrogen atom is in its position of lowest energy, so that half the dipoles point each way and there is no polarization—or the polar state in which all the dipoles point the same way ; it depends on whether the lowering of energy due to the interaction of the dipoles is sufficient to compensate for the increase of energy due

to half the hydrogen atoms being in the higher energy state. At high temperatures the atoms will be more or less randomly arranged, as this state has the largest entropy. If conditions were such that the substance passed successively through the antipolar, polar and non-polar random states, then the existence of two transition temperatures would be satisfactorily accounted for.

Recent work on the structure of Rochelle salt by neutron-diffraction by Frazer *et al.* (1954) has shown that the structure determined by Beevers and Hughes was not quite correct. The particular hydrogen atoms that were supposed to move clearly could not do so. They showed, however, that certain others had two possible positions of equilibrium. Thus the essential features of Mason's model are not altered. His calculations of energy barriers, dipole moments, etc., have no significance now ; however, in this paper we are not concerned with these details, but only with the general features of the model, and whether it can give the double transition observed in Rochelle salt. The model may be applicable to other substances.

The movement of the hydrogen atoms is not, of course, the only source of polarizability in the material. There is also the electronic polarizability, but we shall see later that this does not affect the main conclusions, so for the moment we shall not take it into account.

Let there be N dipoles per unit volume of each group of fixed moments $\pm\mu$, and let the difference in energy between the two dipole positions be $2\varDelta$. At any time let $\frac{1}{2}N(1+x_1)$ of the first group and $\frac{1}{2}N(1+x_2)$ of the second group point in the positive direction. Then the polarization P will be given by

$$P=N\mu(x_1+x_2), \qquad \ldots \ldots \quad (3.1)$$

and the dipole interaction energy will be $-\frac{1}{2}\gamma P^2$, where γ is a constant depending on the configuration of the dipoles. If the dipoles of the first group have their minimum energy when pointing in the positive direction then the energy of the system per unit volume (referred to the antipolar state as zero) is given by

$$U=-\tfrac{1}{2}\gamma N^2\mu^2(x_1+x_2)^2+N\varDelta(2+x_2-x_1). \qquad \ldots \quad (3.2)$$

The entropy of the system is given by the usual formula in terms of the number of configurations

$$
\begin{aligned}
S=k\log&\frac{N!}{\tfrac{1}{2}N(1+x_1)!\,\tfrac{1}{2}N(1-x_1)!}+k\log\frac{N!}{\tfrac{1}{2}N(1+x_2)!\,\tfrac{1}{2}N(1-x_2)!}\\
=-kN\{&(1+x_1)\log(1+x_1)+(1-x_1)\log(1-x_1)+(1+x_2)\log(1+x_2)\\
&+(1-x_2)\log(1-x_2)-4\log 2\}, \qquad . \quad . \quad (3.3)
\end{aligned}
$$

and since the Helmholtz free energy A is $U-TS$ this is given by

$$
\begin{aligned}
A/NkT=-\tfrac{1}{2}\alpha(x_1+x_2)^2&+\beta(2+x_2-x_1)\\
+\tfrac{1}{2}\{(1+x_1)\log(1+x_1)&+(1-x_1)\log(1-x_1)+(1+x_2)\log(1+x_2)\\
&+(1-x_2)\log(1-x_2)-4\log 2\}, \qquad . \quad (3.4)
\end{aligned}
$$

where
$$\alpha=\gamma N\mu^2/kT, \qquad \beta=\varDelta/kT, \qquad , \quad , \quad , \quad . \quad (3.5)$$

At equilibrium A is a minimum with respect to both x_1 and x_2 and hence

$$0 = -\alpha(x_1 + x_2) - \beta + \tfrac{1}{2} \log \frac{1 + x_1}{1 - x_1},$$

$$= -\alpha(x_1 + x_2) + \beta + \tfrac{1}{2} \log \frac{1 + x_2}{1 - x_2},$$

so that

$$\left. \begin{array}{l} x_1 = \tanh\{\alpha(x_1 + x_2) + \beta\}, \\ x_2 = \tanh\{\alpha(x_1 + x_2) - \beta\}, \end{array} \right\} \qquad \cdots \cdots \quad (3.6)$$

and therefore

$$x_1 + x_2 = \tanh\{\alpha(x_1 + x_2) + \beta\} + \tanh\{\alpha(x_1 + x_2) - \beta\}$$

$$= \frac{2 \sinh 2\alpha \,(x_1 + x_2)}{\cosh 2\alpha(x_1 + x_2) + \cosh 2\beta}. \qquad \cdots \cdots \quad (3.7)$$

If we plot the right-hand side of eqn. (3.7) as a function of $x_1 + x_2$ it takes two forms according to whether $\cosh 2\beta$ is less than or greater than 2, as shown in fig. 4. In the first case there will be a solution other than zero if the slope at the origin is greater than 1. This will be so if

$$1 < \frac{4\alpha}{1 + \cosh 2\beta}. \qquad \cdots \cdots \quad (3.8)$$

Fig. 4

(a) $\qquad\qquad\qquad\qquad$ (b)
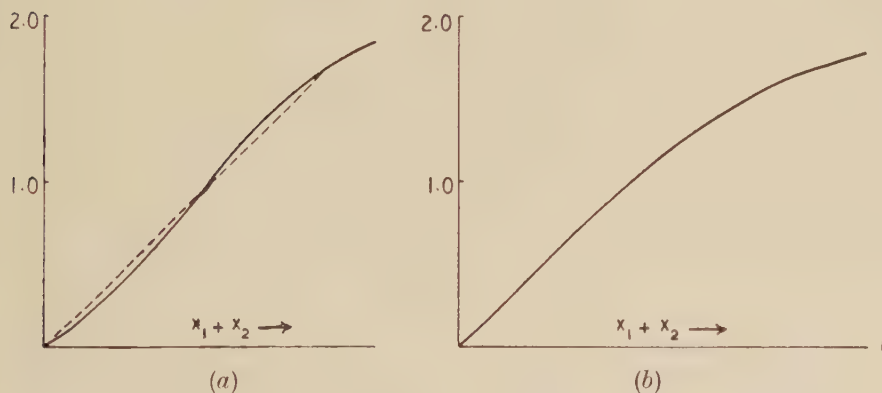
The transition temperature will be given by

$$4\alpha = 1 + \cosh 2\beta, \qquad \cdots \cdots \quad (3.9)$$

and the transition will be a second order one. In the second case the transition will be a first order one and will take place when a line through the origin with unit slope cuts off equal areas.

We have now to consider whether eqn. (3.7) can have two solutions for different temperatures. If the volume is kept constant as the temperature changes it seems reasonable to assume that the quantities Δ and $\gamma N \mu^2$ do not change. We can therefore write

$$\beta = \theta \alpha, \qquad \cdots \cdots \quad (3.10)$$

where

$$\theta = \Delta / \gamma N \mu^2, \qquad \cdots \cdots \quad (3.11)$$

and so is independent of temperature. Now at the absolute zero the substance will be either in the completely ordered polar state ($x_1 = x_2 = 1$), or in the completely ordered antipolar state ($x_1 = -x_2 = 1$). In the first case the free energy is $-2\alpha + 2\beta$; in the latter case it is 0. Thus if the antipolar state is to be the stable one at low temperatures we must have $\theta > 1$. If this is so, however, can we easily show that eqn. (3.9) has no solution, so that no second-order transition to a polar state is possible. It can also be shown that no first-order transition is possible.

Thus Mason's model as it stands does not give two transition temperatures at constant volume. We shall now show, however, that with a slight modification it will do so. An obvious modification to the simple model we have been using is to assume that the two states of the hydrogen atom have different weights. Classically this corresponds to the fact that the atom may have different vibration frequencies in its two equilibrium positions. One would expect it to have a lower frequency in the position with the higher energy, so that this state should have the greater weight.

Let us suppose that the higher energy state has a greater weight by a factor ϖ (it is clearly only the ratio of the weights of the two states that matters). Then the energy of the system will be unaltered, but the entropy will be increased by an amount $\frac{1}{2}Nk(2+x_1-x_2)\log\varpi$. Equation (3.4) for the free energy retains the same form, but instead of (3.5) we have

$$\alpha = \frac{\gamma N\mu^2}{kT},$$

$$\beta = \frac{\Delta}{kT} - \tfrac{1}{2}\log\varpi,$$

$$= \theta\alpha - \phi, \qquad \dots \dots \dots (3.12)$$

where, as before

$$\theta = \Delta/\gamma N\mu^2,$$

$$\phi = \tfrac{1}{2}\log\varpi. \qquad \dots \dots \dots (3.13)$$

Equation (3.9) now becomes

$$4\alpha = 1 + \cosh 2(\theta\alpha - \phi). \qquad \dots \dots \dots (3.14)$$

Unless ϕ is very small this equation in α will, in general, have two solutions for suitable values of θ. In fig. 5 we show θ plotted against $1/\alpha$. Since $1/\alpha$ is proportional to T this figure shows that in a suitable range of θ we have two transition temperatures, and that the upper one is always a second-order transition, but the lower one may be first or second order according to the value of θ.

We must now consider the effect of the electronic polarization, which we have neglected so far. If we denote this by P_e there will be two additional terms in the energy and hence in the free energy, namely

$$\tfrac{1}{2}aP_e^2 - bP_eN\mu(x_1+x_2). \qquad \dots \dots \dots (3.15)$$

The second term represents the interaction energy between the electronic polarization and the dipole polarization. The first term is the net energy

required to produce the electronic polarization; the constant in the term can be determined in terms of the refractive index, which depends on the electron polarizability alone. Since A has to be a minimum with respect to P_e as well as to x_1 and x_2 we have an additional equation, namely
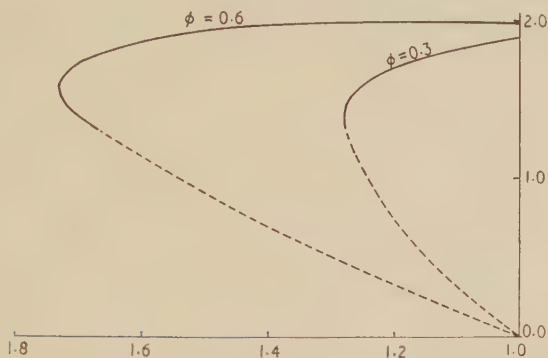
$$0 = aP_e - bN\mu(x_1 + x_2), \qquad \ldots \quad (3.16)$$

and if we substitute for P_e in the expression (3.15) then the additional term in the free energy becomes

$$-\tfrac{1}{2}(b^2/a)N^2\mu^2(x_1 + x_2)^2.$$

Thus comparing it with (3.2) we see that the sole effect of the electronic polarization is to replace γ by γ' where $\gamma' = \gamma + (b^2/a)$.

Fig. 5

Curves at which a transition takes place. The full lines indicate a second order transition and the dotted lines a first order one.

Let us now consider the dielectric susceptibility. We have

$$E = \frac{\partial A}{\partial P_e} = \frac{1}{N\mu}\frac{\partial A}{\partial x_1} = \frac{1}{N\mu}\frac{\partial A}{\partial x_2},$$

and hence

$$E = aP_e - bN\mu(x_1 + x_2) \qquad \ldots \qquad (3.17\,a)$$

$$= -bP_e + \frac{kT}{\mu}\left\{-\alpha(x_1 + x_2) - \beta + \tfrac{1}{2}\log\frac{1+x_1}{1-x_1}\right\} \qquad (3.17\,b)$$

$$= -bP_e + \frac{kT}{\mu}\left\{-\alpha(x_1 + x_2) - \beta + \tfrac{1}{2}\log\frac{1+x_2}{1-x_2}\right\} \qquad (3.17\,c)$$

from (3.4) and (3.15). The total polarization P is given by

$$P = P_e + N\mu(x_1 + x_2). \qquad \ldots \qquad (3.18)$$

From (3.17 b) and (3.17 c) we have

$$x_1 = \tanh\left\{\frac{\mu}{kT}(E + bP_e) + \alpha(x_1 + x_2) + \beta\right\},$$

$$x_2 = \tanh\left\{\frac{\mu}{kT}(E + bP_e) + \alpha(x_1 + x_2) - \beta\right\},$$

and hence

$$x_1+x_2=\tanh\left\{\frac{\mu}{kT}(E+bP_e)+\alpha(x_1+x_2)+\beta\right\}$$

$$+\tanh\left\{\frac{\mu}{kT}(E+bP_e)+\alpha(x_1+x_2)-\beta\right\}$$

$$=\frac{2\sin 2\{\mu/kT(E+bP_e)+\alpha(x_1+x_2)\}}{\cosh 2\{\mu/kT(E+bP_e)+\alpha(x_1+x_2)\}+\cosh 2\beta}. \quad . \quad . \quad . \quad (3.19)$$

From (3.17 a), (3.18) and (3.19) we can determine E in terms of P, and hence find the dielectric constant. If we substitute from (3.17 a) and (3.18) in (3.19) we find that

$$\frac{aP-E}{(a+b)N\mu}=\frac{2\sinh\dfrac{2\mu}{kT(a+b)}\left\{(a+2b)E+b^2P+\dfrac{\alpha kT}{N^2}(aP-E)\right\}}{\cosh\dfrac{2\mu}{kT(a+b)}\left\{(a+2b)E+b^2P+\dfrac{\alpha kT}{N\mu^2}(aP-E)\right\}+\cosh 2\beta}.$$

If E and P are both small then we have

$$(1+\cosh 2\beta)(aP-E)=\frac{4N\mu^2}{kT}\{(a+2b)E+b^2\}+4\alpha(aP-E),$$

and hence

$$\frac{E}{P}=\frac{a\{1+\cosh 2\beta-4\alpha\}-(4N\mu^2/kT)\,b^2}{1+\cosh 2\beta-4\alpha+(4N^2/kT)\,(a+2b)}. \quad . \quad . \quad (3.20)$$

This can be further simplified if we are fairly near the transition temperatures. Here E/P will be small and we shall have approximately

$$a\{1+\cosh 2\beta-4\alpha\}\simeq 4N\mu^2/b^2kT.$$

This can be substituted in the denominator, and then we have

$$\frac{E}{P}=\frac{a^2}{(a+b)^2}\frac{kT}{4N\mu^2}\{1+\cosh 2\beta-4\alpha\}-\frac{ab^2}{(a+b)^2}. \quad . \quad . \quad (3.21)$$

If we substitute for α and β from (3.5) then we have

$$\frac{E}{P}=\frac{a^2}{(a+b)^2}\frac{kT}{4N\mu^2}(1+\cosh 2\beta)-\frac{a^2\gamma+ab^2}{(a+b)^2}, \quad . \quad . \quad (3.22)$$

where

$$\beta=\frac{\Delta}{kT}-\tfrac{1}{2}\log \varpi,$$

that is

$$\frac{E}{P}=\frac{a^2}{(a+b)^2}\left[\frac{kT}{4N\mu^2}\{1+\cosh 2\beta\}-\gamma'\right]$$

$$=\frac{a^2\gamma'}{(a+b)^2}\frac{1}{4\alpha'}[1+\cosh 2\beta-4\alpha'], \quad . \quad . \quad . \quad (3.23)$$

where

$$\alpha'=\gamma'N\mu^2/kT. \quad . \quad . \quad . \quad . \quad (3.24)$$

§ 4. Comparison with Experiment

We must now compare the predictions of the theory with the experimental results of Bancroft. The simplest comparison is that of the

transition temperatures. The theoretical calculations refer to transitions at constant volume ; but the experiments were made at constant pressure. The transitions at constant volume (if they are second order) occur when $\chi_{11}{}^x$ is zero and hence, from (2.7), when $\chi_{11}{}^X$ is -0.04. Thus the experimental contour of $\chi_{11}{}^X$ equal to -0.04 plotted in fig. 2 should correspond to the theoretical contour of the transition. Now the theoretical contour of the transition depends on three parameters $\gamma' N\mu^2/k$, $\varDelta/k$, ϕ, which we may reasonably assume to be functions of volume only. There are two transition temperatures for each volume ; thus if we knew one of the parameters as a function of volume we could determine the other two by a comparison of theoretical and experimental results. We find that the values of the other parameters are not sensitive to the value of ϕ, and this is unlikely to vary much with volume. We shall therefore arbitrarily take ϕ to be 0.6. We then find the following values for the other parameters as functions of volume (table 1). If we take a different value of ϕ, say 0.3, then we get the following set of values (table 2).

Table 1

volume (cm³/mole)	$\gamma' N\mu^2/k$	$\varDelta/k$
156·2	180°	311°
154·3	193°	332°

Table 2

volume (cm³/mole)	$\gamma' N\mu^2/k$	$\varDelta/k$
156·2	203°	260°
154·3	218°	277°

Thus in each case we get a similar variation with volume. Over the small range of variation considered it may be taken to be linear. We see that both parameters increase as the volume decreases. Now there is no particular *a priori* reason for predicting how $\varDelta$ should vary with the volume, but it seems surprising that $\gamma' N\mu^2$ should increase as the volume decreases. Of the factors involved N must, of course, increase, but the change is very small ; on the other hand μ must surely decrease as the two equilibrium positions of the hydrogen atom come closer together, and this will far outweigh the change in N. The increase in $\gamma' N\mu^2$ must presumably therefore be due to an increase in γ'. Now we have

$$\gamma' = \gamma + b^2/a. \qquad \qquad (4.1)$$

Of the two terms in γ', γ depends only on the arrangement of the dipoles, and there is no particular reason why it should change with volume. The same applies to b, which determines the interaction of the dipoles

and electronic polarization. The value of a determines the electronic polarizability and can, in fact, be calculated from the refractive index ; we should expect the electronic polarizability to increase somewhat as the volume is diminished, but not so much as to cause the observed change in the parameter. In fact we should expect the main change with volume to be in the parameter dipole moment μ, and this would be in the wrong direction.

We can also gain information concerning the constants in the equation by comparing the predicted polarization and dielectric constant with the experimental values. Now the dipole polarization is $N\mu(x_1+x_2)$, and to this must be added the electronic polarization P_e. The relation between them is given by (3.16). Thus the total polarization is given by

$$P = N\mu(x_1+x_2)(1+b/a). \qquad \ldots \ldots \quad (4.2)$$

Now the maximum value of the polarization at zero pressure is 740 e.s.u., and the corresponding calculated value of x_1+x_2 is 0·4. Hence we have

$$N\mu\{1+(b/a)\}=1850, \qquad \ldots \ldots \quad (4.3)$$

and N is $3\cdot81\times10^{21}$, so that

$$\mu(1+b/a)=0\cdot49\times10^{-18} \text{ e.s.u.} \qquad \ldots \ldots \quad (4.4)$$

The value of the dielectric susceptibility is given by eqn. (3.23). Now above and below the transition temperatures the reciprocal susceptibility is nearly a linear function of temperature, so the simplest quantity to compare is the slope of this. According to Bancroft we have at the upper critical temperature

$$\frac{\partial}{\partial T}\left(\frac{E}{P}\right)_p = 5\cdot6\times10^{-3},$$

$$\frac{\partial}{\partial p}\left(\frac{E}{P}\right)_T = -0\cdot061\times10^{-3} \text{ per kg/cm}^2.$$

The theoretical values will refer to rate of change at constant volume, but this can be deduced from the above values if we use the values given by Bancroft for thermal expansion and compressibility. From these we can deduce that

$$\left(\frac{\partial p}{\partial T}\right)_v = 23\cdot8 \text{ kg/cm}^2/\text{deg},$$

and hence that

$$\frac{\partial}{\partial v}\left(\frac{E}{P}\right)_v = (5\cdot6-1\cdot45)10^{-3}=4\cdot15\times10^{-3}, \qquad \ldots \quad (4.5)$$

and

$$T\frac{\partial}{\partial T}\left(\frac{E}{P}\right)_v = 1\cdot23. \qquad \ldots \ldots \quad (4.6)$$

We can calculate that at the upper critical temperature

$$T\frac{\partial}{\partial T}\left\{\frac{1}{4\alpha'}(1+\cosh 2\beta-4\alpha')\right\}=0\cdot15,$$

and hence from (3.23) we have

$$\frac{a^2\gamma'}{(a+b)^2} = 8,$$

or

$$\gamma' = 8\{1+(b/a)\}^2. \qquad \ldots \ldots \ldots \quad (4.7)$$

By combining the values given in table 1, however, with the values given in (4.3) and (4.4) we can deduce that

$$\gamma' = 27\{1+(b/a)\}^2. \qquad \ldots \ldots \ldots \quad (4.8)$$

Thus the values of our constants calculated from different experimental results are not entirely consistent.

The quantity a can be deduced from the refractive index, since it gives the reciprocal value of the electronic susceptibility, and this determines the refractive index. The refractive index is 1·49, and hence the corresponding dielectric constant is $(1·49)^2$, that is 2·22, and this is related to a by the formula

$$2·22 = 1 + 4\pi/a,$$

so that

$$a = 10·3.$$

The value of b can only be guessed ; it is the factor giving the interaction of two sets of dipoles, and if these were at random its value would be $4\pi/3$. These values of b and a would make γ' equal to 16 according to (4.7) or to 54 according to (4.8). The values of γ given by (4.1) would be only a little less. But γ is of the same nature as b, since it determines the interaction between the dipoles formed by shift of the hydrogen ions, and hence these values are rather high.

Thus we see that Mason's theory, when modified, can account fairly well for the observed facts, but there are still some difficulties. Some of these could be removed by further refinements. It seems difficult, however, to account in a reasonable way for the fact that the range of transition temperature increases with decreasing volume. As we have just seen this seems to imply an effective dipole moment that increases with decreasing volume, and this is difficult to explain.

REFERENCES

BANCROFT, D., 1938, *Phys. Rev.*, **53**, 587.

BEEVERS, L. A., and HUGHES, W., 1941, *Proc. roy. Soc.* A, **177**, 251.

DEVONSHIRE, A. F., 1954, *Advanc. Phys.*, **3**, 85.

FRAZER, B. C., MCKEORON, M., and PEPINSKY, R., 1954, *Phys. Rev.* **94**, 1435, also see review article by Shirane, G., Jona, F., Pepinsky, R., 1955, *Proc. Inst. Radio Engrs*, **43**, 1775.

MASON, W. P., 1947, *Phys. Rev.*, **72**, 854 : 1950, *Piezoelectric Crystals* (New York : van Nostrand).

MUELLER, H., 1940, *Phys. Rev.*, **57**, 829.

Radio Observations of the Lunar Atmosphere†

By B. Elsmore

Cavendish Laboratory, Cambridge

Abstract

On January 24, 1956 observations were made at a wavelength of 3·7 metres, of the lunar occultation of the Crab Nebula. A comparison of the time of obscuration of the nebula with the computed value enabled the refraction occurring in the lunar atmosphere to be estimated. An electron density at the moon's surface of about $10^3 \, cm^{-3}$ was derived for cases of both an atmosphere in hydrostatic equilibrium and for an atmosphere which is continuously escaping ; a figure which corresponds to a surface density of the lunar atmosphere about 2×10^{-13} of that of the earth's atmosphere at normal temperature and pressure.

§ 1. Introduction

Optical measurements have failed to detect an atmosphere surrounding the moon ; the most sensitive observation was that of Dollfus (1952), who, by measuring the polarization of the scattered light, showed that the density of the lunar atmosphere is less than 10^{-9} of the density of the terrestrial atmosphere at sea level. A density of 10^{-5} of the terrestrial atmosphere derived by Lispkij (1953), has been proved to be unacceptable by Öpik (1955).

It has been shown by Link (1956) that the density of the lunar atmosphere may be derived from measurements of refraction of radio waves at the sunlit limb of the moon, when a radio star is occulted. Preliminary results obtained from observations of the occultation of the large diameter radio source in the constellation of Gemini (Elsmore and Whitfield 1955), have indicated that the density is less than 10^{-12} of the density of the terrestrial atmosphere. This paper is concerned with deductions from the occultation of another radio source, the Crab Nebula, which was observed at Cambridge on January 24, 1956 (Costain, et al. 1956). In § 2 the radio observations are described and their interpretation, in terms of the electron density surrounding the moon, is discussed in § 3. In § 4 an attempt is made to deduce the density of the lunar atmosphere from the measured electron density.

---

† Communicated by the Author.

§ 2. The Radio Observations

The occultation of the Crab Nebula was observed at wavelengths of 7·9 and 3·7 metres. The measurements at 7·9 m were seriously affected by man-made interference and it was only possible to observe the immersion, when the source disappeared behind the moon. At a wavelength of 3·7 m accurate observations were made throughout the occultation, from which a curve was plotted of the observed intensity of radio noise from the nebula. As the diameter of the source at this wavelength is approximately 5′ of arc, the intensity, at immersion, decreased to zero in about 10 minutes, and was restored about an hour later at emersion, when the source reappeared at the opposite limb of the moon. Since the moon's centre passed near the centre of the source, different points on the nebula were covered and uncovered in the same sequence. The occultation curves obtained during emersion and immersion were therefore complementary and corresponding points on the curves were found to be separated by an interval of 59·6±0·26 minutes. The error represents the scatter of times derived from different parts of the occultation curve.

§ 3. Interpretation

The time of obscuration, in the absence of refraction, was calculated from elements of the occultation predicted using Bessel's method and was checked by interpolating topocentric coordinates, kindly provided by Dr. Sadler of the Nautical Almanac Office. The calculated time, 59·21 minutes, is 0·4±0·26 minutes less than the observed time.

Although the difference between the observed and calculated times represents a barely significant result, it will be assumed for the present to have a meaning in deriving a value for the electron density; the observations, in any case, provide a figure for the maximum permissible density, as will be shown later.

Two phenomena may contribute to this time difference; diffraction at the limbs of the moon (§ 3.1), and refraction in the lunar atmosphere (§ 3.2).

3.1. *Diffraction*

The departure from a straight edge, due to both the curvature of the moon's limb and the mountainous surface is small compared with the size of a Fresnel zone. It was further found, that for the present case of an extended source, the effect of Fresnel diffraction is negligible.

3.2. *Refraction*

On the sunlit side of the moon, it is likely that the atmosphere, which had been exposed to the sun's radiation continuously for 11 days, was ionized. The refractive index, μ, of an ionized gas is given by

$$1-\mu^2 = \frac{Ne^2}{\pi m f^2} = \frac{8\cdot1\times10^{-5}}{f^2}\,N$$

where N is the electron density and f is the frequency in Mc/s. Since $\mu \doteqdot 1$, we can write

$$1-\mu = \frac{4 \cdot 05 \times 10^{-5}}{f^2}\, N.$$

The angle of refraction α of the radio waves will depend upon N and its gradient and two different types of distribution will be considered. Firstly, an exponential variation of electron density, which would be established if the atmosphere were in hydrostatic equilibrium, and secondly, an inverse power law, which would occur if the atmosphere were continuously escaping from the lunar surface.

3.2.1. *Exponential variation of electron density*

On the assumption that the Chapman formula is applicable, Link (1956) has shown that the electron density at a height h above the moon's surface is given by

$$N = N_0 \exp\,(-h/2H)$$

where N_0 is the electron density at the surface, and H the scale height. For this distribution, the angle of refraction α, which is assumed to be small, has been calculated by Link to be

$$\alpha = (1-\mu)\sqrt{(\pi a/H)}$$

where a is the moon's radius. Substituting for $1-\mu$ from above

$$\alpha = \frac{4 \cdot 05 \times 10^{-5}}{f^2}\, N\, \sqrt{\left(\frac{\pi a}{H}\right)} = \alpha_0 \exp\left(-\frac{h}{2H}\right)$$

where α_0 is the angle of refraction for a ray grazing the moon's surface.

3.2.2. *Power law variation of electron density*

If the electron density at a height h is given by

$$N = N_0(h+1)^{-\gamma}$$

where h is measured in units of the moon's radius, and γ is a constant, the angle of refraction is

$$\alpha = \frac{4 \cdot 05 \times 10^{-5}}{f^2} \cdot \frac{2 N_0 \gamma}{(h+1)} \int_0^{\frac{1}{2}\pi} \sin^\gamma i\; di$$

where i is the angle of incidence of a ray entering a spherically stratified medium. If the mean vertical component of velocity of the ionized gases is equal to the velocity of escape, then $\gamma = 3/2$; but if the velocity is appreciably greater than the escape velocity, then $\gamma = 2$.

The angle of refraction of rays which graze the surface of the moon is given in the table for different values and distributions of electron density. Since the moon moved its own diameter, which subtended $32'$ arc at the earth, in 59 minutes, the observed increase in the time of obscuration corresponds to $\alpha_0 = 13 \cdot 4'' \pm 8 \cdot 7''$ of arc, if it is assumed that refraction occurred only at the sunlit limb, and half this value if it occurred equally at both limbs. It can be seen that the electron density

lies in the range 10^3 to 10^4 cm^{-2} for $\gamma=3/2$, $\gamma=2$ or for scale heights in the region 5000 km to 80 km. If the scale height lies in the region 80 km to 20 km, the electron density is about 10^3 cm^{-2}; under these circumstances the extent of the refracting region necessary to produce the observed increase in the time of obscuration determines the lower limit of the scale height.

Table giving the Angles of Refraction, α_0 for a Grazing Ray

	Electron density at surface $(=N_0$ electrons cm$^{-2})$		
	10^5	10^4	10^3
$H=5000$ km	2′ 12″	13·2″	1·3″
$H=\ \ 500$ km	6′ 55″	41·5″	4·2″
$H=\ \ 100$ km	15′ 30″	1′ 33″	9·3″
$H=\ \ \ \ 50$ km	34′ 40″	3′ 28″	20·8″
$\gamma=3/2$	4′ 23″	26·3″	2·6″
$\gamma=2$	6′ 36″	39·6″	4·0″

§ 4. Discussion

The observations provide a measure of the electron density near the moon's surface, in excess of that of the surrounding medium. Before relating these data to the two types of atmosphere it is necessary to consider the possibility of the density being increased on one side of the moon, due to its motion through the interplanetary matter. Observations of the zodiacal light (Siedentopf *et al.* 1953) and of ' Whistler ' atmospherics (Storey 1953) have indicated that the electron density near the earth is approximately 600 cm^{-3}, hence the orbital velocity of the moon round the sun (30 km sec^{-1}) might be sufficient to cause an appreciable increase in density near the leading face of the moon.

The magnitude of the increase will depend on the surface effects, when the proton–electron gas, having a temperature of the order of 10 000°K, comes into contact with the lunar surface at a temperature of 160°K. It seems probable that in such an encounter, the majority of the particles will recombine at the surface and will subsequently escape before being reionized. Since the observed effects can only be explained if all the particles, after collision, leave the surface with a velocity of 2·0 km sec^{-1}, corresponding to the temperature of the dark surface, and retain their charge, it seems unlikely that this mechanism is important.

The electron density is therefore probably caused by the action of solar radiation on the lunar atmosphere and estimates of the gas density will now be made for the cases of a ' permanent ' and an escaping atmosphere.

4.1. *Atmosphere in Hydrostatic Equilibrium*

It is difficult to estimate the degree of ionization of the lunar atmosphere by comparison with the terrestrial ionosphere, because its composition probably differs from that of the earth's upper atmosphere in the following ways.

4.1.1. *Chemical composition*

Whereas the earth's atmosphere above 400 km consists almost entirely of N_2 and O, the atoms and molecules comprising the ' permanent ' lunar atmosphere must have a molecular weight greater than 42 if the temperature is equal to, or greater than the surface temperature of $380°K$; otherwise the molecular velocities will exceed the velocity of escape.

4.1.2. *Temperature*

Both the mechanism responsible for heating the earth's upper atmosphere, and the temperature above a height of 200 km are uncertain. By extrapolating results obtained from observations using rockets, Bates (1954) has derived, for two different models, the values of $900°K$ and $1700°K$ for the temperature at 500 km. Nicolet (1956) and Urey (1957) have shown that even higher temperatures must be assumed to account for the observed rates of escape of ^{3}He and ^{4}He. However, the temperature of the lower region of the lunar atmosphere is probably not very different from that of the surface ($380°K$ on the sunlit side), and it is difficult to estimate how the temperature varies with height, when the mechanism for heating the terrestrial ionosphere is, as yet, not understood.

If the temperature is $400°K$, the scale height of the ' permanent ' lunar atmosphere would be about 50 km and hence, it can be seen from the table that the electron density required to produce the observed angle of refraction is 10^3 cm^{-3}.

In the terrestrial ionosphere above a height of 400 km. about 1/100 of the total number of particles are ionized. As the molecules in the ' permanent ' lunar atmosphere have a high molecular weight, they are more readily ionized than those in the ionosphere. However, diffusion to the surface of the moon, where the charged particles will recombine, may tend to reduce the proportion of charged particles. It is difficult to make a quantitative estimate of the latter effect, but provided it is not of undue importance, it is probable that at least one in a thousand particles is ionized. The total number of particles in the lunar atmosphere is therefore unlikely to exceed 10^6 cm^{-3} ; the density of the lunar atmosphere would then be 10^{-13} of that of the earth's atmosphere at sea level.

If it is considered that the observations provide only an upper limit to the electron density surrounding the moon, then the density of the

' permanent ' lunar atmosphere must be less than 5×10^{-13} of that of the earth's atmosphere at sea level.

It is unlikely that the atmosphere will condense on the surface at the dark side of the moon, for, although the surface temperature is only about $160°$K, the lunar atmospheric pressure is very much less than that required to liquify the probable constituents.

4.2. *Escaping Atmosphere*

It is probable that certain gases, of such low densities that hitherto they have been neglected, are continuously escaping and are being replaced at the moon's surface. Such mechanisms responsible for this are (1) radioactive decay of part of the rocks comprising the moon's crust, leading to the production of helium and argon for example, (2) vaporization of a fraction of the 2×10^5 g of meteors which strike the surface of the moon daily, and (3) release of gases from the interior of the moon.

Provided that about one in a thousand of the escaping molecules is ionized, the density of the atmosphere at the surface of the moon is about 5×10^{-13} of the earth's atmosphere at normal temperature and pressure.

§ 5. Conclusion

The observations provide no indication of the relative abundance of the two forms of atmosphere ; such information could only be derived from detailed measurements of the variation of refraction with distance from the moon's limb. In the event of approximately equal abundances, the density of the atmosphere at the surface of the moon is about 2×10^{-13} of that of the earth's atmosphere at sea level, and is unlikely to exceed 6×10^{-13} of that of the terrestrial atmosphere at normal temperature and pressure.

As the mean free path in the lunar atmosphere is very long, it is probable that the ionization may extend over the dark side of the moon. In the extreme case of equal refraction occurring at both limbs of the moon, the above values of the density are divided by two.

REFERENCES

BATES, D. R., 1954, *Rocket Exploration of the Upper Atmosphere* (London : Pergamon Press Ltd.), p. 347.

COSTAIN, C. H., ELSMORE, B., and WHITFIELD, G. R., 1956, *Mon. Not. R. astr. Soc.*, **116**, 380.

DOLLFUS, A., 1952, *C. R. Acad. Sci., Paris*, **234**, 2046.

ELSMORE, B., and WHITFIELD, G. R., 1955, *Nature, Lond.*, **176**, 457.

LINK, F., 1956, *Bull. astr. Czech.*, **7**, 1.

LIPSKIJ, J. N., 1953, *Publ. Sterberg Astron. Inst. Moscow*, **22**, 66.

NICOLET, M., 1956, *Penn. State Report* No. 86.

ÖPIK, E. J., 1955, *Irish Astron. J.*, **3**, 137.

SEIDENTOPF, H., BEHR, A., and ELSÄSSER, H., 1953, *Nature, Lond.*, **171**, 1066.

STOREY, L. R. O., 1953, *Phil. Trans. roy. Soc. Lond.*, **246**, 113.

UREY, H. C., 1957, in preparation for *Handbuch der Physik*.

CORRESPONDENCE

The Etching of Dislocations in Crystals of Silver Halides

By D. A. JONES and J. W. MITCHELL

H. H. Wills Physical Laboratory, University of Bristol

§ 1. INTRODUCTION

Two techniques have recently been developed which allow dislocations in a number of transparent inorganic crystals to be studied with the microscope. The first is based upon the fact that etching solutions often attack particular crystal surfaces more rapidly at points where dislocations emerge than elsewhere. Much valuble information about the properties and behaviour of the dislocations may then be derived from the study of the etch pits. The second depends upon the internal separation of a decorating substance along the dislocation lines.

The most useful observations will be made when it is possible to use the two methods in succession for the study of the same dislocations ; this has so far been possible only in the case of silicon. Here, Dash (1956, 1957) has applied both techniques to the same crystals and established the correspondence between etch pits and decorated dislocations. It has not yet proved possible to decorate the dislocations within crystals of lithium fluoride but Gilman and Johnston (1956, 1957) have made many observations of the motion of dislocations in the crystals with the etch pit techniques which they have developed. Barber *et al.* (1957) have worked out a useful method for decorating the dislocations in crystals of sodium and potassium halides with gold but reliable etching of the dislocations in the crystals prior to decoration has not yet been achieved. In all these inorganic crystals, the properties of the dislocations which are always present in the annealed crystals are different from those of the additional dislocations which appear during deformation.

The purpose of this note is to describe the etching of both types of dislocations in annealed and plastically deformed crystals of silver halides. The correspondence between the etch pits and the points of emergence of dislocations has been established by subsequent exposure which causes silver to separate along the dislocation lines (Hedges and Mitchell 1953).

§ 2. EXPERIMENTAL METHODS

The silver chloride, silver chloro-bromide, and silver bromide sheets which are being used for this work are grown from the melt by the method described by Clark and Mitchell (1956). After separation from the glass

plates, they are annealed for 8 hours in an atmosphere of the halogen at a temperature between 200 and 400°C. The halogen is then condensed by immersing a side arm in liquid air for 1 hour before the furnace is allowed to cool. The crystals are deformed by elongation and by indentation with hemispherical glass indenters and then etched and exposed to reveal the dislocations.

Although many solvents attack the surfaces of silver halide crystals preferentially around the points of emergence of dislocation lines, experience has shown that a 3N solution of sodium thiosulphate provides the most reliable differential etchant. The solution is allowed to act for the shortest possible time ; the specimens are simply immersed in the solution and transferred immediately to water. The etch pits may subsequently be enlarged, usually with some loss of resolution, by treatment with a much weaker solution of sodium thiosulphate which does by itself not etch the dislocations reliably.

After they have been thoroughly washed and dried, the etched crystals are exposed to the unfiltered radiation from a 250 watt high pressure mercury vapour lamp for 30 seconds at a distance of about 30 cm from the lamp ; this causes the separation of silver along the dislocation lines to a depth of at least 40 microns below the surface.

§ 3. Experimental Observations

The thin sheets which are produced by crystallizing discs of molten silver halides between glass plates usually consist of a few large crystals with surfaces almost parallel to (001) planes. After annealing, the presence of dislocations in crystals with precise (001) surfaces, whether the crystals have been plastically deformed or not, cannot usually be established either by etching or by the separation of internal silver (fig. 1, Pl. 39). These crystals do not show sub-structures and have a very low reactivity towards photographic sensitizers and developers (Evans *et al.* 1955). Very few dislocations are observed in crystals with surfaces almost parallel to (001) planes (fig. 2, Pl. 39). As the deviation increases, a few isolated walls first appear (fig. 3, Pl. 40) followed by the well defined sub-structures which have been studied in detail in our previous work (Mitchell 1957). The dislocations thus etch and due to subsequent exposure to light are decorated by the internal separation of silver to a steadily increasing extent as the angle between the surface and the (001) planes increases from 0° to about 10°, the maximum deviation usually found in these crystals.

It will be observed in the photomicrographs that the etch pits which are produced by the 3N solution of sodium thiosulphate have smoothly curved sides and rounded bases. They may be enlarged to pyramidal pits with apparent crystallographic facets by subsequent immersion in a weaker solution of sodium thiosulphate.

A careful study of the correspondence between etch pits and dislocations has shown that not all etch pits are associated with dislocations

which may be made visible by the separation of internal silver. Neither do etch pits appear at all the points where dislocations, which can be made visible during exposure, meet the surface. The correspondence depends on the precise crystallographic orientation of the surface and upon particular properties of individual crystals : it is complete in many crystals but absent in others.

The dislocations which appear during plastic deformation at room temperature give smaller etch pits and print out to a smaller extent than those which are already present in annealed specimens. The two types of etch pit are shown in fig. 4, Pl. 40. This specimen was etched, deformed with a hemispherical indenter, and then re-etched. The larger pits which are not as well defined as in figs. 2 and 3 are associated with the grown-in dislocations and the smaller sharply defined pits with dislocations which appeared during plastic deformation. The most sensitive conditions for the study of the behaviour of dislocations during the deformation of silver chloride crystals occur when the crystals have surfaces almost parallel to (001) planes ; in these crystals, the apparently small numbers of grown-in dislocations can only just be rendered visible by etching. The small and shallow etch pits corresponding with dislocations on slip bands produced by the deformation of such crystals can easily be resolved with the phase contrast microscope.

With exposure to light silver separates along the dislocation lines which appear during plastic deformation to form an internal latent image, and this accounts for the greatly enhanced internal sensitivity of such crystals. The internal image may be developed after the removal of the surface with a dilute solution of potassium cyanide. In favourable circumstances, the exposure may be continued until the dislocation lines become visible within the crystals (Mitchell 1957).

Our observations indicate that the dislocations in the annealed crystals which give rise to deep etch pits and along which visible amounts of silver separate rapidly during exposure do not play an important role during the early stages of plastic deformation. It may be concluded that their mobility is reduced by the segregation of impurities or of vacancies during cooling to room temperature after crystallization or during subsequent annealing. When the crystals are deformed, dislocations appear within the elements of the substructures as in the experiments on lithium fluoride of Gilman and Johnston (1956, 1957).

§ 4. Conclusion

The silver halides provide the only inorganic crystals, which have so far been studied, in which the presence and properties of the dislocations associated with both annealing and deformation structures can be established by the application of etching and decoration techniques at room temperature. The dislocations can be rendered visible under the actual conditions of deformation and modifications due to the decoration techniques are therefore excluded,

References

Barber, D. J., Harvey, K. B., and Mitchell, J. W., 1957, *Phil. Mag.*, **2**, 704.
Clark, P. V. McD., and Mitchell, J. W., 1956, *J. Photogr. Sci.*, **4**, 1.
Dash, W. C., 1956, *J. appl. Phys.*, **27**, 1193 ; 1957, *Dislocations and Mechanical Properties of Crystals*, Lake Placid Conference on Dislocations (New York ; John Wiley).
Evans, T., Hedges, J. M., and Mitchell, J. W., 1955, *J. Photogr. Sci.*, **3**, 73.
Gilman, J. J., and Johnston, W. G., 1956, *J. appl. Phys.*, **27**, 1018 ; 1957, *Dislocations and Mechanical Properties of Crystals*, Lake Placid Conference on Dislocations (New York : John Wiley).
Hedges, J. M., and Mitchell, J. W., 1953, *Phil. Mag.*, **44**, 223.
Mitchell, J. W., 1957, *Dislocations and Mechanical Properties of Crystals*, Lake Placid Conference on Dislocations (New York : John Wiley).

A Demonstration of Parity Non-Conservation in β-Decay

By M. A. Grace, C. E. Johnson, R. G. Scurlock and C. V. Sowter
Clarendon Laboratory, Oxford

Since the suggestion of Lee and Yang (1956) that parity conservation might not hold in weak interactions, attention in recent work on nuclear orientation has been focused on the angular distribution of β-particles emitted from polarized nuclei. We have established the feasibility of detecting β-particles by the blackening of a photographic film inside a cryostat at a temperature of $1°\text{K}$ and have used this method of recording to measure the angular distribution of the β-emission from polarized ^{60}Co. A backward–forward asymmetry was observed, in agreement with the results of Wu *et al.* (1957), thus confirming that parity is not conserved in β-decay. Although this detection method does not enable energy discrimination to be made, it has the merit of simplicity and of allowing the angular distribution to be measured simultaneously at different angles. In the present experiment, observations were confined to the $0°$ and $180°$ directions.

The photographic film has to be used within the low temperature cryostat at $1°\text{K}$ and therefore the main requirement of the film is that it should be sensitive to β-rays at this temperature. Several films were tested and most of these showed a large reduction in sensitivity as the temperature was lowered. However, it was found that for Ilford Industrial G x-ray film, the blackening sensitivity to β-radiation from ^{60}Co

is only reduced by a factor of two when the film is cooled from room temperature to 1°K. Most of the change in sensitivity occurs when the film is cooled from room temperature to 90°K. The γ-rays have relatively little effect on the film owing to their much smaller absorption. Visible light was prevented from affecting the film by protecting it with aluminium foil 0·0002 in. thick. Such a thickness reduces the ^{60}Co β-ray intensity by about 10%. It was found that a two minute exposure at 1°K to a 10 μc source of ^{60}Co at a distance of 5 mm produced sufficient blackening to detect a change greater than 4% in the intensity of the β-emission. (Scurlock and Sowter, to be published.)
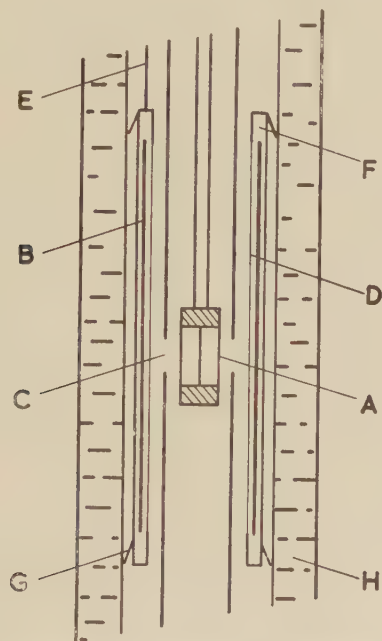
Section through demagnetization cryostat. A, radioactive crystal ; B, cylindrical photographic film : C, apertures defining the β-ray beam ; D, aluminium window ; E, thread for raising the film carrier F ; G, spring guides for locating film carrier ; H, helium bath.

The method of polarizing ^{60}Co was that described by Ambler *et al.* (1953). A pair of single crystals of cerium magnesium nitrate was grown with a thin surface layer in which some of the Mg⁺⁺ ions were replaced by ^{60}Co ions. The crystals were mounted in the demagnetization cryostat with the crystal axis horizontal. A sectional view of the apparatus is given in the figure, and shows the cylindrical photographic film which could be raised past the crystals by an externally operated thread. The β-rays were screened from the film by a brass tube containing two apertures (4 mm diameter) to define a fixed β-ray beam.

In the experiment, the crystals were cooled to 0·003°K by adiabatic demagnetization from 25 kilogauss applied perpendicularly to the crystal axis at 1°K. and the cobalt nuclei were polarized by applying a field of 600 gauss along the axis. The resulting temperature of the surface layer was of the order of 0·01°K and was estimated from the γ-ray anisotropy measured with scintillation counters mounted outside the cryostat. The carrier was raised so as to expose the film for 2 minutes. Helium exchange gas was then admitted to warm the crystal to the temperature of the helium bath, and the carrier was raised again to take a normalizing exposure with the nuclei randomly oriented. Without exchange gas, the crystals would remain cold for nearly half an hour. The possibility of geometrical effects producing a β-asymmetry was eliminated by repeating the experiment with the polarizing field reversed. The apparatus was then warmed up to room temperature and the film removed and developed. The intensities of the exposures were measured with a microphotometer.

Three sets of low temperature photographic runs with different pairs of crystals were made. All of these showed backward–forward asymmetries in which the greater intensity was against the direction of the polarizing field. The most consistent set showed an 18% difference between the 180° and 0° directions, with a corresponding γ-ray anisotropy of 7%. The sign of the difference shows that the β-emission is preferred against the direction of the nuclear spin.

If parity is not conserved, the angular distribution of the β-particles in an allowed transition may be expected to have the form $1 + \alpha \cos \theta$. (θ is the angle of emission measured from the axis of nuclear polarization.) The observed value of the asymmetry parameter α is $-0·09 \pm 0·03$ and the γ-ray anisotropy (0·07) corresponds to a nuclear polarization P_1 of 0·25. The total error has been assessed from control experiments and arises from two main sources (1) a reduction in the β-sensitivity of the film by γ-ray fogging, and (2) the difference in the experimental reproducibility of identical exposures. Since no energy discrimination is available, it is not possible to correct the experimental value of α for the effects of the magnetic field on the electron paths and of the back-scattering in the crystal. Our uncorrected result, however, agrees closely with that of Wu *et al.*

It is interesting to observe that the surface remains at about 0·01°K, as shown by the γ-ray anisotropy, for a considerable time after demagnetization, and therefore the mechanism of thermal conduction is much more favourable than would be expected from an extrapolation of measurements on lattice conductivities made at higher temperatures.

References

Ambler, E., Grace, M. A., Halban, H., Kurti, N., Durand, H., Johnson, C. E., and Lemmer, H. R., 1953, *Phil. Mag.*, **44**, 216.
Lee, T. D., and Yang, C. N., 1956, *Phys. Rev.*, **104**, 254.
Wu, C. S., Ambler, E., Hayward, R. W., Hoppes, D. D., and Hudson, R. P., 1957, *Phys. Rev.*, **105**, 1413.

Density Change of a Crystal Containing Dislocations

By W. M. Lomer

Atomic Energy Research Establishment, Harwell, near Didcot, Berks

Seeger (1956) has recently evaluated the decrease in density of a crystal consequent upon the introduction of a dislocation. His calculation is based on the deviation of real crystals from ordinary linear elasticity. He estimates the magnitude of the effect by assuming that on shearing a crystal the planes of atoms ride up on the neighbouring planes to an extent proportional to the square of the shear strain, and determined the constant of proportionality analytically, using explicit interatomic forces. His result is that the expansion is about $\frac{3}{4}\Omega$ per atomic plane of dislocation (Ω—atomic volume). and that it is distributed in space just like the elastic energy (since both depend on the square of the elastic strains).

It is interesting to note that the order of magnitude of the effect is confirmed by a very simple argument. The thermal expansion of most solids can also be related to the deviations from linear elasticity, and Gruneisen's relation can be exhibited as a relation between thermal energy content and volume expansion. The Gruneisen constant γ is defined as

$$\gamma = \frac{3\alpha V}{KC_v},$$

where K is the compressibility, α is the coefficient of linear expansion, and C_v is the specific heat. Rearranging and replacing α and C_v by their usual definitions we get

$$\frac{dV}{dT} = \gamma K \frac{dH}{dT}$$

where H = thermal energy content.

In a solid, half the thermal energy is kinetic energy, and half elastic potential energy. If the volume expansion is proportional to the elastic energy W, we finally get

$$\delta V = 2\gamma K \delta W.$$

To substitute some numerical values, consider copper, with $\gamma = 1\cdot9$, $K = 7 \times 10^{-13}$ cm³/erg.   Then

$$\frac{\delta V}{\delta W} = 2\cdot6 \times 10^{-12} \text{ cm}^3/\text{erg}$$

$$= 4\cdot25 \times 10^{-24} \text{ cm}^3/\text{ev}.$$

The energy of a dislocation in copper is typically about 6 ev/atom plane, and the atomic volume is $11\cdot6 \times 10^{-24}$ cm³, so that we in fact predict a greater volume expansion than Seeger, nearly 2Ω per atomic length of dislocation line in copper.   The discrepancy may be due to Seeger's neglect of all but the shear strains parallel to the slip plane.

It should be commented that the elastic constants effectively cancel in this calculation, since the energy of the dislocation is proportional to the elastic constants, and K inversely proportional.   For an isotropic medium the volume expansion per unit length of edge dislocation line is

$$3\gamma \frac{(1-2\sigma)}{1-\sigma^2} \frac{\mathbf{b}^2}{4\pi} \ln\frac{R}{r_0} ; \qquad .$$

where σ is Poisson's Ratio, $\mathbf{b}$ the Burgers vector, R and r_0 the outer and inner radii of the effectively strained region.   It would be interesting to compare experimentally the density recovery and energy release in say Cr ($\gamma = 0\cdot9$) and Au and Pt ($\gamma = 3\cdot0$).

<div align="center">REFERENCE</div>

<div align="center">Seeger, A., 1955, *Z. Phys.*, **146**, 217.</div>

REVIEWS OF BOOKS

Atomic Physics. By MAX BORN (6th edition revised in collaboration with R. J. Blin-Stoyle). Blackie & Son Ltd. [Pp. xiv+445.] Price 40s.

IT is twenty-two years since the first edition of this book appeared, and now the sixth comes to us looking as young and alluring as ever. The characteristic array of appendices remains, to satisfy appetites whetted by the equally characteristic and lucid text. There is a little more material than in previous editions, just enough to make us marvel at how little is needed to supplement what must have been, in the beginning, a most exciting and magisterial account of the new ideas in Physics. With familiarity some of the excitement has perhaps waned, but Born's Atomic Physics still remains, and will long remain, we hope, the best introduction for the novice and the best corrective for the over-sophisticated initiate.   A. B. P.

Electricity and Magnetism. By B. I. BLEANEY and B. BLEANEY. (Clarendon Press.) [Pp. xiv+676.] Price 63s.

THIS excellent book by Prof. and Mrs. Bleaney supplies a real need in the advanced teaching of electricity and magnetism, for a book which shall be at once accurate, up-to-date and interesting (especially interesting). Some 450 pages are devoted to those topics which may be expected to appear in such a book, and everywhere the account seems admirably intelligible, without undue emphasis on finer points of difficulty. There is even a photograph of a modern galvanometer, marking a notable break from traditional presentations. The last 200 pages treat phenomena in atomic and solid-state physics which are electric and magnetic in nature, such as fluctuations, dielectrics, metallic conduction, magnetism of solids, and magnetic resonance, and here the authors write with the authority of research workers in the field, while still bearing in mind the needs of the reader whom they are addressing. It is a pity that radio propagation and ionospheric physics are entirely neglected, but clearly this is not due to inadvertence.

The book is full of examples and problems, many of which carry the arguments one stage further. The choice of examples is catholic and imaginative. One may confidently predict for it a long and useful life.   A. B. P.

Optics. By BRUNO ROSSI. (Addison-Wesley Publishing Co., Inc., Reading, Mass., U.S.A.) [Pp. 510.] Price $8.50.

IT is clear that, in this book, the author has given great thought to the best method of presentation of each topic. The style is clear and concise. This, together with the excellent diagrams and typography, makes the book a pleasure to read, and very easy to follow.

The standard of the book is roughly that required for a normal degree course. It includes geometrical optics and physical optics. The chapters on the electromagnetic theory of light (which presuppose a knowledge of Maxwell's equations) would only be required by a student for final honours in Physics. For the rest of the book, the only mathematical knowledge which is assumed is a knowledge of calculus and simple differential equations. The student for final honours will find that the book does not cover a few special topics which he may require. These include the Fourier approach to diffraction, the theory of the resolving power of a microscope, and the theory of white light.

A large number of problems are given at the end of each chapter. These are more interesting than usual, and often extend the treatment given in the text.

For a first edition, the book is remarkably free from errors. One mistake, however, does occur on page 328, where it is stated that the transverse character of light waves cannot be explained on an elastic wave theory.

This is a very valuable book, and will undoubtedly become a standard textbook on the subject.   **B. H. B.**

The Journal of Photographic Science, March/April, 1957, Vol. 5, No. 2. (The Royal Photographic Society of Great Britain.) [Pp. xii+31.] Price: Annual subscription (six bi-monthly parts) £1 5s. 0d.

A SPECIAL number of the Journal of Photographic Science has appeared dealing with high speed photography. The contents are as follows :

" High frequency cinematography in the shock tube " by H. Schardin ;

" A 16 mm. missile camera " by R. B. Herden ;

" Photographic instrumentation at ordnance proving grounds " by G. Doughty ;

" Detonation studies of pentolite sticks " by M. Sultanoff ;

" High speed photography " by J. S. Courtney-Pratt and D. P. C. Thackeray ;

" Report of meeting : High-speed photography " by P. Naslin.

N. F. M.

Les Dislocations. By J. FRIEDEL. (Gauthier-Villars, Paris.) [Pp. 314.] Price £3 14s. 0d.

DURING the last few years dislocation theory has undergone considerable development. The extent of this development can be judged from the scope of this book, the first part of which is concerned entirely with a purely formal treatment of dislocation theory. Chapters are included on elastic theory, glide and climb, on imperfect dislocations, and on crystal growth. The second part of the book is devoted to assemblies of dislocations and to applications of the theory to ' elastic ' moduli, work-hardening, recovery, recrystallization, creep and fracture. The last part of the book deals with the interaction of dislocations with impurities.

The subject has been presented in a very clear manner : often simple arguments are used to derive energies associated with dislocations and other defects. The order in which the theory is presented and the clear style make the book a valuable basis for a lecture course. On the other hand, numerous sections obviously represent new and original contributions to the subject. The section on climb is an example and should be read by anyone engaged in studies of high temperature creep and related phenomena.

After reading this book one feels that whereas the basic properties of dislocations are understood, much remains to be done in the field of application of the theory to the many-bodied problems of creep, work-hardening, recrystallization etc. There is also a lack of calculations on the dislocation core, and this is emphasized by the fact that the Peierls-Nabarro treatment receives only cursory attention.

This book is to be recommended to all those engaged in the study of dislocations. It is by far the most extensive treatment of the subject yet produced. Unfortunately, circulation will however be restricted owing to the very high price. A cheaper translation into English would seem well worth while.

P. B. H.

Physical Properties of Crystals. By J. F. NYE. (Clarendon Press, Oxford.) [Pp. 322+xv.] Price 50s.

THIS book deals with the systematic formulation of the macroscopic tensor properties of crystals. There are four parts : the first deals with the mathematics and properties of tensors. The second part covers the equilibrium properties of crystals, including magnetic susceptibility, polarization, piezo-electricity and elasticity, and ends with a chapter on the thermodynamic relations between these properties. Part III deals with transport properties, i.e. conductivity, and the last part with crystal optics. A number of useful appendices are added at the end.

It has been a real pleasure to review this book, which has been written in a style of exemplary clarity. The arrangement of the subject matter is excellent and this makes the book, or rather parts of it, particularly useful as a basis for a lecture course. At the same time, most of the important tensor properties are treated in detail, and the book will therefore also serve as a useful reference book to solid state research workers. I believe that this book will remain the standard work on this subject for many years. Praise should also go to the Oxford University Press for the high quality of the production of this work.

P. B. H.

BOOK NOTICES

Trilinear Chart of Nuclides. By W. H. SULLIVAN. (Washington : U.S. Government Printing Office.) [Pp. 4+chart.] Price $2.00.

Nonparametric Methods of Statistics. By D. A. S. FRASER. (London : John Wiley.) [Pp. x+299.] Price 68s.

Proceedings of the Third Berkeley Symposium on Mathematical Statistics and Probability. Edited by JERZY NEYMAN. (Berkeley and Los Angeles : University of California Press : London : Cambridge University Press.)

Volume 1. Contributions to the Theory of Statistics. [Pp. viii+208.] Price 45s.
Volume 2. Contributions to Probability Theory. [Pp. viii+246.] Price 49s.
Volume 4. Biology and Problems of Health. [Pp. viii+179.] Price 43s. 6d.
Volume 5. Contributions to Econometrics, Industrial Research, and Psychometry. [Pp. viii+184.] Price 43s. 6d.

The Index of Technical Articles. A monthly index of articles published in British Technical Periodicals. (Published by Iota Services Ltd., 38 Farringdon Street, London, E.C.4.) [Subscription £6 6s. per annum.]

Physics of Non-Destructive Testing, with particular reference to some of the new aspects. British Journal of Applied Physics, Supplement No. 6. (London : The Institute of Physics.) [Pp. iii+72.] Price 25s.

Causality and Chance in Modern Physics. By DAVID BOHM. (London : Routledge & Kegan Paul.) [Pp. xi+170.] Price 21s.

Linear Inequalities and Related Systems. Edited by H. W. KUHN and A. W. TUCKER. (Princeton University Press : London : Oxford University Press.) [Pp. xxi+322.] Price 40s.

Progress in Cosmic Ray Physics. Vol. III. Edited by J. G. Wilson. (Amsterdam : North Holland Publishing Company.) [Pp. xii+420.] Price 76s.

Theory of Alloy Phases. A seminar on theory of alloy phases held in Philadelphia from October 15 to 21, 1955. (Cleveland, Ohio : American Society for Metals.) [Pp. iii+378.] Price not stated,

Discovery of the Universe. By G. de Vaucouleurs. (London : Faber & Faber.) [Pp. 328.] Price 30s.

An Introduction to Junction Transistor Theory. By R. D. Middlebrook. (London : John Wiley.) [Pp. xxiv+296.] Price 68s.

Instrumental Analysis. By P. Delahay. (New York and London : The Macmillan Company.) [Pp. xi +384.] Price 55s. 6d.

Models of Man. By H. A. Simon. (London : John Wiley.) [Pp. xiv+287.] Price 40s.

Rheology. Theory and Applications. Vol. I. Edited by Frederick R. Eirich. (New York and London : Academic Press.) [Pp. xiv+761.] Price $20.00.

The Hypercircle in Mathematical Physics. By J. L. Synge. (London : Cambridge University Press.) [Pp. xii+424.] Price 70s.

(a)   (×712)

(b)   (×712)

(c)   (×1120)

(d)   (×712)

(e)   (×712)

(f)   (×1120)

(a)   (×712)

(d)   (×71
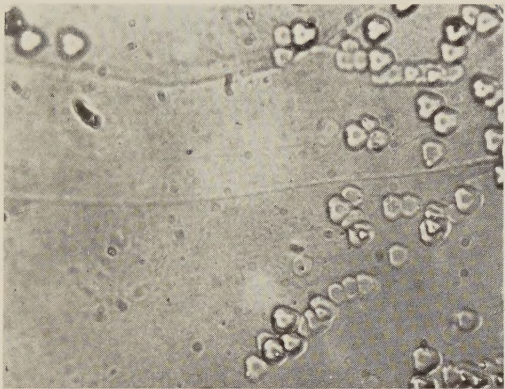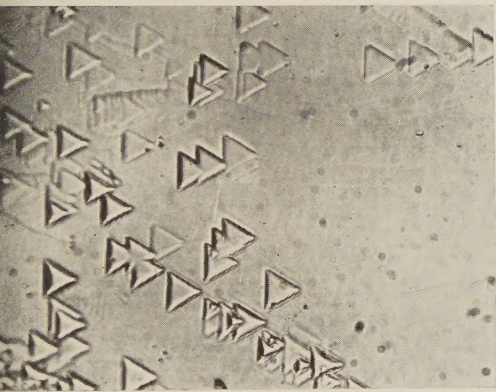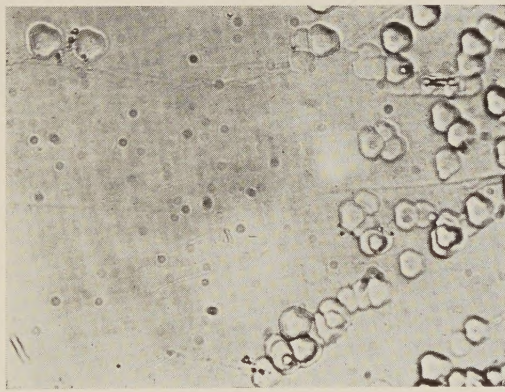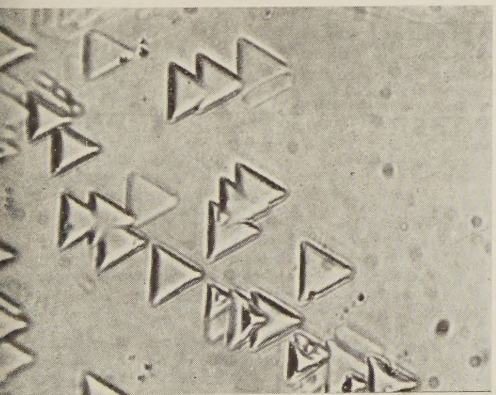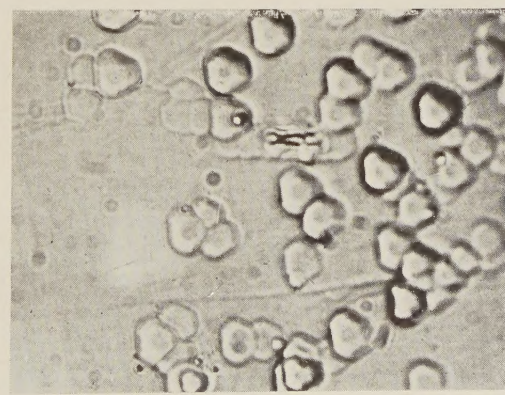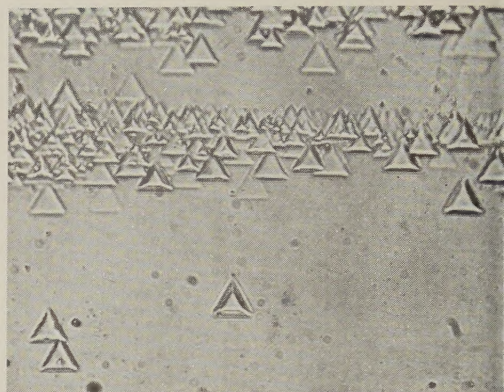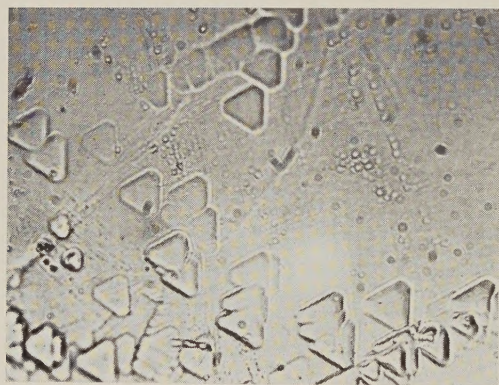
(b)   (×712)
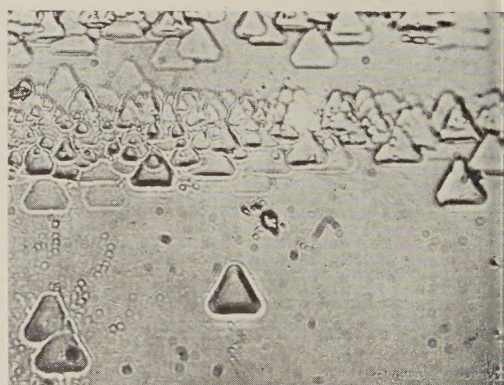
(e)   (×712
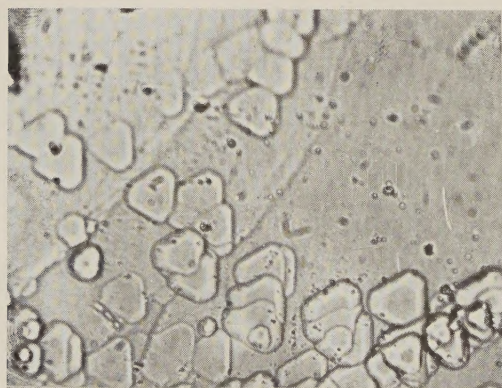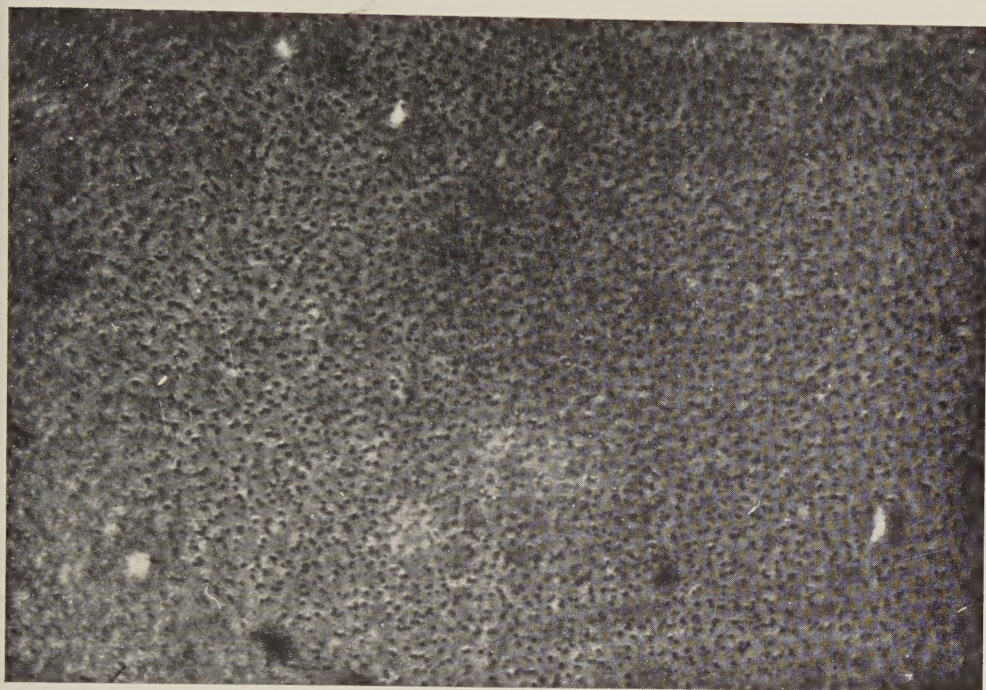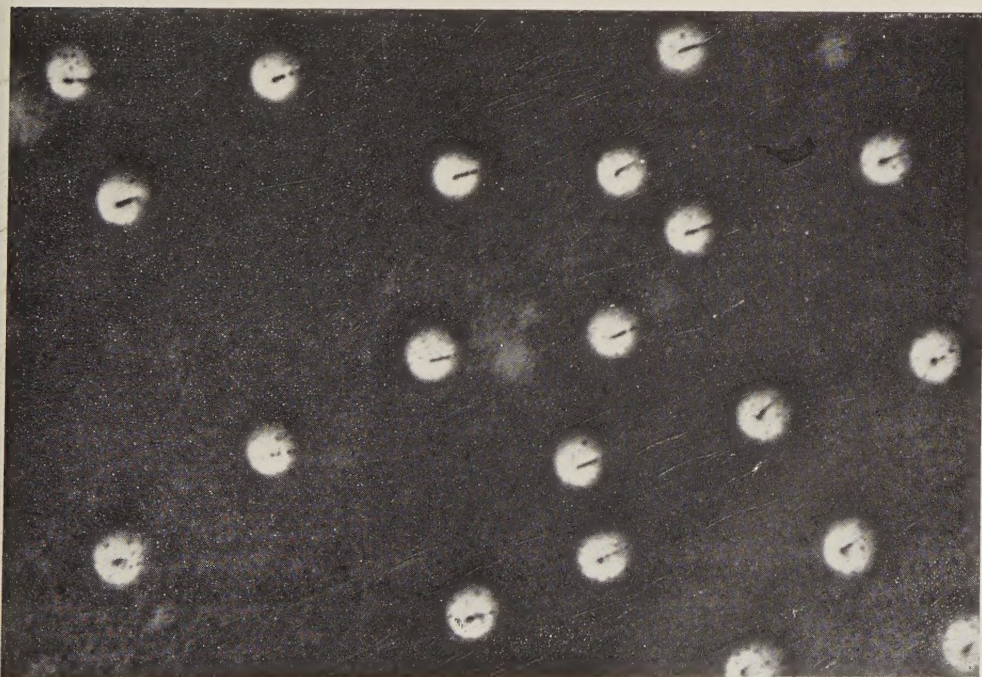

(c)   (×712)

(f)   (×712

Fig. 1

A silver chloride crystal with surface parallel to the (001) planes after etching
and exposure. Any dislocations which are present in these crystals
cannot be made visible either by etching or by the internal separation of
silver. The dark specks represent particles of silver on the surface
of the crystal.   (×2500)
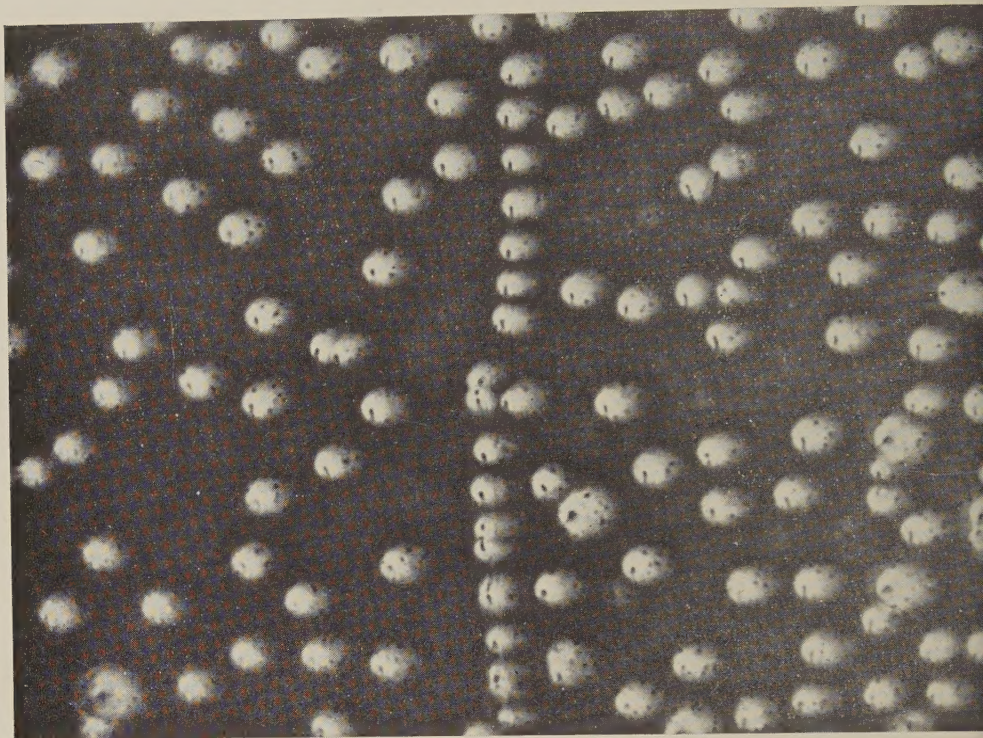
Fig. 2

Dislocations forming elements of a coarse three dimensional network (see
Hedges and Mitchell 1953, fig. 3) made visible in a crystal of silver
chloride both by etching and by the internal separation of silver resulting
from the subsequent exposure to light. This establishes the correspond-
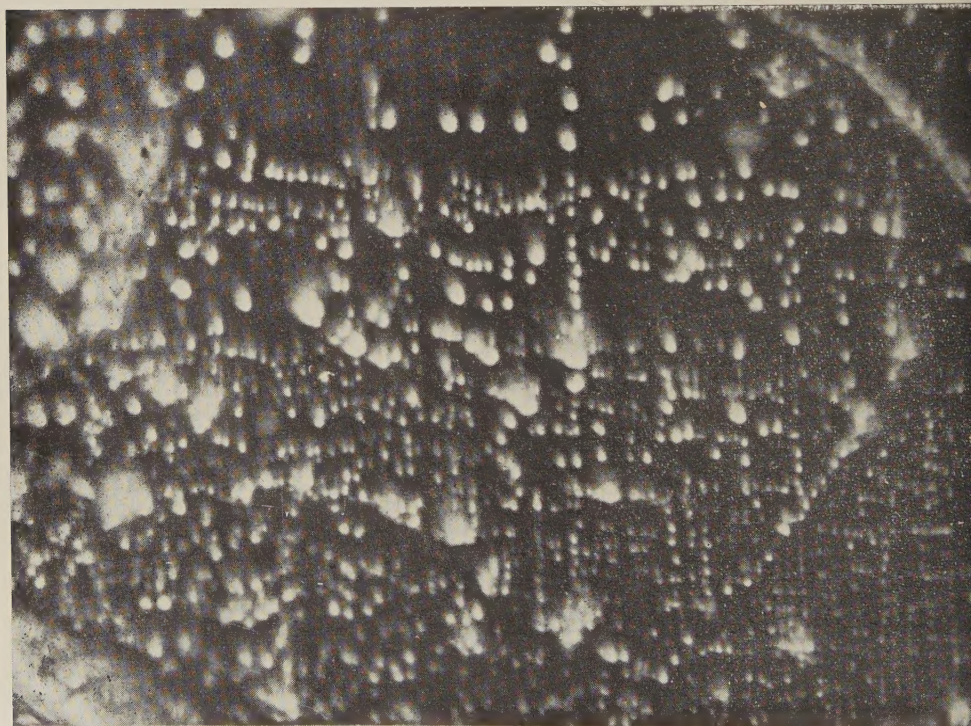ence between etch pits and dislocation lines.   (×2500)

Fig. 3

A wall of dislocations in an annealed crystal of silver chloride.
(×2500)

Fig. 4

Dislocations introduced by the deformation of an element of the substructure of a crystal of silver chloride.   (×2500)

NOTE.–All the photomicrographs have been taken with phase contrast